A MECHANISM BASED INVESTIGATION OF THE DYNAMIC BEHAVIOR OF PURE MAGNESIUM

by

Neha Dixit

A dissertation submitted to The Johns Hopkins University in conformity with the requirements for the degree of Doctor of Philosophy.

Baltimore, Maryland

May, 2015

Abstract

The global emphasis on improving energy efficiency in recent years has propelled the development of new engineering solutions to meet the high efficiency standards. The push from the transportation industry to achieve weight reduction of automobiles/components (in order to meet the higher standards for fuel efficiency) has renewed interest in lightweight materials such as magnesium (Mg). Mg alloys have low density and high specific strengths which makes them attractive in applications where their increased use can lead to significant energy savings. In order to successfully use these materials in applications in which they will be subjected to dynamic loading such as automotive, aerospace and defense applications, we need to assess and understand their behavior under such conditions. The deformation behavior of this HCP material is complicated by the richness of the slip and twinning modes and their interactions and dynamic loading may introduce additional complexities.

High strain rate (Kolsky bar) and normal plate impact experiments were performed on pure extruded magnesium to analyze the mechanical behavior. Microstructural analysis of the pre and post deformation samples was performed in order to

understand the dominant deformation mechanisms and their evolution. Optical microscopy and electron back scattered diffraction (EBSD) was performed to analyze deformation twinning and transmission electron microscopy (TEM) was performed to analyze the dislocation structures. It was observed that under uniaxial stress compression at high strain rates ($\sim 10^3 s^{-1}$) in the ED (induced by Kolsky bars), extension twinning, $\langle a \rangle$ slip and $\langle c+a \rangle$ slip are necessary to accommodate plastic strains. The microstructural observations show that extension twinning reorients the material by 86^0 to a harder orientation and causes a significant change in the texture. The insights gained from the analysis of the evolution of the dominant deformation mechanisms are used to develop a simple mechanism based constitutive model which captures the behavior of single and polycrystalline Mg.

The normal plate impact experiments conducted (on both single crystal and polycrystalline Mg) at 60-70 m/s impose a uniaxial strain loading for very short durations (~ 2 μs). Elastic-plastic plate impact simulations performed in Abaqus/Explicit show that the stress, strain and strain rate in the specimen thickness are inhomogeneous in these experiments. Deformation twinning is observed under this loading of very short duration although the characteristics of the twins formed under this loading are different than those induced by the Kolsky bar loading ($\sim$200 s). The twins induced by the plate impact loading are thinner and occupy smaller volume fraction as compared to the ones induced by the Kolsky bar loading. The observations from both the experiments indicate that the differences in the deformation twinning char-

acteristics arise from the differences in the stress states, strain rates and the loading durations in the two cases. These observations help us further our understanding of the mechanisms controlling the dynamic behavior of pure magnesium.

Thesis Advisor and Primary Reader:

Professor KT Ramesh

Secondary Readers:

Professor Kevin Hemker

Professor Tim Weihs

Acknowledgments

This dissertation would not have been possible without the help of some truly great teachers, advisors, family and friends. I sincerely thank each one of them for believing in me and helping me complete this journey.

First and foremost, I express my deepest gratitude to my advisor, Professor KT Ramesh. I came to Johns Hopkins in 2010 not knowing anything about experimental mechanics, dynamics, twinning or dislocations. I am very thankful to him for believing in my capabilities and entrusting me with a very challenging project. The difficult times that came from the initial failures with the plate impact setup are overshadowed by the joy of the success in getting the setup running. My research journey at Hopkins has been very enriching due to the variety of fields that I have learned about. I am also grateful to him for emphasizing the importance of having strong fundamentals in mechanics without which I would have struggled in this journey. His guidance and desire to produce well rounded scientists has been valuable in shaping me into the person I am today.

I am very grateful to my thesis readers, Professors Kevin Hemker and Tim Weihs

for being great teachers, helpful critics and guides in this journey. Much of my knowledge of material science is due to the very educative classes and helpful technical discussions I have had with them.

I am also thankful to the Mechanical Engineering and Material Science faculty. The classes I took here helped build a strong foundation in mechanics of materials which made my research journey much easier than it would have been otherwise.

A special thank you to Dr. Leslie Lamberson for being a part of the challenging journey of reviving the plate impact setup. Thank you for sharing your knowledge in optics, dynamic experimentation and introducing me to Latex.

In 2014, I had the opportunity to spend some time at the National University of Singapore as a visiting scholar. A big thank you to Professor Shailendra Joshi and Dr. Sunil Rawat at the National University of Singapore for the warm welcome to Singapore and introducing me to Molecular Dynamics.

Much of the microscopy presented in this work wouldn't have been possible without the help of Dr. Kelvin Xie, Dr. Kavan Hazeli and Dr. Lukasz Farbaniec. I appreciate their willingness to collaborate and discuss ideas.

I extend my deepest gratitude to the HEMI faculty, staff, post-doctoral fellows and graduate students, both past and present. To Professor Nitin Daphlapurkar and Drs. Eswar Prasad, Jamie Kimberley, Ravi Sastri, Shailesh Ganpule, Cyril Williams, Guangli Hu, Emily Huskins, Cindy Byer, Rika Wright, Adam Fournier, Andy Tonge and Angela Stickle for being available for research discussions and practice exams. To

ACKNOWLEDGMENTS

Matt Shaeffer for making sure the lab equipment was always functioning smoothly.

A special thank you goes out to Dr. Jamie Hogan, Dr. Justin Wilkerson, Debjoy Mallick, Amy Dagro, Andrew Robinson for helping me survive the last few months of thesis writing and have fun. To the current graduate students, Vignesh Kannan, Meng Zhao, Fatma Madouh, Charles El-Mir, Kimmy Leonard, I wish you the best of luck.

To my parents, who always encouraged me to pursue higher education and supported me unconditionally. To my sister for always being there for me.

Finally, and most importantly, to my wonderful husband, Rohit. I could not have done this without your love and unwavering support. I thank you for pushing me when I needed motivation and comforting me when I needed support. This achievement is as much yours as mine.

Dedication

To my loving and supportive family

Contents

List of Tables

List of Figures

Chapter 1

Introduction

1.1 Motivation

The global emphasis on improving energy efficiency in recent years has propelled the development of new engineering solutions to meet the high efficiency standards. The push from the transportation industry to achieve weight reduction of automobiles/components (in order to meet the higher standards for fuel efficiency) has renewed interest in lightweight materials such as magnesium [5–8]. Magnesium is the eighth most abundant element in the earth's crust and its density is only 1.74 g/cm^3 [8]. The low density, high specific strength (strength-to-weight ratio) and good damping qualities of magnesium alloys makes them attractive in a variety of automotive and aerospace applications. Magnesium is biocompatible, due to which it is also being considered for applications in biodegradable and bioabsorbable implants [9].

Another avenue of interest for the use of magnesium and its alloys as structural materials is in armor systems. Armor systems are currently being developed that use magnesium in a composite form or in conjunction with traditional armor materials (e.g. ceramic armor backing plates) [10]. Although pure magnesium is not very strong, it can be alloyed with other elements and processed to impart different textures in order to obtain desirable properties.

The usage of this material in engineering applications has been limited due to issues such as poor corrosion resistance and flammability and also due to the limited understanding of its complex mechanical properties. The complex mechanical behavior of this material affects the ability to process magnesium and its alloys into the desired form factor for engineering applications as well as their performance as load bearing structures [11]. The recent interest in the increased use of magnesium in automotive, aerospace and armor components has driven research in multiple areas such as new alloy design, improving processing techniques and understanding of the structure-property relationship (mechanical behavior of this material). It is important to understand the fundamental deformation mechanisms and their effect on the mechanical behavior in order to successfully use magnesium as a structural material.

1.2 Crystal structure and deformation mechanisms of magnesium

Magnesium has a hexagonal close packed (HCP) crystal structure and a slightly less than ideal c/a ratio. The low symmetry of the HCP crystal structure of magnesium makes its deformation mechanisms more complex as compared to the high symmetry face-centered-cubic (FCC) and body-centered-cubic (BCC) materials. The crystal structure and the dominant slip and twinning systems in magnesium are shown in Fig 1.1 and Fig 1.2 (adapted from Ref [2]). The basal plane contains the crystallographic $\langle a \rangle$ direction whereas the $\langle c \rangle$ direction is perpendicular to it. The $\langle a \rangle$ direction is given by $\langle \bar{1}2\bar{1}0 \rangle$ and the $\langle c \rangle$ direction is given by [0001] with the lattice parameters as $a = 0.32\ nm$ and $c = 0.52\ nm$ [12].

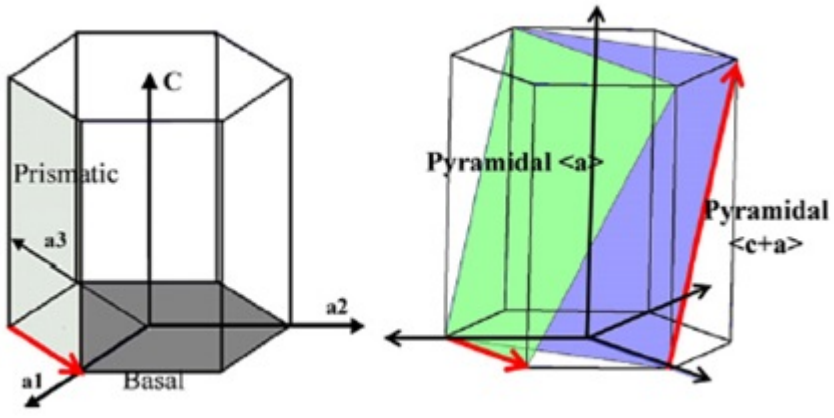

Figure 1.1: Slip systems in magnesium (Figure adapted from Ref [2])

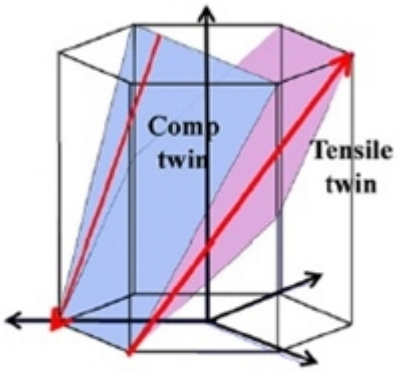

Figure 1.2: Twin systems in magnesium (Figure adapted from Ref([2])

The mechanisms that govern the deformation of Mg and its alloys at low strain rates have been widely studied in recent years [1,13–30]. The dominant slip systems in magnesium are the $(0001)\langle 11\bar{2}0\rangle$ basal slip system and the $\{10\bar{1}0\}\langle 11\bar{2}0\rangle$ prismatic slip system [13,31]. Since both of these slip systems have the $\langle a\rangle$ type Burger's vector, they are insufficient to accomodate general plastic deformations [32, 33] . Thus, additional mechanisms such as the pyramidal $\langle c+a\rangle$ slip system and deformation twinning must be activated under general loading conditions. The commonly observed deformation twinning modes in magnesium are the $\{10\bar{1}2\}\langle\bar{1}011\rangle$ extension twinning mode and the $\{10\bar{1}1\}\langle 10\bar{1}\bar{2}\rangle$ contraction twinning mode [1, 15, 21, 22, 25, 26, 34]. The names represent the type of deformation supplied by the twinning mode. The extension twinning mode accommodates extension along the crystallographic c-axis whereas the contraction twinning mode accommodates contraction along the c-axis [21]. These modes are sometimes referred to as tensile twinning mode and compression twinning

mode respectively. The experimentally measured critical resolved shear stress (CRSS) values for these slip systems in Mg single crystals have been reported by several studies [34–38]. Many authors [34,35,39,40] also define a CRSS for the twin systems, although it is not clear that twinning is controlled only by the magnitude of the shear stress. Recent works suggest that twinning is largely influenced by the local stress concentrations and the grain boundary defects in the case of polycrystalline Mg and alloys [41, 42]. Yu et al. [43] reported twin nucleation stresses of ∼800 MPa for a nanometer sized sample but suggested that these high stresses can be considered as local or microscopic stresses. Although looking at the critical stresses for twinning does not provide complete information about the conditions for twin nucleation, it is often helpful to look at the reported critical stress values in comparison with those reported for other mechanisms [2]. The lowest CRSS is for basal slip (∼ 0.5 MPa), and this appears to be followed by the so-called CRSS for extension twinning (∼ 2-5 MPa) [37, 44]. The reported values of CRSS for prismatic slip (∼ 10-45 MPa), pyramidal $\langle c+a \rangle$ slip(∼ 35-80 MPa) and contraction twinning (∼ 30-100 MPa) are higher (and also display significant ranges in value) [34,35,37,38,44]. The activation of the $\langle c+a \rangle$ pyramidal slip system is difficult due to its high CRSS, but it has been observed in some quasi-static studies [17,18,38,45–47]. Basal slip and extension twinning are thus the mechanisms that are most easily activated in pure Mg when deformed at low rates. The $\{10\bar{1}2\}\langle\bar{1}011\rangle$ extension twin system has been extensively studied in the low strain rate regime over the last decade [1,21,22,29,30,41,48–51].

Contraction twinning was observed in some c-axis compression studies in pure Mg single crystals [34, 40], and some groups have presented observations of contraction twins in polycrystalline Mg alloys [22, 25, 52–54].

1.2.1 Factors affecting the deformation mechanisms of magnesium

1.2.1.1 Effect of texture

Strong texture is developed in Mg and its alloys during thermomechanical processing and has been attributed to the underlying anisotropic HCP crystal structure, the very different CRSS for the various slip and twinning systems and the strong reorientation associated with the twinning. The texture of the material relative to the principal loading directions has a significant influence on the deformation of Mg and its alloys. A large anisotropy is observed in this material in mechanical properties such as flow stress, elongation to failure, and strain hardening behavior [13, 50, 55]. Therefore, it is important to consider the effects of texture when studying the deformation of polycrystalline Mg and its alloys, as noted by previous low strain rate studies [1, 21, 22, 29, 30, 48, 50]. A significant amount of work is being performed on improving the performance of Mg alloys through better control over processing induced textures [28, 56–58]. Extensive work has been performed on deformation of materials such as rolled AZ31 magnesium alloy sheets under a range of deformation

conditions. The strong basal texture induced by the rolling procedure results in strong anisotropy in the material response when deformed in different directions [50, 59, 60]. When compressed in the sheet normal direction (ND), the yield strength of AZ31 was observed to be higher than the yield strength under compression in the rolling and transverse directions (RD, TD). The strain hardening behavior in these two cases was also very different. These differences are attributed to the deformation mechanisms active under these loadings. In the ND compression, pyramidal slip and contraction twinning is the dominant deformation mechanism whereas under RD or TD compression, extension twinning is the dominant mode of deformation. The initial texture of the material with respect to the loading direction controls the dominant deformation mode in the early stages.

The overall material behavior is affected by the evolution of the dominant deformation mechanisms. Yoo [15] analyzed the ductility of various HCP metals on the basis of the observed deformation modes. He noted that HCP metals that deform through extension and contraction twinning of multiple types exhibit extensive ductility (e.g. Ti, Zr). Limited ductility is observed in materials that exhibit only one main type of twin (e.g. Be, Zn). Mukai et al. [61] suggested that the ductility of AZ31 Mg alloys can be improved by processing it by equal channel angular extrusion (ECAE) as compared to direct extrusion. The grain size is similar in both cases and this change in ductility is mainly caused by the difference in the textures induced by the processing. Enhancement in ductility is also observed upon addition of rare earth

elements such as yttrium and cerium to extruded magnesium [62, 63]. The increase in ductility in this case is also tied to the difference in the texture due to the addition of yttrium and cerium.

1.2.1.2 Effect of grain size

Grain size also has an effect on the dominant deformation mechanisms in magnesium. The effect of grain size on twinning in an Mg alloy was studied by Barnett et al. [20]. The propensity to twin was observed to decrease with reduction in grain size. Jain et al. [64] also observed the amount of twinning to increase with increasing grain size in a rolled AZ31B sheet. It is expected that there exist critical grain sizes that mark the transition from twinning to slip in magnesium and this transition is likely to be dependent on the texture of the material and the loading conditions [20]. The analysis of the effects of grain size on the dynamic behavior of magnesium is outside the scope of this work. Here, we focus on an extruded magnesium material with an average grain size of $\sim$20 μm.

1.2.1.3 Effect of strain rate

In order to successfully use magnesium and its alloys in applications involving dynamic loading, their performance under such conditions must be evaluated. Dynamic loading can induce complex deformation mechanisms in materials which might not be activated under quasi-static loading conditions [65]. In many cases, FCC and BCC

materials that do not deform by twinning under quasi-static loading are observed to deform extensively by twinning under dynamic loadings such as shock or very high strain rate deformation [66].

In the recent years, some studies have investigated the high strain rate behavior of Mg alloys [55, 59, 60, 67–72]. Ulacia et al. [59] observed that in AZ31, extension twinning remains the predominant mechanism at high rates and temperatures for loading geometries favoring this mechanism (as it does in the low strain rate regime). Tucker et al. [55] have also performed high strain rate tests on a rolled magnesium alloy AZ31B and observed significant rate effects (increase with increasing rate) on the compressive yield, strain hardening rate and ductility in the normal direction but not in the transverse and rolling directions. Jiang et al. studied twinning in AM30 alloys at moderate temperatures ($25^0 - 30^0$C) over a small range of strain rates [73]. The flow stress was observed to decrease with increasing temperatures and decreasing strain rates. Their observations indicate that the amount of twinning increases significantly with strain rate and decreases with increasing temperatures. The effect of temperature was also analyzed by Barnett et al., who observed that twinning dominated the flow at lower temperatures and slip dominated the flow at higher temperatures [20]. In a recent study by Dudamell et al. [60] on AZ31, enhanced extension twinning activity was observed at high strain rates. Similar observations of increase in twin volume fraction at higher strain rates were reported by Li et al. [70] in an ultrafinegrained ZK60 alloy. The increase in the twin density with increasing strain

rates was also observed in other HCP metals (e.g. α-titanium by Chichili et al. [74]). The review of the dynamic behavior of Mg and Mg alloys by Prasad et al. [72] suggests that Mg alloys undergoing plastic deformation dominated by extension twinning have relatively rate-insensitive strengths whereas those with dislocation activity as the primary mechanism of plastic deformation exhibit some rate dependence of flow stress. This suggests that high strain rate loading may have a strong influence on some deformation mechanisms in Mg and alloys. In magnesium, multiple modes of deformation are activated under many loading conditions. Dislocation slip is generally strain rate and temperature dependent. Some experimental observations indicate that twinning in magnesium is enhanced at high strain rates and low temperatures. The reason for this could be the difficulty to move dislocations at high strain rates and low temperatures making deformation twinning the favored mechanism. Due to the variation in the rate dependence of these modes, the overall response of the material is expected to be influenced by the rate of loading to a degree that depends upon the competition between the rate sensitivity of the active deformation modes.

Mg alloys have been the focus of the majority of prior studies, but the behavior of pure magnesium remains less well characterized. It is important to characterize the fundamental deformation mechanisms in pure Mg without the effects of solutes or precipitates. The deformation of pure magnesium under plane-strain compression was studied by a few researchers [13, 25, 28]. Their observations indicated significant differences in the deformation processes when the material is under c-axis extension

as compared to c-axis contraction. Also, suppression of a strong basal texture was observed to impart ductility to pure Mg by Gehrmann et al. [28]. Although there have been some studies on deformation of Mg alloys at high strain rates, a detailed study of the deformation mechanisms in pure magnesium at high strain rates is yet to be performed. Most of the high strain rate studies have been performed under uniaxial stress conditions. A few recent studies have explored the behavior of magnesium alloys under impact/shock loading [75–77]. Evidence of deformation twinning was observed by Hazell et al. in the recovered Elekton 675 material after shock loading. A detailed understanding of the deformation mechanisms in magnesium under complex stress states induced by dynamic loading is still lacking.

Our understanding of plastic deformation of materials has improved significantly due to the increasing sophistication of our experimental and computational tools. We can now gain information about material deformation at length and time scales that were previously not accessible. Advances in experimental characterization and observational techniques such as transmission electron microscopy (TEM) and scanning electron microscopy (SEM) can provide us information about defect structures at the atomic and mesoscopic scales. The insight gained from the pre and post-deformation analysis (of the mechanisms) using these tools in conjunction with experimental characterization of materials enables us to improve our understanding of the overall material behavior. This knowledge can be used to develop mechanism based constitutive models that predict material behavior under various loading conditions. Such models

are beneficial in evaluating material performance in cases such as dynamic loading in extreme environments where experimental evaluation is costly and/or dangerous.

1.3 Organization of the thesis

The aim of this dissertation is to improve the understanding of the dynamic behavior of magnesium. We focus on exploring the relationship between the dominant deformation mechanisms in this material and their effects on the material behavior. The work is presented in 7 chapters. In Chapter 1, the background and motivation behind this work is provided along with the discussion of the relevant studies till date and their implications. The experimental techniques used to investigate the behavior of this material are discussed in Chapter 2. The dynamic experimental techniques such as Kolsky bars and Plate Impact are discussed in detail. In Chapter 3, the microstructural evolution of pure magnesium when deformed under high strain rate loading under Kolsky bars is discussed. The observed mechanical behavior (stress-strain response and strain hardening) is related to the evolution of the underlying deformation mechanisms. The development of a simple mechanism based constitutive model is presented in Chapter 4. The model is applied to the deformation of single crystal and polycrystalline magnesium and is able to capture the effect of the dominant mechanisms. The dynamic deformation of polycrystalline magnesium under uniaxial strain conditions under normal plate impact loading is discussed in Chapter

5. The resulting microstructure is analyzed and compared with the observations of the deformed microstructures under the Kolsky bar loading. Elastic-plastic simulations (conducted in in Abaqus/Explicit) that probe the stress and strain evolution in the normal plate impact experiments are also presented. The plate impact technique is also used to perform experiments on pure single crystal magnesium and the findings are presented in Chapter 6. The summary of the work presented in this thesis and suggestions for future research are discussed in Chapter 7.

Chapter 2

Experimental Techniques

The experimental techniques and the sample preparation methods used in the dissertation are explained in this chapter. Polycrystalline pure magnesium and single crystal pure magnesium were the materials investigated in this work. The polycrystalline pure magnesium was purchased from GoodFellow in the form of an extruded rod of 99.9% purity. The single crystal magnesium was purchased from Metal Crystals and Oxides, Ltd. (Cambridge, UK) and was of 99.999% purity.

Electrical Discharge Machining (EDM) was used to cut the specimens for experiments from the bulk material. A single pass in a wire EDM was used to cut specimens for all experiments for both the polycrystalline as well as single crystal magnesium. The sample preparation techniques are described below.

2.1 Sample Preparation

2.1.1 Quasi-static and Kolsky bar compression experiments

The quasi-static compression and Kolsky bar compression experiments were performed on millimeter size cuboidal specimens of dimensions (6 mm x 3 mm x 3 mm) and (3 mm x 4 mm x 4 mm) respectively. These specimens were mechanically polished prior to loading to remove any recast layer from the EDM. Loctite 46040 Instant Adhesive was used to mount the specimens for polishing. This adhesive was chosen since it does not require application of heat for mounting or dismounting the specimen and can be dissolved quickly in acetone.

The loading faces of the specimens were polished using silicon carbide (SiC) paper and water as lubricant to a final polish of 15 μm (1200 grit) or better on an Allied Multiprep polishing machine.

2.1.2 Normal Plate Impact Experiments

The specimens for the normal plate impact experiments were cylindrical magnesium plates of 1 inch (or 25.4 mm) diameter and thickness in the range of 2 mm - 7mm. The specimens (target and flyer plates) were first lapped on a Lapmaster 15 lapping machine. A lapping slurry with 15 μm boron carbide abrasive and an oil based lapping vehicle was used. Both the front and rear surfaces of the target and

flyer plates were lapped. A total lapping time of 40 minutes on each side at 15 rpm produced the desired flatness for the pure magnesium material.

The rear surface of the target plate was then polished to a mirror-like finish for interferometry. This was achieved by mechanical polishing with SiC paper (15 μm) and water followed by polishing with diamond pastes (9μm, 3μm, 1μm) and Green Lube from Allied. The specimens were carefully cleaned in alcohol in an ultrasonic cleaner after the lapping and polishing steps to remove any abrasives from the surfaces.

The flyer plate was glued to a thin piece of balsa wood which was glued on to the front end of the projectile. The target plate was glued into a delrin holder along with a copper wire which provided the ground for the tilt circuit. The target plate had 4 through thickness holes along the circumference which are 90^0 apart. Insulated copper pins were glued into these holes with epoxy for the measurement of the tilt. The copper pins need to be flush with the impact surface of the target for the tilt measurement to work correctly. After the epoxy was set, the excess material from the copper pins was polished off such that the the pins were flush with the surface. The schematic of the tilt circuit is shown in Fig 2.8. The final step was lapping the impact surface of the target to ensure flatness. This was achieved by holding the target down by hand on the lapping wheel for approximately 5 minutes. The surfaces are carefully cleaned with acetone followed by ethanol to ensure and then air dried. The flatness can be checked with respect to a reference optical flat under a monochromatic light source. Flatness corresponding to two light rings or better is considered acceptable.

2.1.3 Microstructural analysis

Microstructural analysis of the as-received and deformed materials was performed using various techniques such as optical microscopy, X-Ray diffraction (XRD), Electron Back Scattered Diffraction (EBSD) inside a Scanning Electron Microscope (SEM) and Transmission Electron Microscopy (TEM). The final steps of the specimen preparation methods were somewhat different for each of the techniques.

The specimens were first sectioned (if necessary) with a low speed diamond saw in the case of polycrystalline magnesium and EDM in the case of single crystal magnesium. The specimens were then mechanically polished to remove any damage induced by machining or sectioning. This was followed by mechanical polishing performed in steps starting from a coarse (400 grit) SiC paper to a fine (1200 grit) SiC paper with water as the lubricant.

The mechanically polished surface using SiC paper was sufficient for XRD pole figure measurements since this technique is not very sensitive to the condition of the surface.

For optical microscopy and EBSD, the SiC polishing was followed by polishing with diamond pastes (9μm, 3μm, 1μm, 0.5μm) and Green Lube from Allied as the lubricant. Chemical etching was then performed on the specimens for optical microscopy. The etchant used for pure magnesium was 10% nitric acid in distilled

water. The material was exposed to the etchant for 20-30 seconds and immediately rinsed in ethanol and air dried. The specimens for EBSD were polished electrochemically in a LectroPol-5 electropolisher. The electropolishing was performed with a 5% nitric acid in methanol electrolyte at 0^0C and a voltage of 20V. The specimen was immediately put into an evacuated container or transferred to the SEM to prevent surface oxidation since this technique is very sensitive to the surface conditions.

The specimens for TEM were first polished down to a final thickness of 200μm. A twin jet Tenupol-3 electropolisher was used to electropolish these specimens with 10% nitric acid and methanol solution at -40^0C using liquid nitrogen for cooling. The specimens were then cleaned using low voltage ion milling with a low incidence angle for 0.5h while being cooled by liquid nitrogen. The TEM observations were made at an accelerating voltage of 120 kV using a Philips 420 microscope.

2.2 Quasi-static Testing

Quasi-static compression experiments were performed using an MTS servo-hydraulic testing machine at the strain rate of 10^{-3}s^{-1}. Cuboidal specimens were tested in compression under the displacement control mode. The ends of the specimens were lubricated with a multipurpose synthetic grease (AMSOIL) so as to minimize friction. The force-displacement data was collected using Station Manager, the MTS data collection software. The engineering strain was calculated using the displacement data

and the original sample length whereas the engineering stress was calculated using the force data and the initial cross sectional area of the sample. This data was then used to calculate the true stress-true strain response. The results from the quasi-static tests are presented in Chapter 3.

2.3 Compression Kolsky Bar Experiments

The compression Kolsky bar (also known as the Split-Hopkinson Pressure Bar) was used to study the behavior of magnesium at dynamic strain rates [3]. In this technique, the specimen is sandwiched between two long high strength steel bars called the input and output bars, which are designed to remain elastic throughout the test. A compressive stress wave is generated by impacting one end of the input bar with a projectile launched by a gas gun. This compressive wave travels down the input bar to load the specimen. The impedance of the bars is higher than that of the specimen by design. Therefore, several reverberations of the compressive stress pulse occur in the specimen; some part is transmitted to the output bar and the rest is reflected back into the input bar. Since the impedance of the bars is higher than that of the specimen by design, the compressive stress pulse keeps loading the specimen until substantial plastic flow of the specimen material has been achieved. The stress in the specimen is then uniform and information about this equilibrated stress state can be obtained from the signals from the strain gages mounted on the input and output bars. The signals recorded by the strain gages are analyzed to

obtain information about the strain, strain rate and the stresses in the specimen.

The wave propagation in the experiment is explained through the x-t diagram shown in Figure 2.1 [3]. The dashed lines show the location of the strain gages. The bars and the specimen are initially stationary. At time t=0, the projectile launched by the gas gun impacts the input bar. A compressive stress pulse is generated in the projectile and the input bar. The wave front is represented by a solid line of slope equal to the reciprocal of the longitudinal wave speed in the bar. The longitudinal wave speed in the bar can be calculated as

$$c_b = \sqrt{\frac{E_b}{\rho_b}} \tag{2.1}$$

where E_b is the elastic Young's modulus and ρ_b is the density of the bar material. The compressive stress wave is reflected as a tensile wave from the free surface at the back of the projectile. The tensile wave acts as the unloading wave in the input bar thus establishing the duration of the incident pulse as

$$\tau = \frac{2L}{c_b} \tag{2.2}$$

where L is the length of the projectile.

When the incident pulse reaches the input bar-specimen interface, a part of it is transmitted into the specimen and the remainder is reflected back into the input bar in tension. The compressive pulse in the specimen reaches the specimen-output bar interface and a part of it is reflected back as a compressive pulse and the rest is transmitted into the output bar. Several reverberations of this compressive pulse

occur from the input bar-specimen interface and the specimen-output bar interface thus increasing the compressive load experienced by the specimen. After several reverberations, it can be assumed that the stress in the specimen is uniform (stress equilibrium has been achieved) and this can be checked from the balance of forces at the specimen/input bar and specimen/output bar interfaces [3].

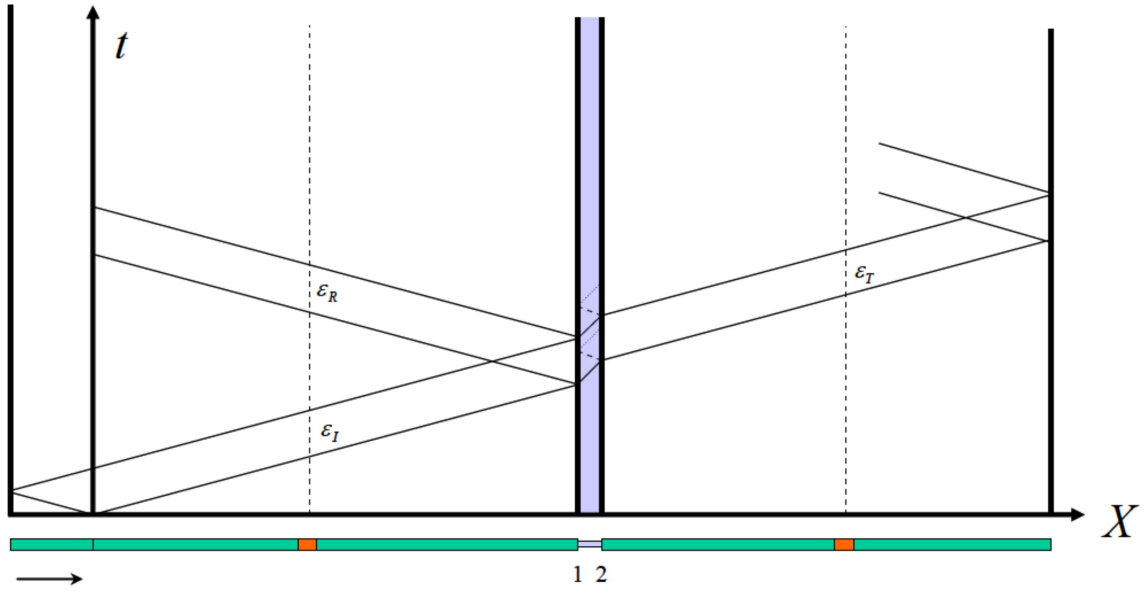

Figure 2.1: Wave propagation in a Kolsky bar experiment [3]

One dimensional wave propagation is typically assumed and the method of characteristics is used to relate the particle velocity and the strain in the pulses. Let ϵ_I, ϵ_T and ϵ_R be the strains in the incident, transmitted and reflected pulses respectively.

The particle velocity at the input bar-specimen interface by one-dimensional elas-

tic wave propagation is given as

$$v_1 = c_b(\epsilon_I - \epsilon_R) \tag{2.3}$$

At the specimen-output bar interface, the particle velocity is

$$v_2 = c_b\epsilon_T \tag{2.4}$$

If l_0 is the inital specimen length, the mean axial strain rate in the specimen is given as

$$\dot{e}_s = \frac{v_1 - v_2}{l_0} = \frac{c_b}{l_0}(\epsilon_I - \epsilon_R - \epsilon_T) \tag{2.5}$$

The elastic strains in the input, transmitted and reflected pulses are measured by the strain gages located on the input and output bars. The stresses in the input and output bars are then given as

$$s_i = E_b(\epsilon_I + \epsilon_R) \tag{2.6}$$

and

$$s_o = E_b\epsilon_T \tag{2.7}$$

The normal forces at the two interfaces can be calculated as

$$P_1 = E_b(\epsilon_I + \epsilon_R)A_b \tag{2.8}$$

and

$$P_2 = E_b(\epsilon_T)A_b \tag{2.9}$$

If the initial cross-section area of the specimen is A_{s0}, the mean nominal axial stress in the specimen is give by

$$\overline{s}_s(t) = \frac{P_1 + P_2}{2A_{s0}} = \frac{E_b}{2}\frac{A_b}{A_{s0}}(\epsilon_I + \epsilon_R + \epsilon_T) \tag{2.10}$$

After the stress has been equilibrated, we have $P_1 = P_2$. Therefore, from equations (2.8) and (2.9), we get

$$\epsilon_I + \epsilon_R = \epsilon_T \tag{2.11}$$

The above equations are used to obtain the nominal strain rate, strain and stress in the specimen as follows

$$\dot{e}_s(t) = -\frac{2c_b}{l_0}\epsilon_R(t) \tag{2.12}$$

$$e_s(t) = \int_0^t \dot{e}_s(\tau)d\tau \tag{2.13}$$

$$s_s(t) = \frac{E_b A_b}{A_s}\epsilon_T(t) \tag{2.14}$$

The true strain, the true strain rate and the true stress in the specimen can be obtained as given below.

$$\epsilon_s(t) = -ln[1 - e_s(t)] \tag{2.15}$$

$$\dot{\epsilon}_s(t) = \frac{\dot{e}_s(t)}{1 - e_s(t)} \tag{2.16}$$

$$\sigma_s(t) = s_s(t)[1 - e_s(t)] \tag{2.17}$$

where the compressive strain e_s is considered positive. The experiments to obtain the high strain rate compressive behavior of pure magnesium were performed on maraging steel input and output bars with a diameter of 9/32 in. (7.144mm). The typical range of specimen aspect ratio (length/diameter) for Kolsky bar testing is 0.6 - 1. The dimensions of the specimens used here were 3mm x 4mm x 4mm. We also kept track of the extrusion direction and radial directions on each specimen when working with the extruded rod of commercially pure polycrystalline magnesium. A momentum trap bar was also used to prevent reloading of the specimen due to the wave reflected from the free end of the transmitted bar.

2.3.1 Kolsky Bar Experiments for Small Plastic Strains

In order to achieve small plastic strains at high strain rates, we have also carried out some controlled strain tests on the compression Kolsky bars with collars similar to the work in Ref [78]. Collars are made of high strength material like tool steel (typically the same material as the bars) and are designed to remain elastic while the specimen undergoes plastic deformation. The length of these collars is shorter than the specimen length and is designed to allow the specimen to achieve a specific

strain. The schematic of this configuration is shown in Fig 2.2 below. The collar is placed around the specimen such that it interfaces with the output bar but not the input bar and also does not contact the specimen. During testing, the compressive stress pulse propagates through the specimen and causes plastic deformation of the specimen until the collar comes into contact with the input bar interface. The length of the specimen after deformation is equal to the length of the collar. Note that care must be taken to ensure that the lateral sides of the specimen do not come into contact with the collar. If the lateral expansion of the specimen is restricted due to the surrounding collar, the stress state will no longer be uniaxial and effects of lateral confinement will have to be considered in the analysis.

Collars made out of high strength steel by EDM were used, with inner and outer diameters of 6.5 mm and 12.6 mm respectively. Note that the outer diameter of the collar is equal to the bar diameter. Collars of two different lengths (2.895 mm and 2.73 mm) were used to achieve final plastic strains of approximately 3.5% and 9% at a strain rate of about $2\text{x}10^3 s^{-1}$. The results from the Kolsky bar experiments are presented in Chapter 3.

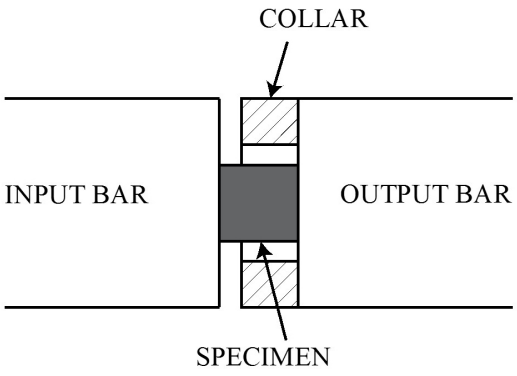

Figure 2.2: Schematic of the controlled strain test setup using collars in the Kolsky bar experiment. The final length of the specimen after deformation is equal to the length of the collar

2.4 Plate Impact Experiments

The plate impact technique can be used to perform various types of experiments - wave propagation type experiments to study interaction of waves with materials, and pressure-shear plate impact experiments to study the behavior of materials under very high strain rate loading. This work was focused on investigating the material behavior under wave propagation induced by normal impact. In the normal impact configuration, a cylindrical plate (the flyer) of a material is mounted on a projectile. Another cylindrical plate (the target) is stationary and is situated inside a target chamber which is evacuated during the experiment. The projectile carrying the flyer

plate is launched with a velocity V by a gas gun and impacts the target plate. The velocity range for the plate impact system used here is from tens of meters per second to about 300 m/s.

In the normal impact configuration used here, the target and the flyer plates are parallel to each other and therefore, upon impact, uniaxial strain compressive waves are propagated in both plates. The velocity of the wavefront is a characteristic of the material and is given by

$$c_{el} = \sqrt{\frac{\lambda + 2\mu}{\rho}} \tag{2.18}$$

where λ and μ are the *Lame'* constants and ρ is the density. The x-t diagram in the case of purely elastic wave propagation is shown in Fig 2.3. Lines Ot_1 and Ot_1' represent the compressive wavefronts and lines t_1A and t_1'A represent the tensile wavefronts. The flyer and target plates are both made of the same material (Magnesium) and are designed to have the same thickness. The rear surface of the target is stress free and thus the longitudinal compressive wave is reflected as a tensile wave from it. This also is the case for the back surface of the flyer which is backed by balsa wood with a very low impedance. These reflected waves from the target and flyer rear surfaces arrive at the impact face at approximately the same time by design. The interface between the target and the flyer cannot support tension and therefore separates thus ending the window of interest for the experiment.

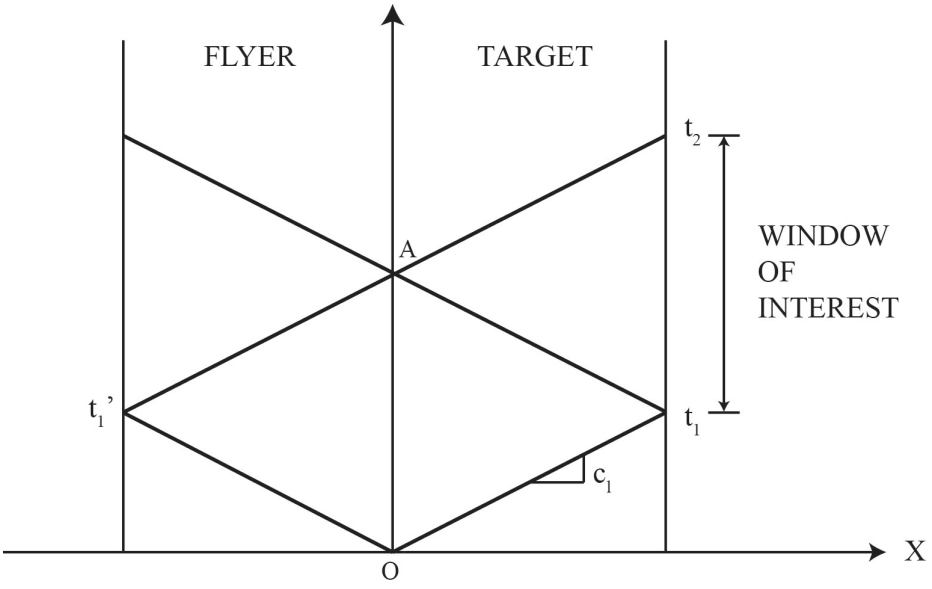

Figure 2.3: Schematic of the normal plate impact recovery setup

The stress generated due to the impact can be estimated using the method of characteristics from the equations below for the case of purely elastic wave propagation.

$$\sigma \pm \rho c_{el} v = constant \tag{2.19}$$

For the case of symmetric impact, as shown in Fig 2.3 the stress in the region bounded by lines Ot_1 and t_1A in the target and lines Ot_1' and t_1'A in the flyer is given by the equation below.

$$\sigma = \frac{1}{2}\rho c_{el} v \tag{2.20}$$

where ρ is the density of the material, c_{el} is the longitudinal elastic wave speed and v is the impact velocity. In the case of elastic-plastic wave propagation, a more

complex analysis is needed to probe the stress state.

We are interested in the case where the loading causes inelastic deformation of the material. If the impact velocity is greater than the velocity needed to cause yield of the material, the wavefront will decompose into elastic and plastic waves. The elastic wave propagates at a higher wave speed which is the characteristic wave speed (such as c_{el}) in the material. If the impact velocity is significantly high, shocks will be generated in the material. The impact velocities in our experiments are in the domain of elastic-plastic wave propagation and shocks are typically not generated.

The thickness of the plates is small (in the range of 2 mm - 7 mm) in relation to the diameter (25.4 mm). Therefore, the state of strain can be considered to be uniaxial at the point of interest until the unloading waves arrive from the peripheries. The state of uniaxial strain in the experiment is maintained at the center of the plates only for a finite time. The arrival of release waves from the boundary of the plates at the point of interest ends the uniaxial strain state. The diagnostics in the experiment consist of measuring (i) the velocity of the projectile prior to impact, (ii) the misalignment between the impact faces (known as tilt) and (iii) the particle velocity history at the rear surface of the target plate.

2.4.1 Normal Plate Impact Recovery Experiment

In order to study the effect of the wave propagation caused by the dynamic loading on the microstructure of the material, we need to investigate the mechanical response

of the material as well as the microstucture of the deformed material. Therefore, we need to be able to recover the material after the loading is complete. It is difficult to avoid material deformations after the data collection ends in dynamic experiments. In order to avoid deformation of the material beyond the known loading, a high amount of energy (e.g. kinetic energy of the projectile) needs to be dissipated quickly. This is typically achieved by ramming the projectile into a catching device containing energy absorbing materials/mechanisms in non-recovery type plate impact experiments.

The plate impact recovery setup used here was designed by Jia and Ramesh [79] and a schematic is shown in Fig 2.4. In the recovery configuration, the flyer backed by balsa wood is glued to the extended front end of the projectile that fits into the PVC tubing. The projectile front end for recovery has a flat shoulder machined on it which comes into contact with the stopper just after the impact. The stopper is designed to absorb the kinetic energy of the entire projectile and reduce the projectile velocity to zero. The details of the structure of the stopper assembly can be found in Jia et. al. [79]. The target plate is held separately in a target holder that allows for the initial alignment of the target and flyer impact faces.

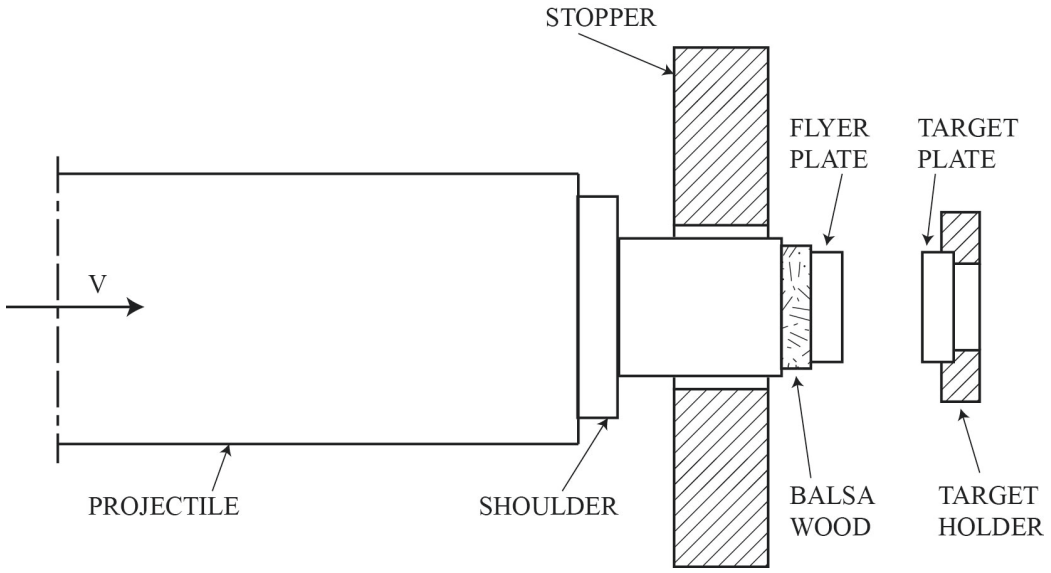

Figure 2.4: Schematic of the normal plate impact recovery setup

The projectile velocity is measured just before impact with a laser line velocity measurement system The particle velocity at the rear surface of the target plate is measured using a normal displacement interferometer (NDI) and the misalignment between the impact faces is measured using a tilt circuit as described below.

2.4.2 Projectile Velocity

A laser line velocity measurement system originally designed by Ramesh and Kelkar [80] is used to measure the velocity of the projectile just before impact. A schematic of the system is shown in Fig 2.5. A laser sheet is genereated using a diode laser and optics on one side of the target chamber. A photodiode is mounted across the target chamber which monitors the intensity of the laser sheet. As the projectile

intersects the laser sheet, it obstructs part of it from reaching the photodiode thus reducing the intensity measured by the photodiode. When the laser sheet is completely obstructed, the intensity measured by the photodiode drops to zero. The time (t) needed to completely obstruct the laser sheet of known length (L) enables us to calculate the velocity of the projectile as $v_{projectile} = \frac{L}{t}$. An example of the signal from the laser line velocity system measured during a plate impact experiment is shown in Fig 2.6.

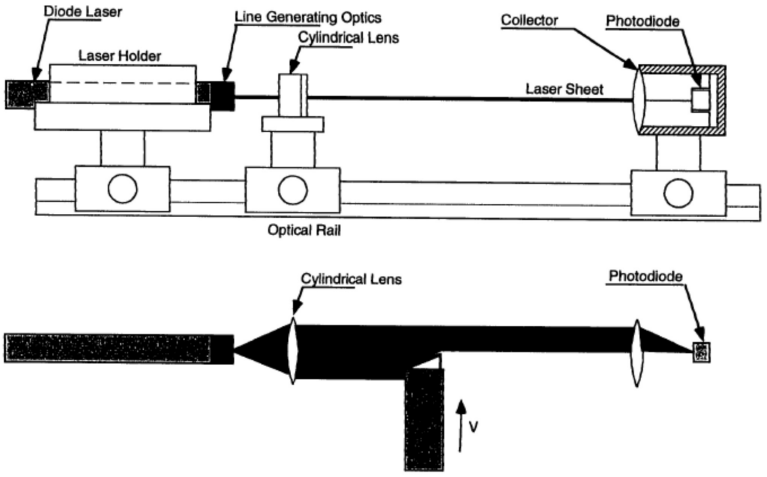

Figure 2.5: Schematic of the laser line projectile velocity measurement system [4]

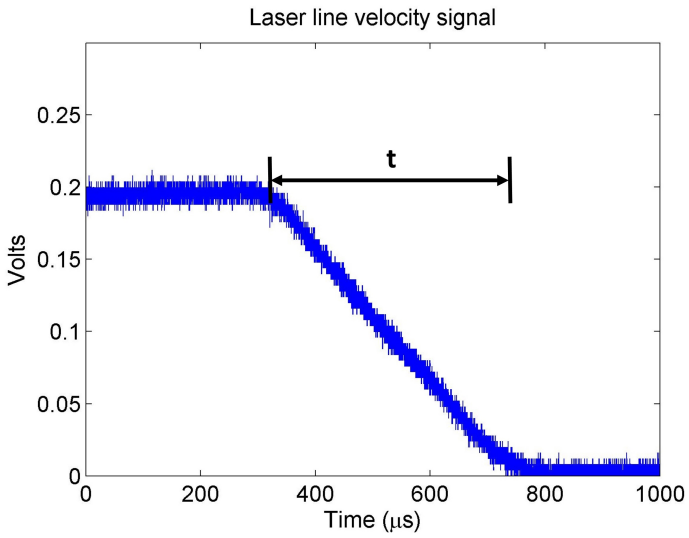

Figure 2.6: An example of the laser line velocity signal measured during a plate impact experiment

2.4.3 Tilt measurement

In the plate impact experiments it is very important to minimize the misalignment between the impact faces to ensure planar wave propagation. The impact faces of the flyer and target plates are aligned using an autocollimator technique first developed by Kumar and Clifton [81]. In this technique, mirrors are mounted on the impact faces of the target and the flyer plates. A partially mirrored prism is used to align the impact faces of the flyer and the target plates. A detailed description of the procedure can be found in Ref [81]. A schematic of the setup for the alignment is shown in Fig 2.7. Even after aligning the impact faces well, there is typically some misalignment that occurs during the experiment and it is important to measure this misalignment or tilt.

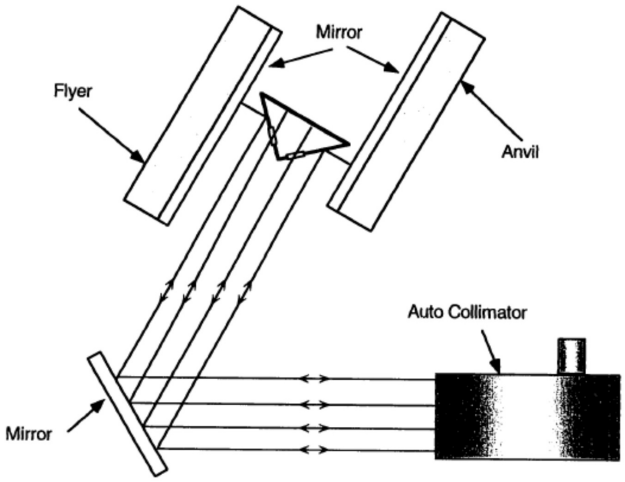

Figure 2.7: Auto-collimator setup used for the alignment of the impact surfaces [4]

A tilt circuit is used to measure the misalignment between the impact faces of the flyer and the target. The tilt circuit consists of four insulated copper pins embedded inside the target as shown in Figure 2.8 which are biased with a voltage. The target plate is connected to the tilt circuit via a ground wire. Upon impact, the circuit for each of the pins closes when the pin makes contact with the flyer plate. The voltage versus time data is recorded as shown in the figure.

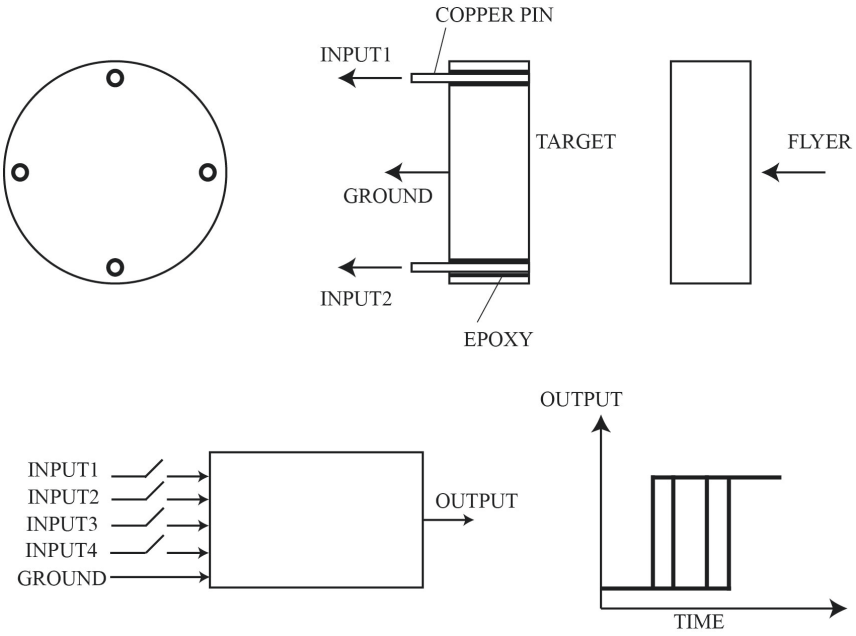

Figure 2.8: Tilt Circuit

The maximum tilt angle can be calculated using the following formula.

$$sin\theta \approx \theta = \frac{v\Delta t_{max}}{d} \tag{2.21}$$

where Δt_{max} is the maximum time between the closure of two pins, v is the impact velocity and d is the diameter of the plates.

A tilt of <2 milliradian is considered acceptable for the plate impact experiments. For the example shown in Figure 2.9, $\Delta t_{max} = 0.3$ μs, $d = 25.4$ mm and $v = 60$ m/s giving $\theta = 0.7$ milliradians.

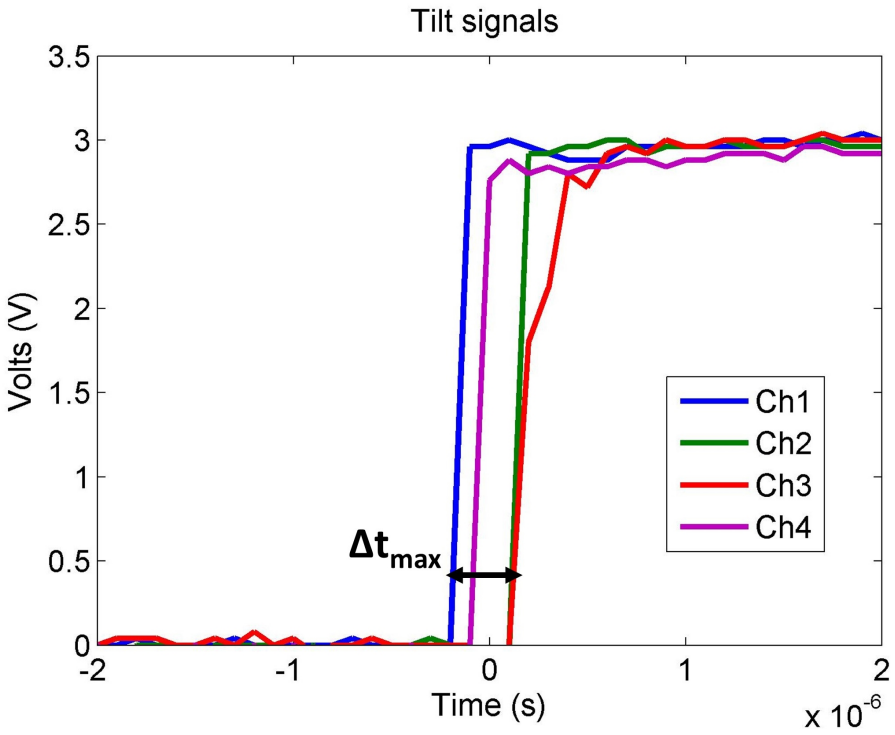

Figure 2.9: An example of the tilt signals measured by the tilt circuit for a normal plate impact experiment

2.4.4 Interferometry

The measurement of the normal particle displacement at a point on the rear surface of the target is achieved by setting up a normal displacement interferometer (NDI) also known as Michelson interferometer. The laser used is a Genesis CX532 high power optically pumped semiconductor laser with a wavelength of 532 nm (green). The interferometric setup is shown in Figure 2.10.

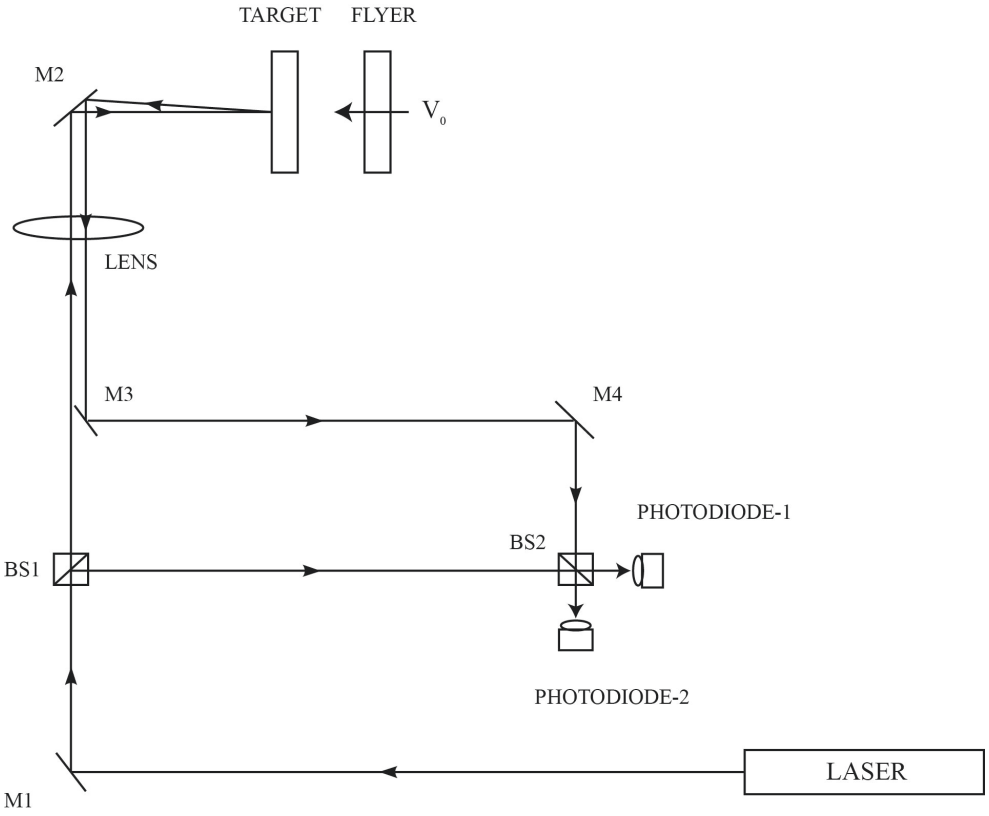

Figure 2.10: Schematic of the normal displacement interferometry (NDI) setup

The collimated beam generated by the laser is directed by the mirror M1 to the beamsplitter BS1 where it is split into two parts. The reference beam travels to the beamsplitter BS2 whereas the remaining part - (the test beam) travels to the rear surface of the target though a lens mounted on the target chamber and the mirror M2. The mirror M2 is a disposable mirror situated inside the target chamber. The test beam is reflected off the target rear surface (which has a mirror-like finish) and travels back through the lens on to the mirror M3. The test beam is then directed towards

the beamsplitter BS2 by the mirror M4 where it interferes with the reference beam. The resultant beams are interrogated by the two photodiodes. The interference of these beams results in the maxima/minima in the intensity when they are in/out of phase. The intensity of the combined beam will vary as a result of the motion of the target. The two photodiodes are used to record this intensity variation and the optical path of the reultant beams are such that the resulting signal measured by the photodiodes should be 180^0 out of phase with each other. The displacement vs. time history is obtained and the normal free surface velocity can be calculated by differentiation of the data.

2.4.4.1 Data Reduction

Three different oscilloscopes are used to record the data from the three diagnostic systems - the laser line velocity measurement, the tilt circuit and the NDI. The oscilloscopes used to record the later two are controlled through a Labview program whereas the oscilloscope for the laser line velocity measurement is operated independently. The specifications for the oscilloscopes used are given in the table below. The oscilloscopes recording the tilt and the NDI signals are triggered by a signal from the tilt circuit when a tilt pin makes contact with the flyer closing its circuit.

Measurement	Oscilloscope	Bandwidth	Sampling Rate
Tilt circuit	Tektronix TDS 684B	1 GHz	5 GS/s
Laser line velocity	Tektronix DPO 3014	100 MHz	2.5 GS/s
Interferometry	Tektronix DPO 4104	1 GHz	5 GS/s

The signals measured by the photodiodes in the NDI are in the form of a voltage history as shown in Fig 2.11. The two channels represent the measurements from the two photodiodes which are 180^0 out of phase. The zoomed in view of the data recorded by one of the photodiodes is shown in Fig 2.12. A 2π phase variation in the intensity profile is termed as a fringe. A displacement of $\lambda/2$ corresponds to a 2π phase variation in the intensity. The intensity vs. time data from the photodiodes is then processed using a MATLAB script which counts the number of fringes as a function of time.

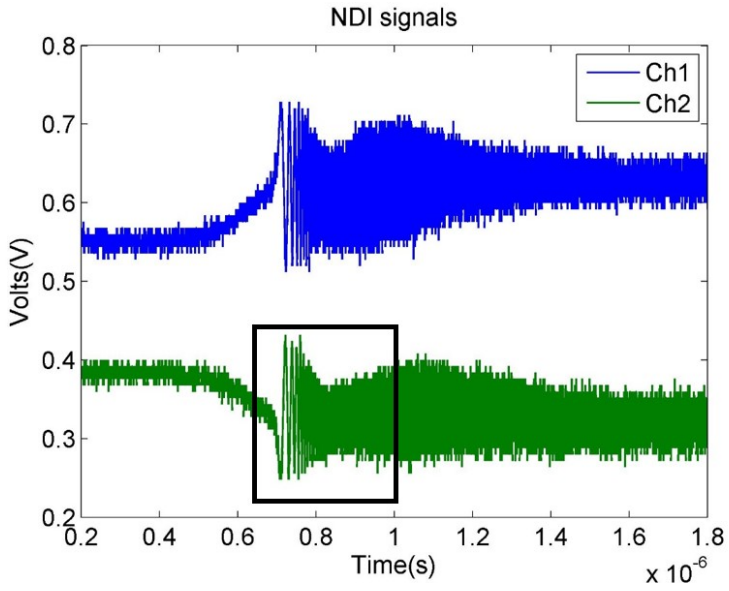

Figure 2.11: Signals measured by the photodiodes from the Normal Displacement Interferometer (NDI)

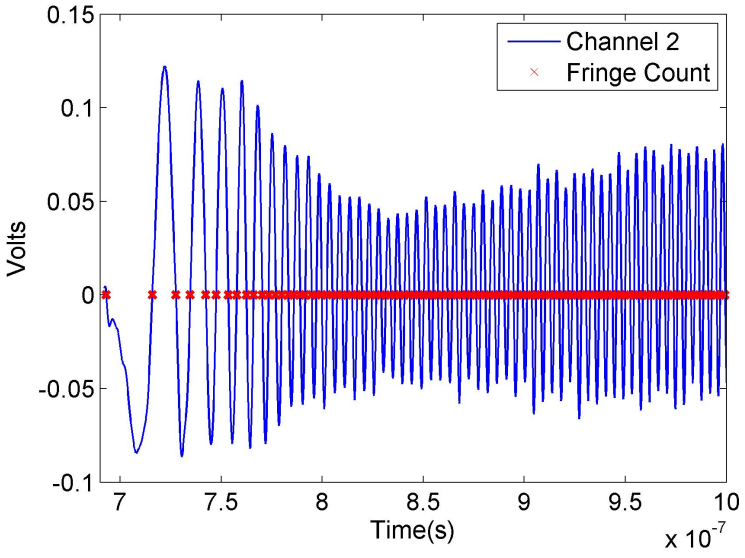

Figure 2.12: Zoomed in view of the intensity vs. time profile measured from the NDI (Channel 2) in Fig 2.11. Each half fringe is marked by the red crosses

The displacement of the rear surface can be related to the intensity variation through the following equation

$$s(t) = \frac{1}{2}\lambda F(t) = 266F(t) \tag{2.22}$$

where s(t) is the rear surface displacement as a function of time and F(t) is the fringe count. In order to obtain better resolution of the calculated displacement from the data, every half fringe can be counted and the modified form of the above equation can be used to calculate the displacement as $s(t) = \frac{1}{2}\lambda\frac{F(t)}{2}$. The red crosses in Fig 2.12 represent each half fringe.

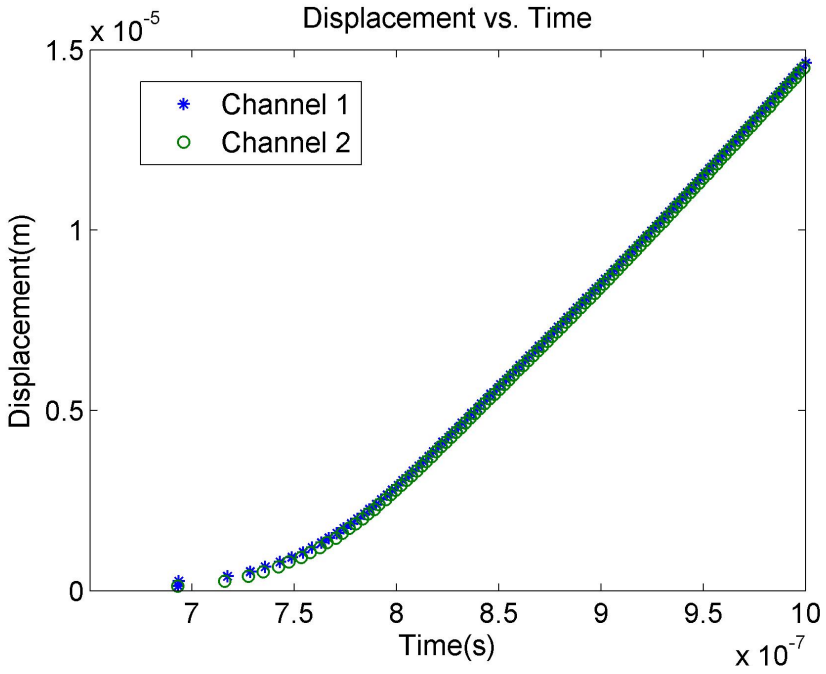

Figure 2.13: Displacement history at the free surface of the target plate as calculated from the NDI signals

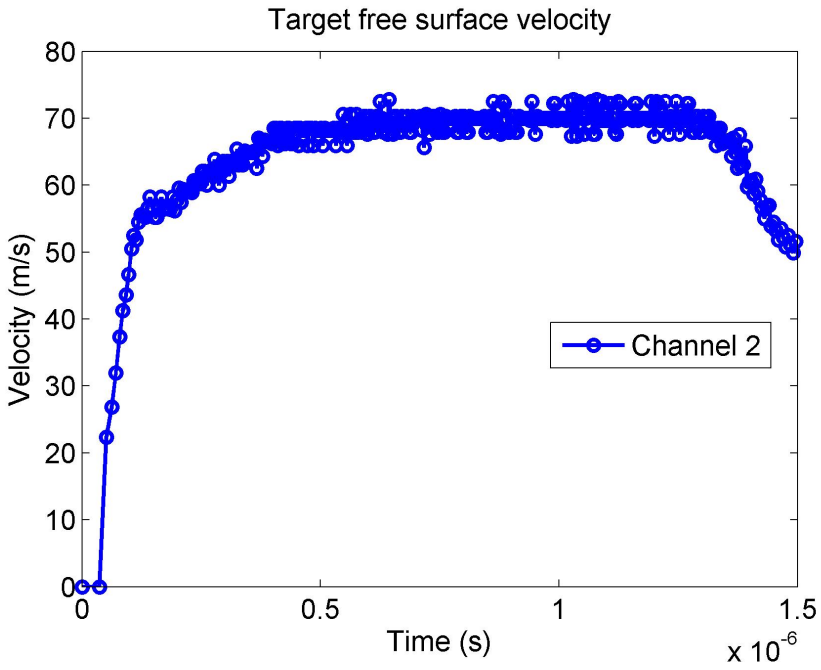

Figure 2.14: Particle velocity history at the free surface of the target plate as calculated from the NDI signals

The displacement history of the target rear surface is calculated from the above data is shown in Fig 2.13. The rear surface velocity history at the target rear surface is then obtained from numerical differentiation of the data. A 5 point central difference scheme is used to numerically differentiate the displacement time history in order to obtain the velocity history shown below (Fig 2.14). The raw data is collected through a Labview program and saved on a the local hard drive of the computer. It is then archived in an experimental database.

The techniques described in this chapter are used to conduct experiments on polycrystalline and single crystal magnesium. The results from the quasi-static and Kolsky bar experiments are presented in Chapter 3. The results of normal plate

impact experiments on polycrystalline magnesium are discussed in Chapter 5 and those from the impact of single crystal magnesium are presented in Chapter 6. We discuss the behavior of extruded magnesium under high strain rate loading and its microstructural evolution in the next chapter (Chapter 3).

Chapter 3

Microstructural evolution of pure magnesium under high strain rate loading

3.1 Introduction

The behavior of magnesium and its alloys is sensitive to the initial texture and its evolution during deformation due to the activation, evolution and interaction of various deformation mechanisms. It is important to understand the fundamental deformation mechanisms active during dynamic deformation in order to successfully use these materials in the applications of interest such as automotive and aerospace components, armor etc. To this purpose, an experimental study of the fundamen-

tal deformation modes in pure magnesium is performed. Quasi-static compression experiments are first performed on pure magnesium in the extrusion direction (ED) in order to establish a baseline for the material response. This is followed by high strain rate compression experiments and investigation of the microstructural evolution through transmission electron microscopy (TEM) and electron back scattered diffraction (EBSD) analyses. In order to investigate the evolution of the microstructure with deformation, controlled strain tests have also been performed under high strain rate loading. The microstuctural evolution (of texture, twins and dislocations) is then used to explain the observed mechanical behavior of the material.

3.2 Experiments

3.2.1 Initial texture

A hot-extruded Mg rod of commercial purity (99.9%) was used in this study. The microstructure of the material consists of equiaxed grains with an average grain size of about 20μm. The initial texture of the material was analyzed using X-ray diffraction (XRD) in the extrusion direction (ED) and is shown in Fig 3.1. The initial microstructure was found to be typical for an extruded HCP material with a random in plane orientation spread of the basal (0001) poles perpendicular to the ED [49]. The spread of the basal poles in the radial direction (RD) was observed to be quite uniform.

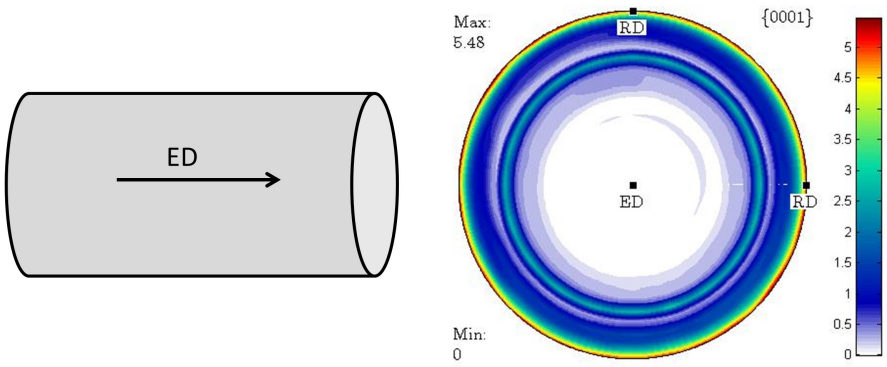

Figure 3.1: (0001) pole figure of the as-received material in the ED as measured by XRD

3.2.2 Quasi-static and high strain rate experiments

Uniaxial compression experiments at quasi-static and high strain rates were performed on extruded pure magnesium. The quasi-static tests were performed using a servohydraulic machine whereas the high strain rate/dynamic experiments were performed using a conventional Kolsky bar (also known as a Split-Hopkinson pressure bar).

The nature of dynamic compression tests involving Kolsky bars is such that the total strain imposed is dictated by the strain rate and duration of loading and the tests typically lead to large strains (> 0.1). In order to analyze the microstructural evolution of the material under high strain rate loading, we need to recover specimens deformed to various strains at high rates of loading. Smaller strains were achieved

by using collars of hardened steel surrounding the magnesium sample during testing similar to the work in Ref [78]. These controlled dynamic strain tests were carried out at a strain rate of about $2x10^3 s^{-1}$ and plastic strains of approximately 3.5% and 9% were achieved. These values were chosen since at $\sim$ 3.5% strain, the plastic deformation is in the initial stages and the strain hardening rate is rising rapidly while at $\sim$ 9% strain, the strain hardening rate is at its maximum value. Microstructural investigation at these strains enables us to gain an understanding of the deformation processes responsible for the observed mechanical behavior.

3.2.3 Microstuctural analysis using EBSD and TEM

The microstructure of the material was examined before and after testing using EBSD and TEM. Detailed microstuctural analysis at intermediate strains was performed for samples deformed under high strain rate loading. The samples for EBSD and TEM analyses were prepared by carefully sectioning tested and untested specimens with a low speed diamond saw. These specimens were then mounted and mechanically polished down to about 200μm thickness by a series of sand papers down to 1200 grit. A Tenupol-3 electropolisher was used to electropolish these specimens with 10% nitric acid and methanol solution at -40^{0}C using liquid nitrogen for cooling. Low incidence angle, low voltage ion milling was then used for 0.5 h to clean the samples while being cooled by liquid nitrogen. A Philips 420 microscope was used to make the TEM observations at an accelerating voltage of 120 kV. The EBSD

data was collected by an EDAX system mounted on a Hitachi 4700 FE scanning electron microscope and analyzed using TSL-OIM software. The step sizes used for data collection were in the range of 0.3 μm - 0.5 μm.

3.3 Results

3.3.1 Mechanical behavior under quasi-static and high strain rate loading

Quasi-static compression experiments were performed at strain rates of the order of 1x10$^{-3}s^{-1}$. The true stress-true strain behavior in the extrusion direction (ED) is shown in Fig 3.2. The yield stress was found to be about 65 MPa and a peak stress of about 260 MPa was observed at a strain of about 0.15. The flow stress is observed to increase with increasing strain. The material did not fail under this loading until a strain of $\sim$0.16 after which it was unloaded.

High strain rate compression experiments were performed at room temperature in the ED. The material was tested at strain rates of approximately 2x10$^{3}s^{-1}$ and 4x10$^{3}s^{-1}$ and the response was found to be very similar at these rates as seen in Fig 3.3a. The stress-strain data from a 2x10$^{3}s^{-1}$ test is presented in Fig 3.3b as a representative case (solid blue line). Note that these Kolsky bar experiments do not accurately capture the elastic response, but the apparent yield stress under dynamic

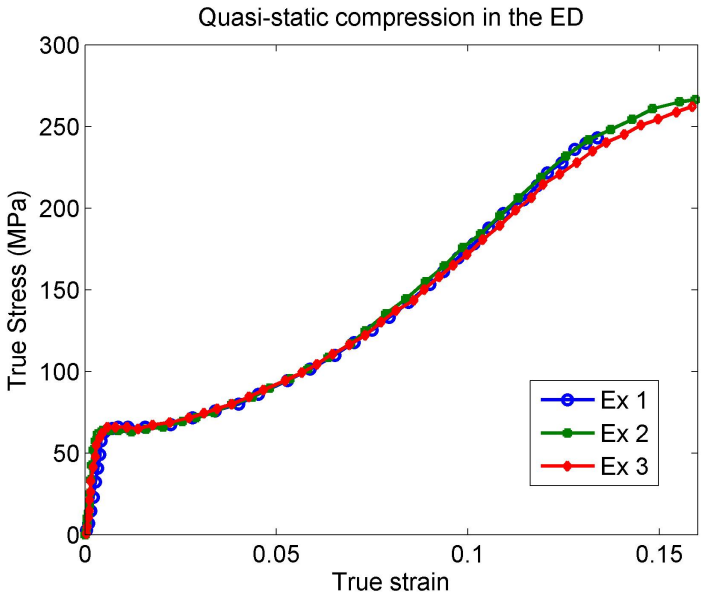

Figure 3.2: True stress - true strain response under quasi-static compression in the ED at strain rates of 1x10$^{-3}s^{-1}$

compression of 2x10$^{3}s^{-1}$ was found to be about 65 MPa (at a true strain of 0.002), and was similar in the 4x10$^{3}s^{-1}$ tests. After an initial nearly perfectly plastic response, the flow stress was observed to increase with increasing strain to a value of ∼315 MPa at a true strain of 0.15 (Fig 3.3b). Unloading of the sample began at a strain of approximately 0.15 and the material did not fail under this 2x10$^{3}s^{-1}$ loading. The sigmoidal shape of the true stress-true strain curve observed for both the quasi-static and dynamic cases is typical of textured Mg and its alloys under twinning dominated deformation [21, 50, 59]. The significant amount of strain hardening in the material can be noted from the true stress - true strain curve.

The true strain hardening rate (defined here as the rate of change of true stress as

a function of true strain, $d\sigma/d\epsilon$) under high strain rate loading of $2x10^3 s^{-1}$ for this material is also presented in Fig 3.3b as the green dashed line. Only the stress-strain data in the clearly plastic regime were considered for this calculation. The true strain hardening rate was calculated by the numerical differentiation of the true stress data with respect to the true strain data. The true strain hardening rate increases sharply with strain during the early stages of deformation. It reaches a maximum value at a strain of about 9%, and then decreases.

In order to understand the microstructural evolution of this material under dynamic loading, the samples deformed to plastic strains of approximately 3.5% and 9% were analyzed using EBSD (for the evolution of texture and twins) and TEM (for the evolution of dislocations and twins).

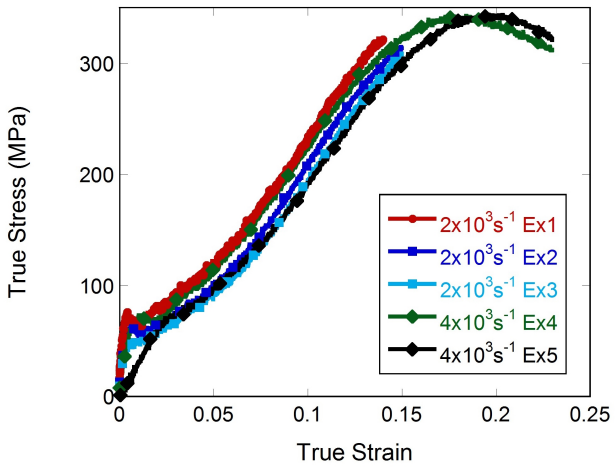

(a)

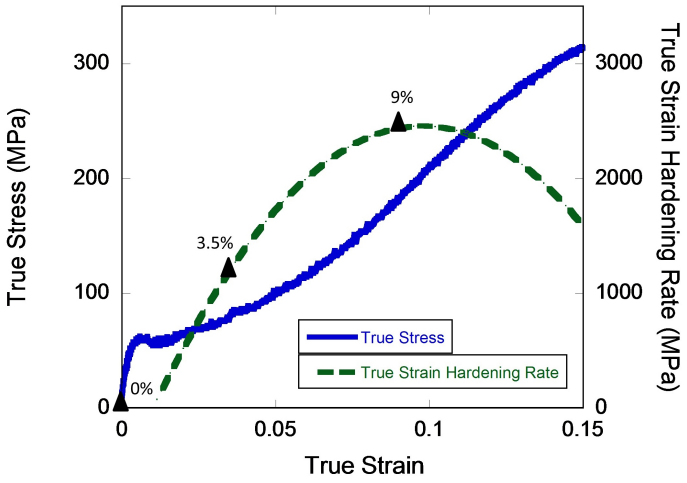

(b)

Figure 3.3: (a) True stress - true strain response under dynamic compression in the ED at strain rates of 2x10$^3 s^{-1}$ and 4x10$^3 s^{-1}$ (b) A representative stress-strain curve (solid blue line) is shown. The true strain hardening rate as a function of true strain is shown by the green dashed line. Markers represent the values of intermediate strain at which the tests were stopped for microstuctural analysis

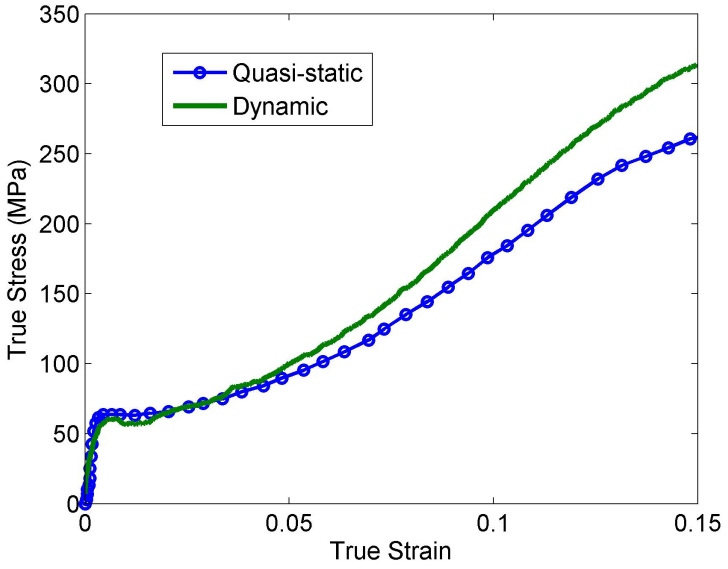

Figure 3.4: Comparison of the true stress - true strain response under compression in the ED at quasi-static and dynamic strain rates

A comparison of the response of the material under quasi-static and dynamic loading is shown in Fig 3.4. The flow stress at yield is observed to be very similar for the $10^{-3}s^{-1}$ loading and $10^{3}s^{-1}$ loading. Therefore, the flow stress at yield for the extruded material when compressed in the ED is not sensitive to the strain rate. There are significant differences in the strain hardening behavior with the degree of strain hardening being much higher under the dynamic loading. Therefore, the strain hardening behavior in ED compression is strain rate sensitive. This indicates that some of the the deformation mechanisms active under ED compression are sensitive to the rate of loading. Therefore, we expect to observe differences in the microstructural evolution at different rates of loading. Although the comparison of the microstructural

evolution under quasi-static loading with the evolution under dynamic loading is of interest, in this work, only the microstructural evolution under the high strain rate loading is analyzed.

3.3.2 Texture Evolution

The initial texture of the material was analyzed using EBSD. The inverse pole figures and the (0001) pole figures at the different values of strain allow us to visualize the overall change in the texture.

Fig 3.5(a,b,c) shows the EBSD inverse pole figures (or the out-of-plane crystal orientation maps) of the as-received material in the ED. These inverse pole figures are measured in the ED in different regions of the as-received material. The starting microstructure is essentially twin free and most grains are oriented with their c-axes in a radial direction (RD) that is perpendicular to the ED. Fig 3.5(d,e,f) shows the pole figure for the as-received material that corresponds to the inverse pole figures in Fig 3.5(a,b,c) in which the maximum intensity of the basal poles is in the RD, typical for extruded Mg and its alloys [49]. There are local variations in the in-plane orientations of grains that can be observed from the clustering of the (0001) poles in different regions around the circumference in the three scans. As the EBSD measurements are typically performed over small regions and the extruded material has a weaker texture as compared to the rolled material, we expect to see these variations in the measurements. The effect of these local variations averages out

when the measurement is performed over a large enough area as in the XRD pole figure measurement in Fig 3.1 showing a random spread of basal poles in the RD.

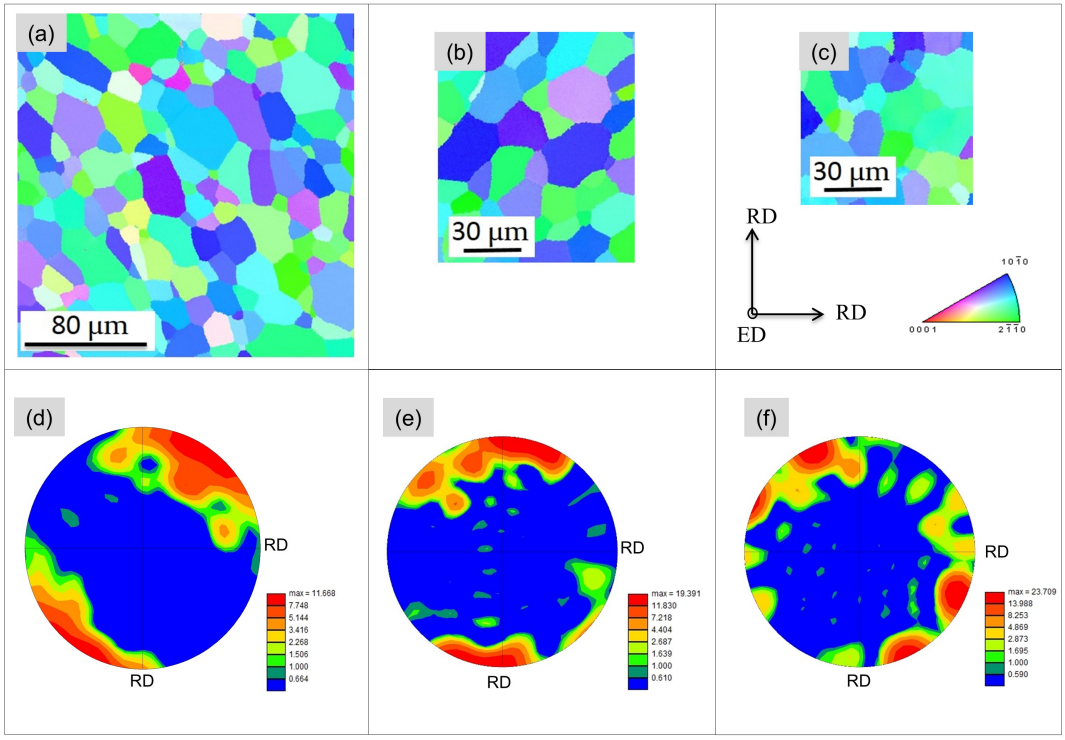

Figure 3.5: EBSD inverse pole figure (or out-of-plane crystal orientation) maps in the ED of as-received samples are shown in Fig 3.5 (a,b,c). The (0001) pole figures calculated from the EBSD data for the regions shown in Fig 3.5 (a,b,c) are presented in Fig 3.5 (d,e,f) respectively

Fig 3.6(a,b,c) shows that in the samples deformed at the strain rate of $2x10^3 s^{-1}$, to a plastic strain of about 3.5% a large number of twins are present in the microstructure. These twins are extension twins as can be understood from the misorientation

angle distributions discussed in the later sections. The (0001) pole figures show the appearance of the basal pole intensity away from the RD which indicates a change in the overall texture due to formation of extension twins. It can be seen from Fig 3.6(a) that in some grains, the basal poles of the twinned regions are reoriented to a different RD direction and not in the ED although the orientation of the twinned region is $\sim 90^0$ away from the orientation of the parent. This can also be observed by the appearance of high intensity of basal poles in RDs that are $\sim 90^0$ apart in Fig 3.6(d). Many of the twinned regions are reoriented such that their basal poles are now towards the ED as seen in Fig 3.6(e,f).

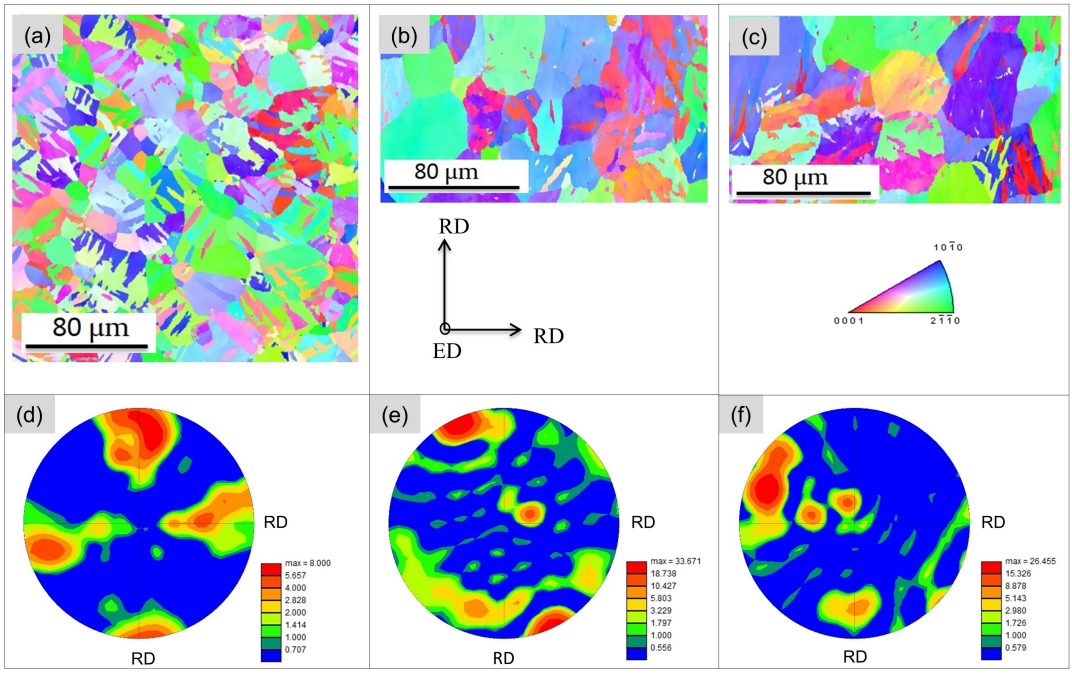

Figure 3.6: EBSD inverse pole figure maps in the ED of the samples deformed to 3.5% strain under high rate loading are shown in Fig 3.6(a,b,c). The (0001) pole figures calculated from the EBSD data for the regions shown in Fig 3.6(a,b,c) are presented in Fig 3.6(d,e,f) respectively

By about 9% strain, the entire microstructure is almost entirely twinned (Fig 3.7(a,b)). The extension twins have grown and consumed entire grains in many cases and thus very few grains are now present with their original orientation. The large change in the overall texture of the material due to twinning is indicated by the strong intensity of the (0001) pole in the ED in Fig 3.7(c,d).

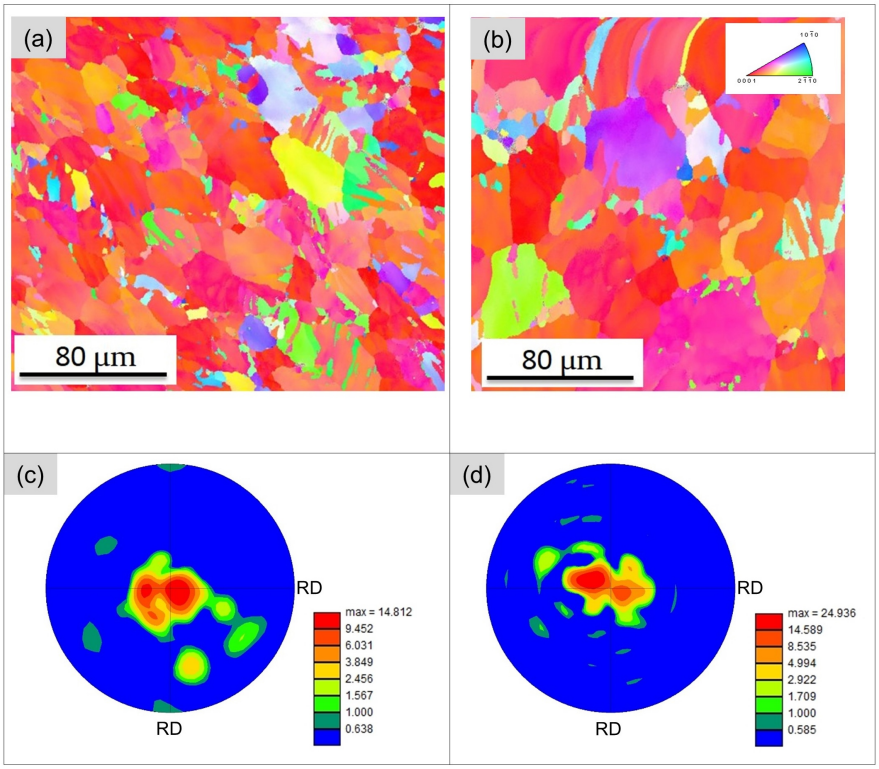

Figure 3.7: EBSD inverse pole figure maps in the ED of the samples deformed to 9% strain under high rate loading are shown in Fig 3.7(a,b). The (0001) pole figures calculated from the EBSD data for the regions shown in Fig 3.7(a,b) are presented in Fig 3.7(c,d) respectively

At the beginning of the deformation, the c-axes in most of the grains are oriented $\sim 90^0$ away from the ED. At a strain of 3.5%, due to the formation of numerous extension twins, c-axes in the twinned region of many grains have now been reoriented by $\sim 86^0$ with respect to the orientation of the parent grain. At a strain of approximately 9%, many of the grains have completely twinned and therefore now have their c-

axes oriented along the ED which is $\sim 90^0$ away from their original orientation. Previous studies in the literature on Mg alloys indicate similar behavior. Knezevic et al. [50] observed that extension twins completely consume grains reorienting them when a rolled AZ31 sheet is loaded in the orientation in which extension twinning is the preferred mechanism. Dudamell et al. [60] observed that in rolled AZ31 under dynamic loading, about 98% of the material is twinned at a strain of 10% when compressed in the sheet rolling direction. They also observed enhanced extension twinning activity at high rates of loading.

3.3.3 Evolution of dislocation substructure

The as-received material was examined by transmission electron microscopy (TEM) in order to understand the pre-existing dislocation structure in the material. The microstructure of the as-received material is shown in Fig 3.8. Fig 3.8a and 3.8b were taken in the same area but different diffraction spots were excited to reveal the $\langle a \rangle$ and $\langle c \rangle$ components of dislocations respectively. The $\mathbf{g} \cdot \mathbf{b} = \mathbf{0}$ invisibility criterion is used for this purpose. For the $\langle 0002 \rangle$ reflection, all the $\langle a \rangle$ type dislocations will lose their contrast and for the $\langle 2\bar{1}\bar{1}0 \rangle$ reflection, all the $\langle c \rangle$ type dislocations are extinguished. A $\langle c + a \rangle$ dislocation cannot be extinguished by either of the $\langle 0002 \rangle$ or $\langle 2\bar{1}\bar{1}0 \rangle$ reflections. A network of pure $\langle a \rangle$ dislocations with mainly edge component (referred to as background dislocations) is seen in Fig 3.8a. This network is most likely a result of the extrusion process. There are a few straight dislocations (highlighted by the white

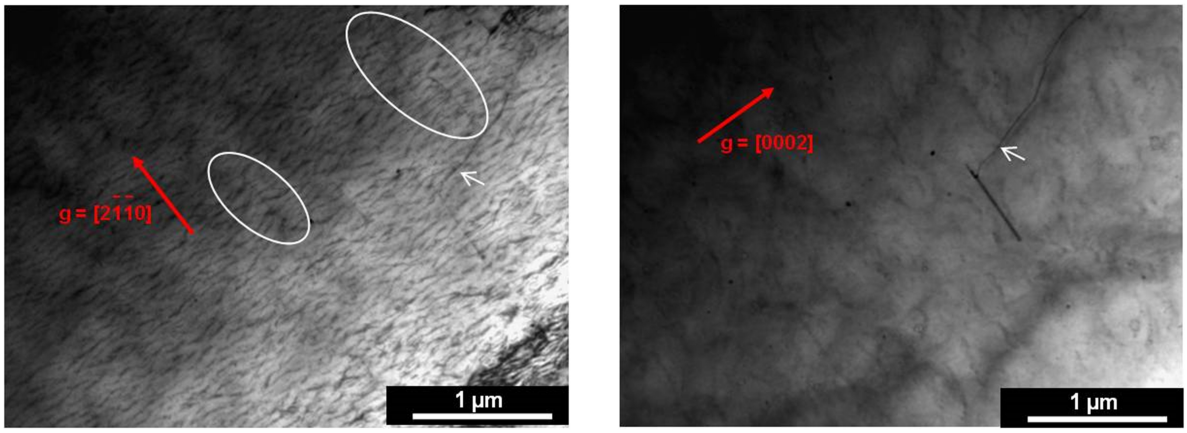

(a) (b)

Figure 3.8: Dislocations in the as-received material. The diffraction conditions were chosen to display (a) Dislocations with $\langle a \rangle$ component Burgers vector and (b) Dislocations with $\langle c \rangle$ component Burgers vector

ovals in the figure) that are parallel to a $\langle 2\bar{1}\bar{1}0 \rangle$ direction, which are likely to be $\langle a \rangle$ type screw dislocations. Fig 3.8b shows that there are very few $\langle c \rangle$ type dislocations. Dislocations of $\langle c + a \rangle$ type were also rarely seen in this microstructure. The one shown in the figure (marked by the white arrow) is essentially used as a marker for the two images and is a $\langle c + a \rangle$ type dislocation as it is not extinguished for either of the reflections.

The microstructure of the material dynamically deformed to a plastic strain of 3.5% (Fig 3.9) contains numerous twins. We examined the parent region (Fig 3.9a, 3.9b) as well as the twinned region (Fig 3.9c, 3.9d) in order to analyze the differences in dislocation activity between twins and parents. The dislocation microstructure in the

twinned region is vastly different than in the parent region. The background dislocations (the network of pure $\langle a \rangle$ dislocations with mainly edge component) still persist in the parent region as seen in Fig 3.9a. A number of long straight $\langle a \rangle$ dislocations are also observed (e.g. one is marked by the white oval) in Fig 3.9a but not in Fig 3.9b. The parent region remains mostly free of $\langle c + a \rangle$ dislocations.

In contrast to what was observed in the parent region, numerous straight $\langle c + a \rangle$ dislocations are present in the twinned region and are visible in Fig(3.9c, 3.9d). Since the twinned region is now oriented for compression along the c-axis, $\langle c+a \rangle$ pyramidal slip is a likely mechanism of plastic deformation. Many of these dislocations are parallel to the basal planes as seen in Fig 3.9c, 3.9d. Some curved $\langle c+a \rangle$ dislocations like the ones marked by the white arrows do not lie parallel to the basal planes. The twinned region also contains the background $\langle a \rangle$ dislocations. Although these dislocations look similar to the ones in the as-received material, they are caused by the deformation. The twinned regions will have a range of orientations with respect to the loading direction such that basal slip can be activated in many of them due to its low CRSS .

By about 9% strain (Fig 3.10), most grains have been consumed by twins and thus reoriented. Therefore, we only imaged the twinned region in these samples. The diffraction analysis showed that these dislocations contained both $\langle a \rangle$ and $\langle c \rangle$ components. Numerous long straight dislocations with some kinks are observed in both Fig 3.10a and Fig 3.10b. These images (Fig 3.10) indicate a change in the

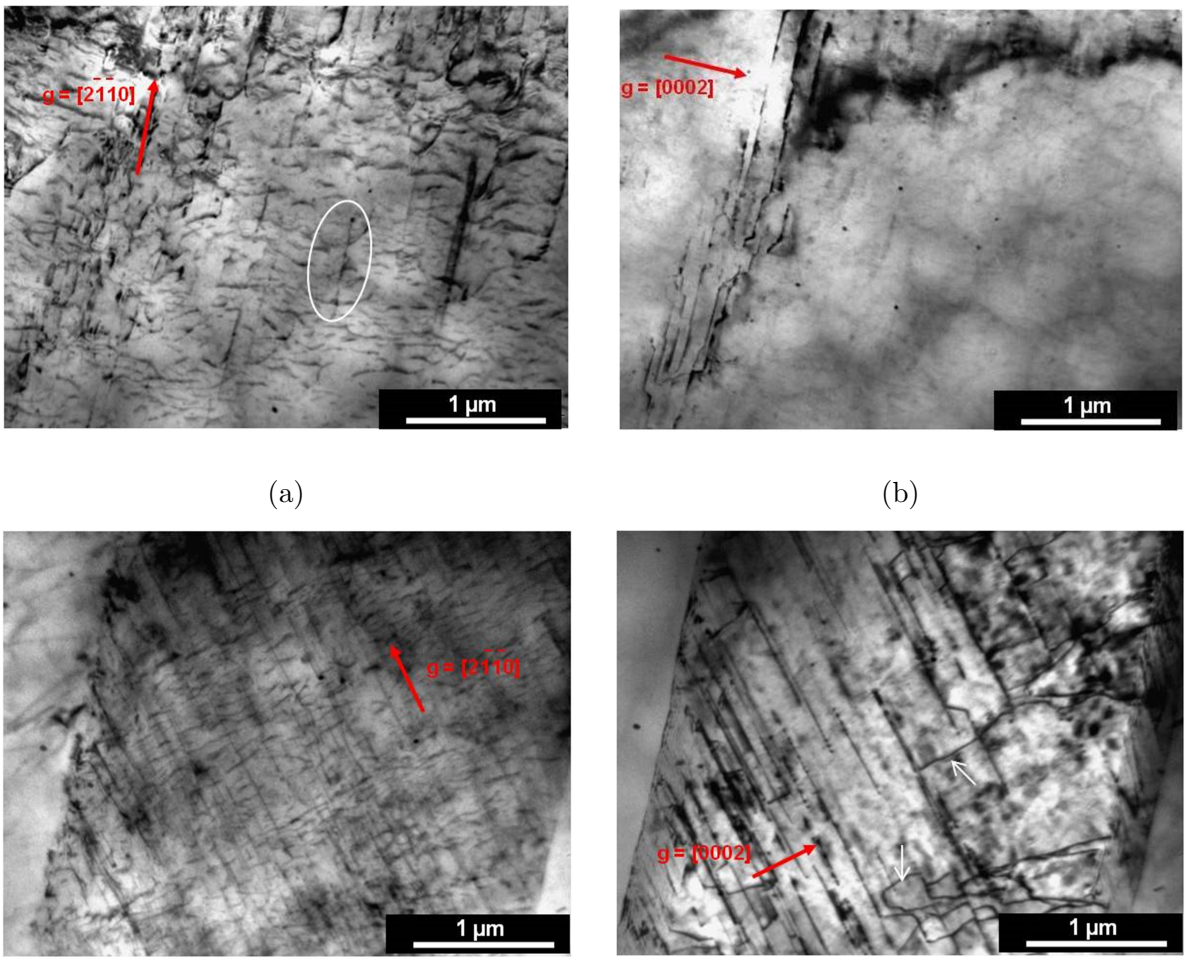

Figure 3.9: Dislocations in specimens deformed to strains of 3.5%. The diffraction conditions were chosen to display (a) $\langle a \rangle$ components in the parent region (b) $\langle c \rangle$ components in the parent region, (c) $\langle a \rangle$ components in the twinned region and (d) $\langle c \rangle$ components in the twinned region

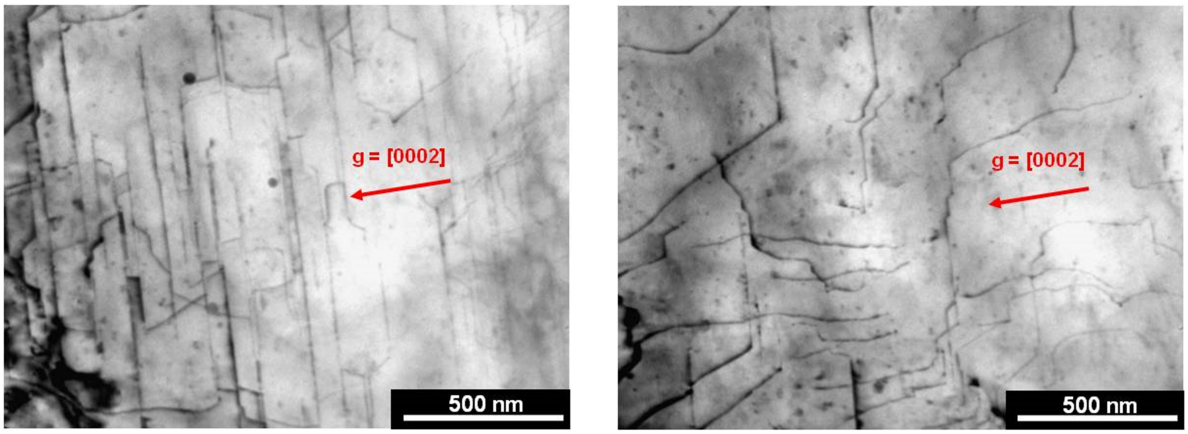

(a) (b)

Figure 3.10: Dislocations in the specimens deformed to strains of 9%. The dislocations are of $\langle c+a \rangle$ type

dislocation structure as compared to the dislocation structure at 3.5% strain in the twinned region. At 3.5% strain, most of the $\langle c+a \rangle$ dislocations were parallel to the basal planes (Fig 3.9c, 3.9d) whereas at 9% many of these dislocations had kinks (Fig 3.10a). Some of the $\langle c+a \rangle$ dislocations at 9% strain were curved and did not lie parallel to the basal planes (Fig 3.10b). These kinked dislocation segments were observed to be the dominant feature in the microstructure.

The dislocation densities in the deformed samples were also measured in the TEM images. The projected length (ℓ_p) of dislocation lines in the images were measured using the image analysis software ImageJ. The dislocation density was then calculated using the formula $\rho = \ell/(At)$ where $\ell = 4\ell_p/\pi$ [82]. The thickness of the foil, t, was assumed to be 100 nm. The $\langle a \rangle$ dislocations are in the form of a network making

the measurement of the dislocation density very difficult. Hence, we focused on the measurement of the density of $\langle c+a \rangle$ dislocations as this has been suggested to be the reason for the high degree of strain hardening [38]. The $\langle c+a \rangle$ dislocation density in the sample strained to 3.5% was measured to be $(3.0 \pm 0.11) \times 10^{13} m^{-2}$ (this is the average of the measurements in both the parent and twinned regions) and that measured in the sample deformed to 9% strain was $(1.0 \pm 0.04) \times 10^{14} m^{-2}$. It was difficult to measure the density of $\langle c+a \rangle$ dislocations in the as-received material since they were very few in number and their estimated dislocation density was several orders of magnitude smaller than the dislocation densities at 3.5% strain.

3.4 Discussion

3.4.1 Microstructural Evolution

In order to gain a better understanding of the changes in the texture of the material during deformation, the point-to-point misorientation angle distributions were measured at intermediate strains and are shown in Fig 3.11(a, b, c) for the as-received, 3.5% and 9% strain samples. Here, misorientation is defined as the rotation required to bring crystal orientations corresponding to two pixels into coincidence based on a fixed reference frame. The starting microstructure of this as-extruded material (Fig 3.11a) contains a misorientation angle distribution similar to the misorientation angle distribution of the as-rolled AZ31 material reported by Hong et al. [1]. At 3.5%

strain (Fig 3.11b), the misorientation distribution is dominated by a strong peak at $85^0 - 90^0$, which corresponds to the numerous extension twin boundaries present in the microstructure (the reorientation angle associated with extension twins in magnesium is $\sim 86^0$). Many grains at 3.5% strain contain two or more twins. Many of these twins are from the same variant pair which is discussed in detail later.

At 9% strain the twin growth and coalescence process is almost complete. This is evident from the reduction in the peak of $85^0 - 90^0$ observed in Fig 3.11b. The microstructure consists of many low angle boundaries ($<10^0$) as seen in Fig 3.11c. Additionally, a modest rise in the misorientation angle in the range of $50^0 - 60^0$ is also observed.

The coalescence of two twins may lead to different boundary misorientations depending upon the types of twin variants. There are six extension twin variants (or three twin variant pairs) in Mg. As pointed out in previous works, for extension twins in Mg, the misorientation relationship between identical twin variants is 0^0, between twins from the same variant pair is 7.4^0 and between twins from different variant pairs is 60^0 and 60.4^0 [1, 25]. Here, only the data above misorientation angles of 5^0 were considered since the confidence in the data below this value is low. The strong peak for the low misorientation angles ($<10^0$) indicates that in many cases, twins from the same variant pair were activated in a grain. Twins from different twin variant pairs were formed in some grains and are believed to be the origin of the $50^0 - 60^0$ misorientation.

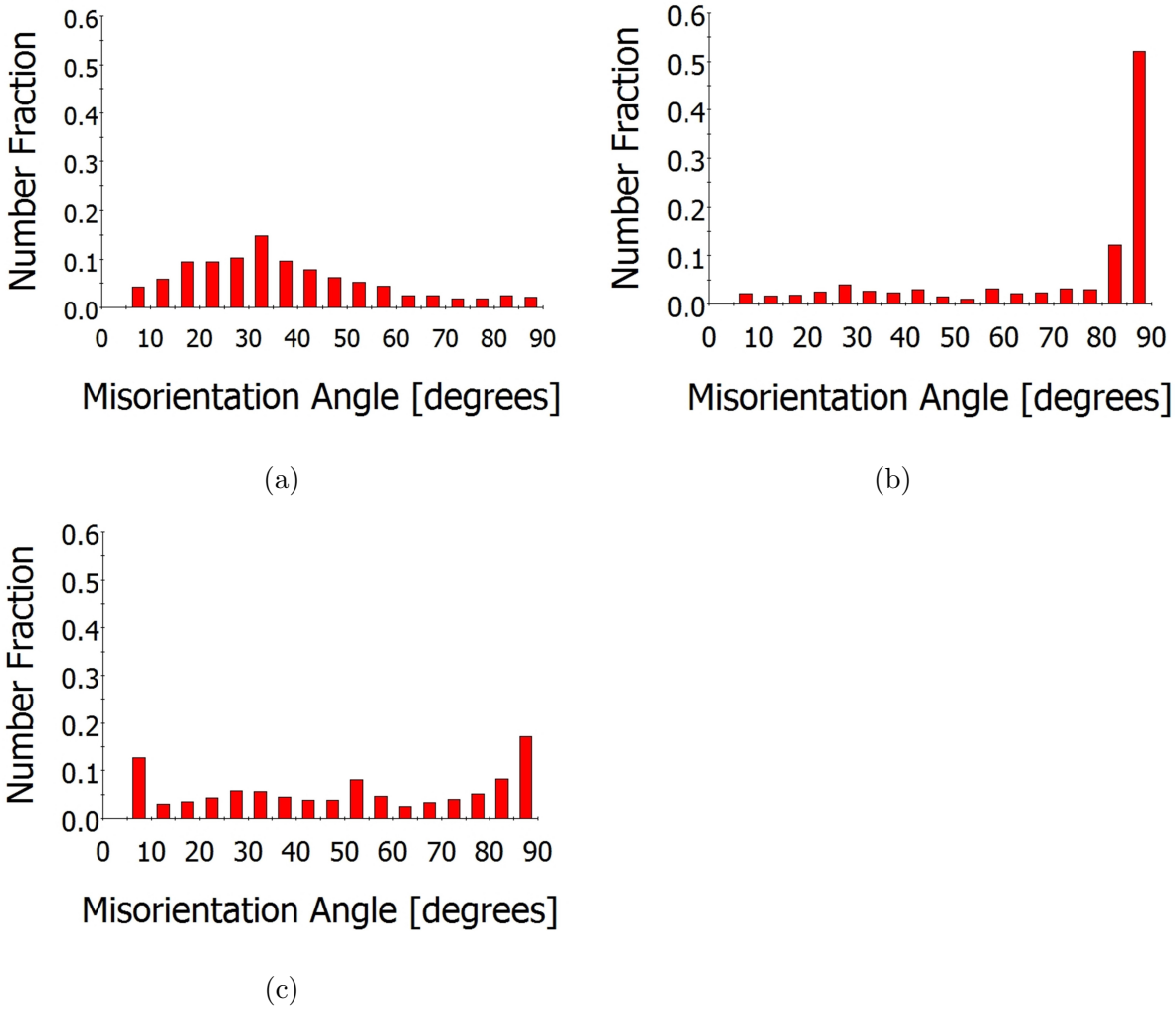

Figure 3.11: Point-to-point misorientation angle distributions calculated from EBSD in the ED of samples deformed at high strain rates upto the strain of (a) 0%, (b) 3.5% and (c) 9%

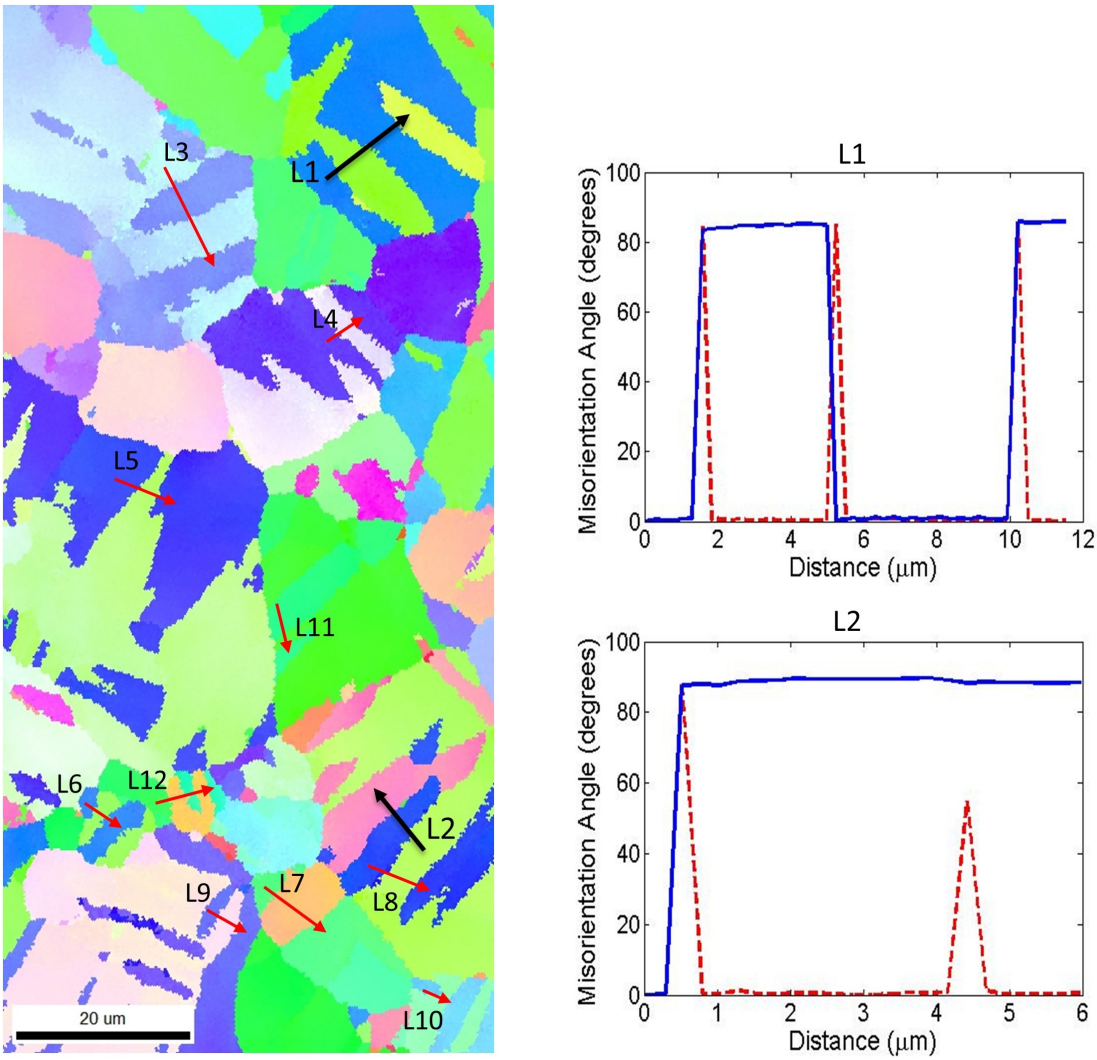

(a) (b)

Figure 3.12: (a) EBSD IPF of sample deformed upto 3.5% strain showing twin variants (b) Point-to-point misorientation (red dashed line) and point-to-origin misorientation (blue line) along line L1 and line L2. Lines L1 and L3-L11 represent twins from the same variant pair. Lines L2 and L12 represent twins from different variant pairs

CHAPTER 3. MICROSTRUCTURAL EVOLUTION OF PURE MAGNESIUM UNDER HIGH STRAIN RATE LOADING

The strain path dependence of extension twinning in AZ31 alloy was studied by Hong et al. [83]. Their observations indicate that for a rolled material with a strong basal texture, tension directly applied along the crystallographic c-axis, by applying tension along the sheet normal direction, leads to nucleation of different twin variants. When tension was imposed on the c-axis indirectly by applying compression in the sheet rolling direction (90^0 from c-axis), only one twin variant was nucleated. The selection of which twin variant is activated during deformation is believed to depend to some extent on the respective Schmid factors [49]. Beyerlein et al. [41, 42] suggested that the twin nucleation is heavily influenced by the grain boundary defects and the local stress state. Therefore, the orientation of each grain with respect to the loading axis along with the local stress state should dictate if one or more of these twin variants are activated during deformation. These twin variants have fixed misorientation relationships with each other and examination of the misorientation angle distributions can help us see which twin variants were active during deformation. The loading in this work is similar to the compression in the rolling direction in Hong's work (indirect tension imposed on the c-axes by applying compression in a perpendicular direction) and therefore we may expect that only one twin variant pair will be nucleated in most of the grains. Note that the texture of the material in this case is weaker (extrusion) than the strongly textured rolled material in Hong's work. This will have an effect on the types of twin variants that are nucleated depending on the grain orientation and the local stress state. The twin variant relationship at

3.5% strain is shown for a few grains in Fig 3.12. Fig 3.12b shows the point-to-point misorientation (red dashed line) and point-to-origin misorientation (solid blue line) along lines L1 and L2. The majority of grains contain twins from the same variant pair as in the case of the grain containing line L1. The twins corresponding to line L3 - L11 are all also from the same variant pair. A small number of grains contain different twin variants and the grain containing line L2 is shown here as an example. The misorientation angle for both the extension twins crossed by line L2 is about 86^0 with respect to the parent grain and about 60^0 between the twins suggesting that these extension twins are from different variant pairs. The twins corresponding to line L12 are also from a different twin variant pair. The misorientation angle between the different twin variants is observed to be close to $\sim 60^0$ which is expected from the theoretical misorientation relationship.

Several low angle boundaries were identified in the TEM analysis of the sample deformed to 9% strain (Fig 3.13a). These were not apparent at the early stage (3.5%) of deformation. These low angle boundaries (highlighted with red dashed lines) are found within the same grain. The misorientation angle associated with these boundaries is a few degrees ($<2^0$). The structure of one of these low angle boundaries is in the form of a dislocation cell as shown in Fig 3.13b. The dislocation-dislocation interaction and recovery processes most likely lead to the formation of the dislocation cells and subgrains (Fig 3.13).

The observations in this study can be compared to the ones reported in the liter-

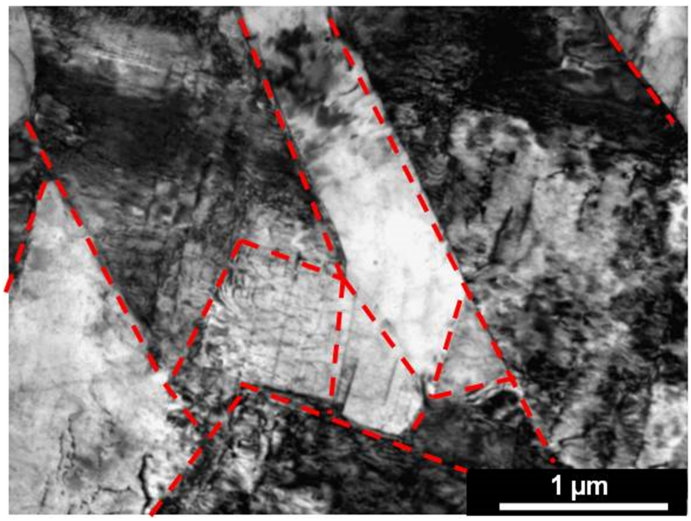

(a)

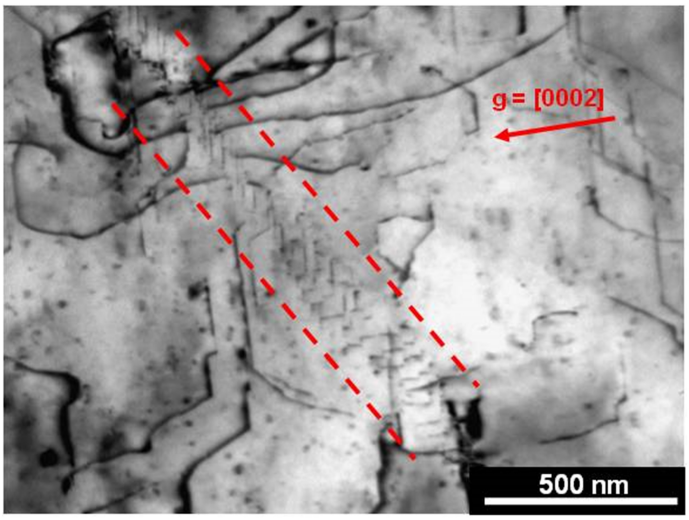

(b)

Figure 3.13: Specimen deformed upto a strain of 9% (a) Formation of subgrains with low angle boundaries seen within a grain (b) The structure of one of these boundaries in the form of a dislocation cell

ature. Dislocation activity during compression of Mg single crystals along the c-axis was studied by Obara et al. [38]. A high activity of $\{11\bar{2}2\}\langle\bar{1}\bar{1}23\rangle$ slip system was found in their study. The $\langle c+a\rangle$ dislocations observed in their study were found to lie parallel to the basal planes as well. Morozumi et al. [84] studied the dislocation activity in and around $\{1\bar{1}02\}$ twins in pure magnesium. They observed $\langle c+a\rangle$ dislocation activity inside the twins as well. The activity of $\langle c+a\rangle$ dislocations has been associated with extension twins by a few other researchers previously [17, 84].

Mechanisms for dissociation of $\langle c+a\rangle$ dislocations have been proposed in a few studies [17]. Some of these proposed mechanisms suggest dissociation of $\langle c+a\rangle$ dislocations into $\langle a\rangle$ and $\langle c\rangle$ dislocations. Pure $\langle c\rangle$ dislocations were generally not observed in our investigation. This is similar to the observation of Obara [38].

3.4.2 Strain hardening rates

Given the texture of the material, when a compressive load is applied in the ED it is expected that most grains will experience extension along the c-axis under uniaxial stress conditions. Extension twinning is highly favored under this loading configuration. The true stress vs. true strain curve exhibits a sigmoidal shape which is known to be a characteristic of extension twinning [21, 50, 59]. The shape of the stress strain curve compares well with other works on Mg and Mg alloys of similar grain size under loading configurations where extension twinning is the favored mechanism [1, 50, 85]. The studies at high strain rates on AZ31B have also shown similar results

[59, 60]. The effective strain hardening rates (Fig 3.3b) are high and increase with strain similar to other works on Mg alloys [1, 50]. The extension twins were observed to develop at early stages of deformation (<3.5%) strain. They do not require high stresses for growth and are known to grow very quickly and consume entire grains. Thus, the extension twins are not a likely source of the high strain hardening rates as also pointed out by Knezevic et al. [50]. Once a twin is formed, the twinned region is reoriented by 86^0 and is now in a hard orientation in most cases. This serves as a contribution to the strain hardening rate in the form of texture hardening.

The twinned region which is under c-axis compression can undergo deformation by $\langle c + a \rangle$ slip. As the deformation progresses, the dislocation density inside the twinned region increases. In addition, the volume of the material undergoing $\langle c + a \rangle$ slip increases as strain is accumulated. As the accumulated strain increases, the interaction of the $\langle c + a \rangle$ dislocations increases.

The highest strain hardening rates are observed when the texture of the material is such that most grains are favorably oriented for c-axis compression [1, 38, 50]. In this work, by about 9% strain, most of the grains have completely twinned so that the crystallographic c-axis in these grains will be under compression during further loading. In this configuration, contraction twinning and $\langle c + a \rangle$ slip are the mechanisms that can accommodate the plastic strain. Some authors have suggested that contraction twins are responsible for the high strain hardening rates in AZ31 [50]. In the present work, no contraction twins were observed upto the strain level corresponding

to the maximum strain hardening rate. Thus, we believe the very high strain hardening rates are a result of the $\langle c+a \rangle$ dislocation activity as suggested by the formation of subgrains and dislocation cells by dislocation-dislocation interactions.

The density of $\langle c+a \rangle$ dislocations increases significantly as the deformation progresses $(3.0 \pm 0.11) \times 10^{13} m^{-2}$ at 3.5% strain and $(1.0 \pm 0.04) \times 10^{14} m^{-2}$ at 9% strain). At lower strains, these dislocations are mainly parallel to the basal planes. As strain is accumulated, the dislocation interaction increases as suggested by the higher number of dislocations that have kinked segments (Fig 3.10b). At strains of about 9%, the mobile dislocations also face obstacles from the dislocation cells as shown in Fig 3.13. Therefore, the texture hardening and dislocation activity appear to work together and contribute to the high strain hardening observed in this work.

3.5 Summary

The mechanical behavior of extruded magnesium under compression in the ED has been studied at quasi-static and high strain rates. The deformation mechanisms and microstructural evolution under dynamic loading have also been investigated. The key observations are:

- Extension twinning and dislocation activity are both required to accommodate plastic strains under high strain rate loading.

- In the early stages of deformation (3.5% strain), numerous extension twins are

formed. Deformation by $\langle c+a \rangle$ dislocation slip occurs in the twinned region to accommodate compressive load along c-axis. These extension twins contain $\langle c+a \rangle$ dislocations that lie parallel to the basal planes.

- The parent region (at 3.5% strain) contains long straight $\langle a \rangle$ dislocations despite the low Schmid factor for the associated slip systems. This is attributed to the ease of basal slip in Mg due to its low CRSS.

- As the deformation progresses, the extension twins consume entire grains thus reorienting them into a hard orientation. $\langle c+a \rangle$ slip is therefore a favored mechanism for accommodating compression along the c axis. A significant increase in the density of $\langle c+a \rangle$ dislocations with increase in strain is observed. This increase in dislocation density and the dislocation-dislocation interactions at higher strains ties directly with the high strain hardening rates observed in this work.

- No contraction twins were observed in this work upto strains of 9%. Therefore, the high strain hardening rates observed in this work are associated with dislocation activity and texture hardening.

- Dislocation cells and subgrains formed due to the dislocation-dislocation interactions are believed to be the source of the high strain hardening rates.

Similar analysis of microstructural evolution can be performed under quasi-static loading. A comparison of the current work with such an analysis will enable us

to gain insight into the strain rate dependence of different deformation mechanisms. Based on the understanding of the evolution of the dominant deformation mechanisms in magnesium, the development of a simple mechanism based constitutive model is discussed in Chapter 4.

Chapter 4

Constitutive Modeling

4.1 Introduction

The mechanical behavior of magnesium and its alloys is governed by multiple deformation modes such as basal and non-basal slip and extension and contraction twinning as discussed in Chapter 3. Which of these modes are dominant is dependent upon the loading conditions such as the nature of loading with respect to the texture of the material, temperature, rate of loading etc. Under some loading conditions, multiple modes of deformation are activated (Chapter 3). In order to predict the material behavior under different loading conditions, constitutive models need to account for the various deformation mechanisms, their interaction and evolution.

There has been significant work done in the recent years on modeling the deformation of magnesium and its alloys using a variety of modeling techniques. Phenomeno-

logical models have been used in the past to describe the rate dependent deformation behavior of metals [86]. Many of these models are essentially empirical fits to data and perform very well over a limited range of strain, strain rate and temperature values. In these models, the flow stress is typically described as a function containing the strain, strain rate and temperature. Models such as Johnson-Cook [86] have a small number of parameters and are computationally efficient and have been successfully used to describe the behavior of some FCC metals. A modified form of the Johnson-Cook model was used by Ulacia et al. to describe the behavior of rolled AZ31B, a magnesium alloy [87]. They considered a range of strain rates and temperatures but only considered the orientations that undergo slip and ignored twinning. However, it is important to capture the orientation dependence of deformation modes and the associated texture evolution in the case of HCP metals like magnesium that undergo twinning in addition to slip. It is difficult for phenomenological models to account for the observed sigmoidal stress-strain response under twinning dominated deformation in magnesium. A semi-analytical formulation was developed by Barnett et al. which captures the twinning dominated deformation of magnesium in the low strain rate regime well [88]. The texture evolution in this case is captured by an empirical twin volume fraction evolution relationship.

Physics/mechanism based constitutive models are another class of models that are used to describe behavior of metals. These models typically incorporate an internal state variable approach. The evolution of the internal state variable is described in

the model and the constitutive behavior is directly described by the current value of the internal state variable. The internal state variables (eg. dislocation density, twin volume fraction) generally represent the microstructure of the material and its evolution with deformation. Examples of such models include the MTS and Zerilli-Armstrong models, which use a thermal activation theory of dislocation motion [89, 90]. The formulation developed by Estrin [91] extended the Kocks-Mecking model to incorporate effects of particles and solutes on the evolution of the internal state variable.

The behavior of magnesium is complicated due to the anisotropy, slip and twinning mechanisms and their interaction. Constitutive models need to account for the initial texture, the wide range of strengths of different slip and twin systems and the evolution of texture due to twinning to successfully describe the behavior of this material. However, conventional physics based models do not capture these phenomena well and need to be extended to successfully model the deformation of magnesium.

Several single crystal plasticity models have also been developed in the last decade. The first few models that incorporated the slip and twinning deformation modes in HCP materials in a single crystal plasticity framework were developed by Kalidindi, Staroselsky and Anand [92–94]. More recently, the single crystal plasticity model developed by Zhang and Joshi [2] incorporated the evolution characteristics of extension and contraction twins. A number of self-consistent polycrystal plasticity models have been developed that incorporate dislocation slip and deformation twinning [48, 95].

These models are typically used to study the macroscopic response of polycrystalline materials such as strain hardening and texture evolution and have been fairly successful in describing the behavior of magnesium at low strain rates.

There is a need for more sophisticated physics based models which can account for complex deformation processes in magnesium and its alloys under a variety of loading conditions. Due to the advances in both the experimental as well as computational capabilities, we are now able to obtain information about defects such as dislocations, twins etc. at small length scales. The EBSD and TEM data enables us to build a fundamental understanding of the defect structures inside the material. Computational techniques such as molecular dynamics (MD) can be used to study the interaction of these defects. Leveraging such information from multiple scales can help us build better constitutive models that are able to capture complex deformation characteristics of materials like magnesium. There have been a few efforts in the recent years trying to incorporate this information in models (eg. Beyerlein et al. [42]).

A simple physics based scalar constitutive model which takes into account the evolution of the dominant mechanisms active during the deformation of magnesium is developed here. The model is applied to the deformation of single crystal and extruded polycrystalline magnesium. The model is developed in Section 4.2 and the evolution equations for the internal state variables are presented in Sections 4.2.1, 4.2.2.1, and 4.2.2.2.

4.2 Modeling framework

The scalar constitutive model described here is based on an internal state variable approach. The internal state variables considered here are the dislocation densities of the $\langle a \rangle$ and $\langle c+a \rangle$ dislocations (ρ_a, ρ_{c+a}) and the extension twin volume fraction f. These internal state variables evolve as the deformation progresses, and the evolution equations for these internal state variables are described in this section.

The flow stress of the material is given by

$$\sigma = \sigma_0 + \sigma_{Taylor} \tag{4.1}$$

where σ_0 is the initial deformation resistance which includes the lattice resistance (Peierl's stress) and the grain size dependent strength from the Hall-Petch effect in the case of polycrystalline materials.

$$\sigma_0 = \sigma_P + \sigma_{HP} = kd^{-1/2} \tag{4.2}$$

σ_P is the Peierl's stress and σ_{HP} is the Hall-Petch term where d is the grain size and k is the Hall-Petch constant. The term σ_0 remains constant and does not evolve with deformation.

The second term in Eq 4.1 accounts for the strength from the density of dislocations in the material given by the Taylor hardening equation

$$\sigma_{Taylor} = \alpha M \mu b \sqrt{\rho_{total}} \tag{4.3}$$

Here, α is the dislocation-dislocation interaction parameter, M is the texture dependent Taylor factor for polycrystalline material, μ is the shear modulus, b is the Burgers vector and ρ_{total} is the total dislocation density.

The total dislocation density is decomposed into the additive sum of the $\langle a \rangle$ and $\langle c+a \rangle$ dislocation densities since these are the commonly observed dislocation types in magnesium.

$$\rho_{total} = \rho_a + \rho_{c+a} \tag{4.4}$$

Based on experimental observations, pure $\langle c \rangle$ dislocations are very rarely observed and therefore are not considered in the model. The equations for the evolution of the $\langle a \rangle$ and $\langle c+a \rangle$ dislocation densities are formulated separately. The CRSS for these two slip systems and the loading configurations under which these dislocations are activated are significantly different from each other. Since extension twinning is a dominant deformation mechanism in magnesium and due to the propensity of the extension twins to grow, we consider two material domains in our analysis - the parent region and the twinned region. Different types of dislocation slip may be activated in the parent and twin regions depending on the loading conditions (Chapter 3). The growth of the extension twins is modeled through an empirically derived relationship based on the work by Barnett et al. [88].

In order to develop a formulation that can be applicable to general deformations under which a variety of deformation modes are active, we consider the cases of compression along the $\langle a \rangle$ axis for single crystal Mg and compression in the extrusion

direction for extruded polycrystalline Mg. Under these loading conditions, multiple modes of deformation, namely, extension twinning, $\langle a \rangle$ slip and $\langle c+a \rangle$ slip are activated at various stages of deformation. We describe the evolution equations for these three deformation modes in the following sections.

4.2.1 Evolution of twin volume fraction

Extension twins in magnesium are easily nucleated and can grow to consume large volumes causing a significant change in the texture of the material [21]. Therefore, evolution of the volume fraction occupied by extension twins is considered here. Contraction twins are not as commonly observed in magnesium. They are difficult to nucleate and grow, and typically occupy small volumes [22]. Therefore, the evolution of contraction twins is not considered here as they are unlikely to cause significant changes to the texture.

An empirical relationship for the evolution of the extension twin volume fraction with strain based on Barnett's [88] work is used here. The twin volume fraction is described as the ratio of the volume of the twinned material to the total volume ($f=\frac{V_{twin}}{V}$). The twin volume fraction evolution equation used by Barnett et al. is

$$f(\epsilon) = 1 - exp[-4(\frac{\epsilon}{\epsilon_{max}})^a] \tag{4.5}$$

where f is the twin volume fraction and ϵ is the equivalent plastic strain. ϵ_{max} is the value of strain at which twinning is 98% complete, and a is a parameter. We use

a slightly modified version of the above equation for simplicity (Eq 4.6).

$$f(\epsilon) = 1 - exp[-(\frac{\epsilon}{\kappa})^a] \tag{4.6}$$

This modified equation has two parameters κ and the strain rate exponent a. The value of a is kept constant and equal to 2.5, which is the same as that in Barnett's work for extension twinning dominated deformation. The effect of the value of κ on the twin volume fraction evolution from Eq. 4.6 is shown in Fig 4.1 and Fig 4.2 below.

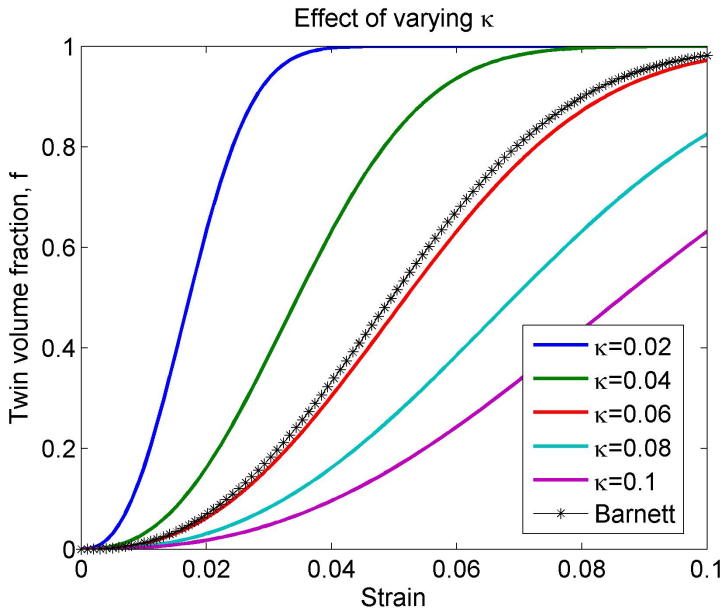

Figure 4.1: Twin volume fraction evolution with strain; the effect of varying the parameter κ in Eq 4.6

Here, the twin volume fraction is taken to be 0 when there are no twinned regions in the material and is taken to be 1 when the entire material has been reoriented by

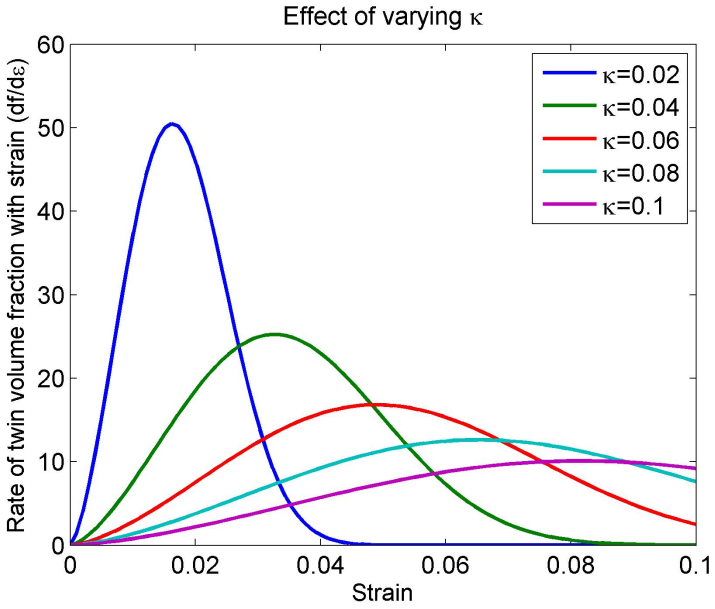

Figure 4.2: Rate of change of twin volume fraction with strain; the effect of varying the parameter κ in Eq 4.6

twinning. For comparison, Barnett's twin volume fraction evolution function is also plotted in Fig 4.1. The parameter values used for Barnett's function were $\epsilon_{max} = 0.1$ and a = 2.5. It can be observed from Fig 4.1 that the twin volume fraction reaches its peak rapidly and then saturates for smaller values of κ. The peak/saturation value of the twin volume fraction, f, decreases with increase in κ for the same strain. Different evolution rates for the twin volume fraction can be obtained by varying the values of κ. The rate of change of the twin volume fraction with strain $(\frac{df}{d\epsilon})$ varies with the value of κ as well (Fig 4.2). The highest value of $\frac{df}{d\epsilon}$ is observed for smallest values of κ. The strain at which this peak value of the rate of change of twin volume fraction $(\frac{df}{d\epsilon})$ occurs is lower for smaller values of κ. Therefore, the material twins

rapidly initially and twinning saturates at a lower strain for smaller values of κ. The phenomenological relationship presented here is used to describe the observed twin volume fraction evolution in magnesium in this work.

4.2.2 Evolution of dislocation density

In order to accommodate the plastic deformation, dislocation motion occurs under the applied load. In order to continue their motion, dislocations need to overcome the energy barriers created by short range obstacles (such as other dislocations, solutes, precipitates etc.) and long range obstacles (such as grain boundaries). The distance that a dislocation can travel depends on the structure and spacing of these obstacles. Gliding dislocations can be immobilized by these obstacles and be stored causing the dislocation density to increase. As the deformation progresses, under the applied load, some of these dislocations may cross slip and interact with other dislocations causing dislocation annihilation or kinks and jogs. These mechanisms are accounted for by the evolution equations.

The dislocation density evolution is dictated by the competition between dislocation accumulation and recovery. When gliding dislocations become immobilized and are stored, there is an increase in the dislocation density. Follansbee et al. suggested that this immobilization distance is inversely proportional to the imposed strain rate [90]. Therefore, the dislocation accumulation term is considered to be dependent on the strain rate and temperature. Experimental observations of increased

dislocation densities at high rates and dislocation generation under shock loading in some FCC metals support this idea [96]. Therefore, the coefficient of the dislocation accumulation term, in the case of both $\langle a \rangle$ and $\langle c + a \rangle$ dislocations is considered to be strain rate and temperature dependent. The recovery of dislocations can occur through cross slip which is also a strain rate and temperature dependent mechanism.

4.2.2.1 $\langle a \rangle$ dislocations

In magnesium, both single crystal and polycrystalline, $\langle a \rangle$ slip is activated under many loading conditions due to its low CRSS. Activity of $\langle a \rangle$ slip is observed even under loading conditions where this deformation mode is not geometrically favored. Under compression in the extrusion direction in the case of extruded polycrystalline magnesium, profuse extension twinning is observed along with $\langle a \rangle$ slip in the parent region. The density of the $\langle a \rangle$ dislocations evolves inside the parent region with strain.

The equations below describe the evolution of this dislocation density. The dislocation density evolution equation (Eq 4.8) has two terms - one accounts for the increase in the dislocation density due to dislocation generation, dislocation-dislocation interaction etc. and the other term accounts for the decrease in dislocation density due to dislocation annihilation or recovery.

$$\dot{\rho}_a = \frac{\delta \rho_a}{\delta \epsilon} \dot{\epsilon} \tag{4.7}$$

where

$$\frac{\delta\rho_a}{\delta\epsilon} = (\frac{\beta}{b_a}\sqrt{\rho_a} - \beta_r\rho_a)[1-f]^n \tag{4.8}$$

and $\dot{\epsilon}$ is the equivalent plastic strain rate, $\beta(\dot{\epsilon}, T)$ is the dislocation accumulation or the source parameter and $\beta_r(\dot{\epsilon}, T)$ is the dislocation annihilation or the recovery parameter. The mean free path (λ) that a dislocation can travel before being stopped depends on the average dislocation spacing (eq 4.9) [97] assuming that other dislocations are the primary obstacles. The obstacles are assumed to be dislocations of the same type for the first order interactions.

$$\frac{\delta\rho_a}{\delta\epsilon} = \frac{P}{b}\frac{1}{\lambda_a} \tag{4.9}$$

where P is a constant. The dislocation spacing can be expressed in terms of the dislocation density which gives us $\lambda_a \propto \frac{1}{\sqrt{\rho_a}}$ for $\langle a \rangle$ dislocations. This results in the form of the first term in eq 4.8.

Experimental observations suggest that the $\langle a \rangle$ dislocation slip occurs inside the original/parent crystal (Chapter 3). The volume fraction of the parent region is given by (1 - f), where f is the volume fraction of the twinned region (Section 4.2.1). Therefore, the evolution equation for the density of $\langle a \rangle$ dislocations contains this term. If there is no twinning in the material, $f = 0$, and there is no effect of this term on the dislocation density. If twinning occurs and the value of f increases, the volume fraction of the parent region decreases and the rate of change of the $\langle a \rangle$ dislocation density decreases. When the material is completely twinned, $f = 1$, and the volume fraction of the parent region is 0, the rate of change of $\langle a \rangle$ dislocation density with

strain (Eq 4.8) becomes zero and the dislocation density saturates and doesn't change with further strain. Therefore, the volume fraction term dominates the evolution rate of $\langle a \rangle$ dislocations at later stages of twinning. Note that the $\langle a \rangle$ dislocations inside twins are not considered in this analysis for simplicity. The values of the various parameters from Eq 4.8 are determined later, in Sections 4.3 and 4.4.

4.2.2.2 $\langle c + a \rangle$ dislocations

Extension twinning in magnesium causes an $\sim 86^0$ reorientation of the crystal compared to the parent region. Therefore, continued compressive loading along the $\langle a \rangle$ axis in single crystal Mg or along ED in extruded Mg, imposes compression along the $\langle c \rangle$ axis of the twinned (reoriented) region. Under this loading configuration, pyramidal $\langle c + a \rangle$ slip and contraction twinning are the favorable modes of deformation. In this work, we focus solely on the easier $\langle c + a \rangle$ slip mechanism. In the case of deformation involving extension twinning, the $\langle c + a \rangle$ slip is activated inside the twinned region. Therefore, the volume fraction of the twinned region, f, is considered in the evolution equation. When there are no twins, $f = 0$, and there is no increase in the density of $\langle c + a \rangle$ dislocations. As twins grow, f increases and more $\langle c + a \rangle$ dislocations can be accumulated inside the twinned region. The contribution from the growth of twins saturates when f grows to 1.

$$\dot{\rho}_{c+a} = \frac{\delta \rho_{c+a}}{\delta \epsilon} \dot{\epsilon} \tag{4.10}$$

$$\frac{\delta\rho_{c+a}}{\delta\epsilon} = (\frac{\gamma}{b_{c+a}}\sqrt{\rho_{c+a}} - \gamma_r\rho_{c+a})[f]^n \tag{4.11}$$

where $\gamma(\dot{\epsilon}, T)$ is the coefficient of the dislocation accumulation/source term and $\gamma_r(\dot{\epsilon}, T)$ is the coefficient of the dislocation annihilation or recovery term for the $\langle c+a\rangle$ dislocations. The volume fraction of the twinned material, f, affects the rate of change of the $\langle c+a\rangle$dislocation density increasing it as the volume fraction increases.

The volume fraction terms of f in the case of $\langle c+a\rangle$ slip and (1 - f) in the case of $\langle a\rangle$ slip are also representative of the orientation dependence of the mechanisms. The value of f=0 corresponds to the loading configuration such that the c-axis is under extension and there is no $\langle c+a\rangle$ slip. The value of f=1 corresponds to the loading configuration in the case of the c-axis under compression. This later is also applicable when the activity of $\langle c+a\rangle$ slip is observed with no extension twinning. Therefore, in the case of c-axis compression of Mg single crystal, f is set to 1 since $\langle c+a\rangle$ slip is the dominant mechanism of deformation and extension twinning is generally not observed.

The set of equations presented in this section give the general framework for the constitutive model. This model is applied to the case of deformation of single crystal Mg along crystallographic $\langle a\rangle$ axis and $\langle c\rangle$ axis and compression of extruded magnesium along the extrusion direction (ED) in the following sections.

4.3 Deformation of Single Crystal Mg

Analysis of the deformation of single crystal magnesium enables us to build a fundamental understanding of the orientation dependent deformation modes of this material. The insights gained from this study can be extended for application to polycrystalline deformation. Studies on single crystals of magnesium and alloys over the last few decades at both the micro and macro scale have enhanced our understanding of the deformation mechanisms in this material. Studies on the micro-compression of single crystal magnesium along different orientations have been performed which bring out the dominance and size dependence of the deformation mechanisms [98,99]. The properties of bulk single crystals were investigated by Kelley and Hosford [37] in the 1960s under plane strain compression along different orientations. More recently, quasi-static uniaxial compression experiments were performed on bulk single crystals of 99.99% purity by Xie et al. at Johns Hopkins University (in preparation) and Syed et al. [100]. Post-deformation microstructural investigation of the specimens revealed the dominant deformation modes. With the insights gained from the experimental work, we employ the simple mechanism based modeling framework developed in Section 4.2 to describe the behavior of bulk single crystals of Mg.

4.3.1 Analytical solution for $\langle c \rangle$ axis compression of single crystal Mg

Compression of single crystal magnesium along the c-axis is considered first since only one dominant mode of deformation is activated under this loading. Pyramidal $\langle c+a \rangle$ slip is the primary mode of deformation under this loading which has been observed in bulk crystals as well as some micrometer size specimens [38, 98, 100]. We develop an analytical solution for this loading condition which describes the evolution of the density of the $\langle c+a \rangle$ dislocations with deformation. The twin volume fraction evolution is not considered here since twinning is not observed under this loading configuration. The orientation of the material with respect to the loading is such as that represented by setting the value of $f = 1$ in Eq 4.11.

The evolution of the dislocation density ρ can be expressed as

$$\frac{d\rho}{dt} = (\frac{\gamma}{b}\sqrt{\rho} - \gamma_r \rho)\frac{d\epsilon}{dt} \tag{4.12}$$

from Eq 4.11.

Let $A = \gamma/b$ and $B = \gamma_r$. Therefore,

$$d\rho = (A\sqrt{\rho} - B\rho)d\epsilon \tag{4.13}$$

Integrating the above equation in order to obtain an analytical relationship between ϵ and ρ we obtain

$$\epsilon = \frac{-2}{B}\log(B\sqrt{\rho} - A) + C \tag{4.14}$$

where C is the constant of integration. At $\epsilon = 0$, $\rho = \rho_i$, the initial dislocation density. Therefore, the constant of integration is

$$C = \frac{2}{B}\log(B\sqrt{\rho_i} - A) \tag{4.15}$$

Hence, we obtain the relationship between ϵ and ρ as

$$\epsilon = \frac{2}{B}\log(\frac{\sqrt{\rho_i} - \frac{A}{B}}{\sqrt{\rho} - \frac{A}{B}}) \tag{4.16}$$

Inverting the above equation gives us

$$\sqrt{\rho} = \frac{A}{B} + (\sqrt{\rho_i} - \frac{A}{B})\exp(-\frac{B\epsilon}{2}) \tag{4.17}$$

where A has the units of m^{-1} and B is dimensionless. Then, substituting in the Taylor hardening equation (4.1), we obtain the analytical expression for the c-axis single crystal compression.

$$\sigma = \sigma_0 + \alpha\mu b[\frac{A}{B} + (\sqrt{\rho_i} - \frac{A}{B})\exp(-\frac{B\epsilon}{2})] \tag{4.18}$$

Re-substituting the values for A and B, we obtain,

$$\sigma = \sigma_0 + \alpha\mu b[\frac{\gamma}{\gamma_r b} + (\sqrt{\rho_i} - \frac{\gamma}{\gamma_r b})\exp(-\frac{\gamma_r\epsilon}{2})] \tag{4.19}$$

The data from the recent experiments conducted on single crystal Mg by Xie et al. (in preparation) (Fig 4.4) were used to select the values of the parameters so as

to fit the experimentally measured stress-strain response. Table 4.1 lists the values of the parameters used here.

σ_0	40 MPa
b, Burgers vector for $\langle c+a \rangle$ dislocations	0.61×10^{-9} m
α for pyramidal-pyramidal interaction	0.9
μ, shear modulus	17.2 GPa
γ	3.3
γ_{rec}	150
Initial dislocation density, $\rho_{(i)}$	$8.7 \times 10^{11} m^{-2}$

Table 4.1: Parameters for $\langle c \rangle$ axis compression of single crystal Mg

The values of the Burgers vector and the initial strength σ_0 are taken from the literature [2, 101]. The Taylor hardening equation is then used to calculate the value of the initial dislocation density. The experimentally measured value flow stress of the material at yield is ∼61 MPa. The value of the initial dislocation density is calculated to be $0.87 \times 10^{12} m^{-2}$. The value of the dislocation-dislocation interaction parameter α is taken to be 0.9 for the pyramidal-pyramidal interaction from the literature [102].

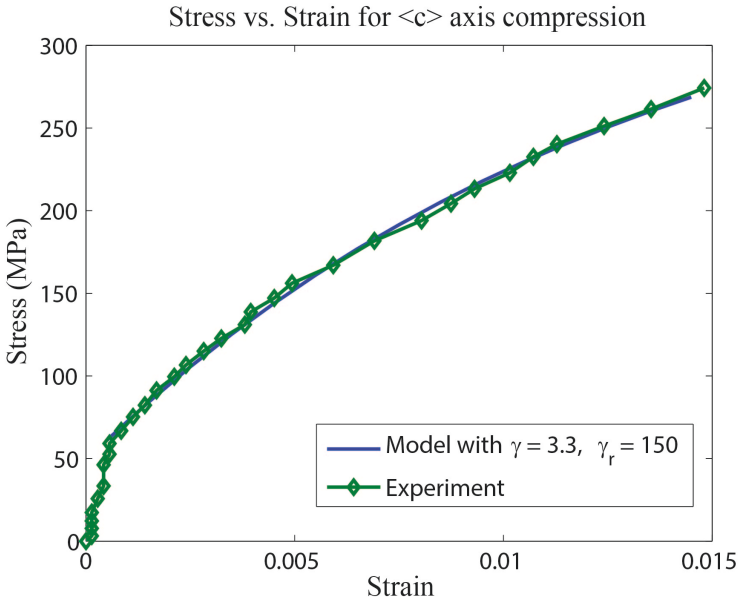

Figure 4.3: Comparison of the experimental (green line) stress vs. strain response of single crystal Mg with the output of the model (blue line) under c-axis compression

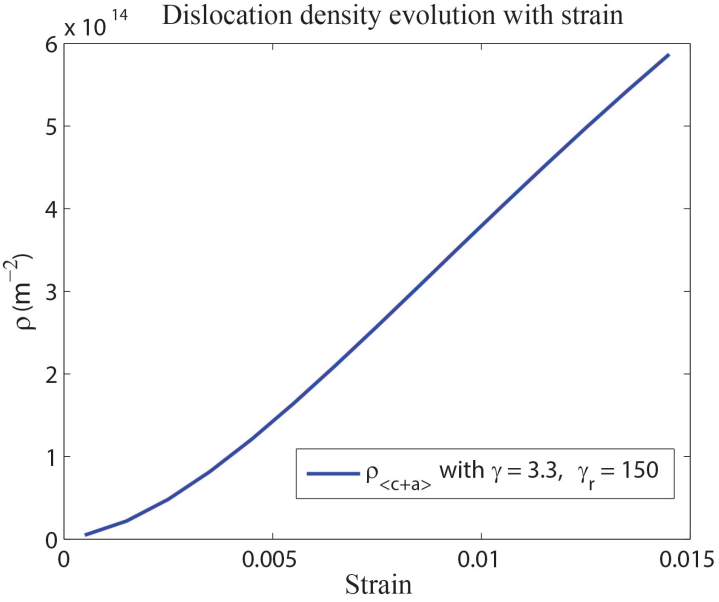

Figure 4.4: Evolution of the density of $\langle c+a \rangle$ disloctions under c-axis compression

The stress-strain response of the material generated using the analytical solution for $\langle c \rangle$ axis compression of magnesium is presented in fig 4.3. The comparison between the experimental response (green line) and the model output (blue line) and the evolution of the dislocation density from the model shows that the analytical formulation can capture the material response well. Under this loading, the final strains achieved are low (of the order of $\sim 2-4\%$). The dislocation density rises significantly so as to produce the high degree of strain hardening observed. The accumulated dislocation density from the model falls in the range of the experimentally measured dislocation density values reported in the literature [103].

4.3.2 Response of single crystal Mg under compression along the $\langle a \rangle$ axis

The deformation of bulk single crystal Mg loaded in compression along the $\langle a \rangle$ axis was recently studied experimentally by Xie et al. (in preparation). This loading configuration imposes indirect tension along the $\langle c \rangle$ axis of the crystal. The dominant deformation mechanisms observed initially are $\langle a \rangle$ slip and extension twinning. In addition, pyramidal $\langle c + a \rangle$ slip is also observed inside the twinned region. This is similar to our observations of the deformation of extruded magnesium compressed in the extrusion direction at high strain rates (Chapter 3). In order to capture the evolution of these three mechanisms, we employ our general modeling framework

described in Section 4.2.

The orientation of the crystal with respect to the loading under $\langle a \rangle$ axis compression is such that the resolved shear stress on the basal plane is ideally zero. The CRSS of basal slip in Mg is very low ($\sim$0.5 MPa) making basal slip possible even for a slight misorientation. Therefore, basal slip which is commonly observed in Mg under many loading configurations is also observed here. In the early stages, the deformation under $\langle a \rangle$ axis compression proceeds through activation of basal slip and extension twinning in the material. The evolution of the density of $\langle a \rangle$ dislocations in the parent region is described by the equations (4.7 and 4.8) which in a succinct form are given as

$$\dot{\rho}_a = (\frac{\beta}{b_a}\sqrt{\rho_a} - \beta_r \rho_a)[1 - f]^n \dot{\epsilon} \tag{4.20}$$

The parameters β and β_r are the coefficients for the accumulation and recovery mechanisms respectively for the density of $\langle a \rangle$ dislocations. The activity of $\langle a \rangle$ slip is presumed to be high at the beginning of the deformation since $\langle a \rangle$ slip mainly occurs in the parent region. At larger strains, the twins grow to consume the parent volume. The effect of the parameters β and β_r on the mechanical behavior is very small at larger strains due to the growth of twins and increase in the twin volume fraction thus making the term (1 - f) small. Therefore, their values are chosen such that the mechanical behavior at lower strains (upto $\sim$ 5% strain) is accurately captured. At larger strains, a greater volume of the parent region transforms into

twinned region causing the density of $\langle a \rangle$ dislocations to saturate. It is assumed that due to twinning, the density of $\langle a \rangle$ dislocations is low and the recovery process does not occur. Therefore, the value of β_r (the recovery parameter) is taken to be zero.

The twinned region which is $\sim 86^0$ away from the orientation of the parent experiences compression along the $\langle c \rangle$ axis. Pyramidal slip is a favored mechanism under this loading configuration. Experimental observations show the existence of $\langle c + a \rangle$ dislocations in the twinned region. The $\langle a \rangle$ dislocations that exist in the parent region may be transmuted into $\langle c + a \rangle$ dislocations in the twinned region under the twinning shear upon interaction with the twin boundary. This mechanism proposed by El Kadiri and Oppedal [104] may explain the experimental observations of significant $\langle c + a \rangle$ dislocations inside twinned regions. As the twin volume fraction increases, more dislocations from the parent region may be transmuted into $\langle c + a \rangle$ dislocations in the twinned region therefore increasing the dislocation density. Additionally, twin boundaries may act as sources of dislocations as seen in some other metals [105].

The parameters γ and γ_r are coefficients of the dislocation accumulation term and the recovery term for the $\langle c + a \rangle$ dislocations respectively. In this case of $\langle a \rangle$ axis compression, these dislocations are inside the twinned region which is different from the case of $\langle c \rangle$ axis compression in which the dislocations were inside the original/parent crystal. Considering the transmutation mechanism above and that the twin boundaries act as sources for the $\langle c + a \rangle$ dislocations, we expect that the magnitude of the source term γ will be higher in this case. We assume that the coefficient

for the recovery term γ_r remains the same.

The values of additional constants and parameters for $\langle a \rangle$ axis compression of single crystal Mg are given in Table 4.2.

σ_0	6 MPa
α for basal-basal interaction	0.2
b_a	0.32×10^{-9} m
b_{c+a}	0.61×10^{-9} m
β	0.4
β_r	0
γ	5.6
γ_{rec}	150
Initial dislocation density, $\rho_{(i)}$	$8.7 \times 10^{11} m^{-2}$
κ	0.07
n	2

Table 4.2: Parameters used in modeling the $\langle a \rangle$ axis compression response of single crystal Mg

The Burgers vector for the $\langle a \rangle$ and $\langle c+a \rangle$ dislocations are taken from the literature [106]. The initial strength σ_0 is taken to be 6 MPa based on the experimental data [2]. The value of κ is taken to be 0.07. This value of κ describes the twin volume fraction

evolution (Fig 4.8) that matches the experimentally measured behavior. The initial total dislocation density was chosen to be the same as that in the case of $\langle c \rangle$ axis compression.

The value of the parameter n affects the rate of change of dislocation density of both $\langle a \rangle$ and $\langle c+a \rangle$ dislocations. The effect of different values of n on the dislocation densities is shown in Fig 4.5 and 4.6 and the stress-strain response in Fig 4.7. It is observed from Fig 4.5 that as the value of n increases, the accumulated density of $\langle a \rangle$ dislocations decreases. At larger strains, the rate of change of dislocation density with strain decreases, and the dislocation density tends to saturate for larger values of n.

The evolution of the density of $\langle c+a \rangle$ dislocations is also affected by the value of n as observed in Fig 4.6. In the case of $\langle c+a \rangle$ dislocations, for higher values of n, the initial rate of change of change of dislocation density (at small strains) is small but it increases at larger strains. This leads to a lower accumulated density of $\langle c+a \rangle$ dislocations for larger n at the same strain for the range of strains considered.

Due to the significant effect of the value of parameter n on the densities of $\langle a \rangle$ and $\langle c+a \rangle$ dislocations, the overall stress-strain response is also affected by the value of n. From the stress-strain response (Fig 4.7), it can be seen that the sigmoidal behavior of the curve can be captured by the higher values of n (e.g. n=2). For higher values of n, a higher rate of change of the $\langle c+a \rangle$ dislocation density with strain is obtained at larger strains (Fig 4.6) due to which the observed strain hardening effect from

the pyramidal dislocations can be captured. The parameter values that resulted in a close match with the experimental data are used to generate the results presented in Figures 4.8, 4.9, and 4.10.

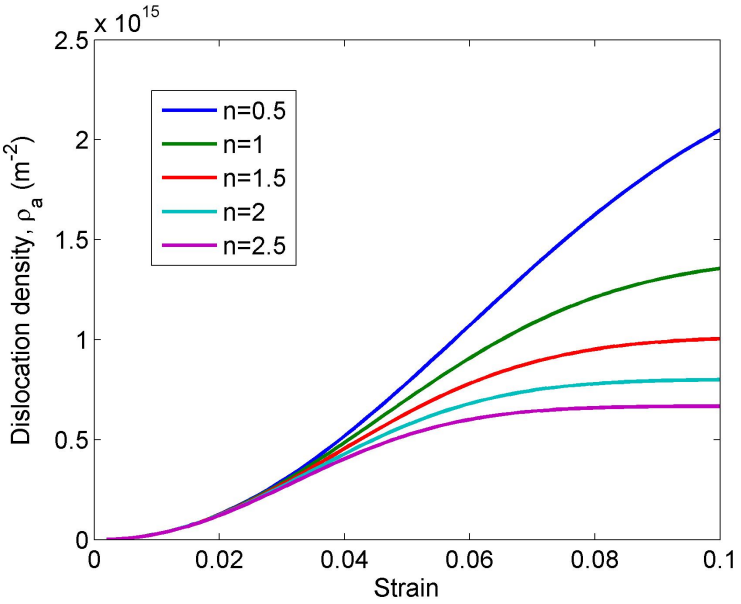

Figure 4.5: Effect of the value of parameter n from Eq 4.20 on the evolution of the $\langle a \rangle$ dislocation density

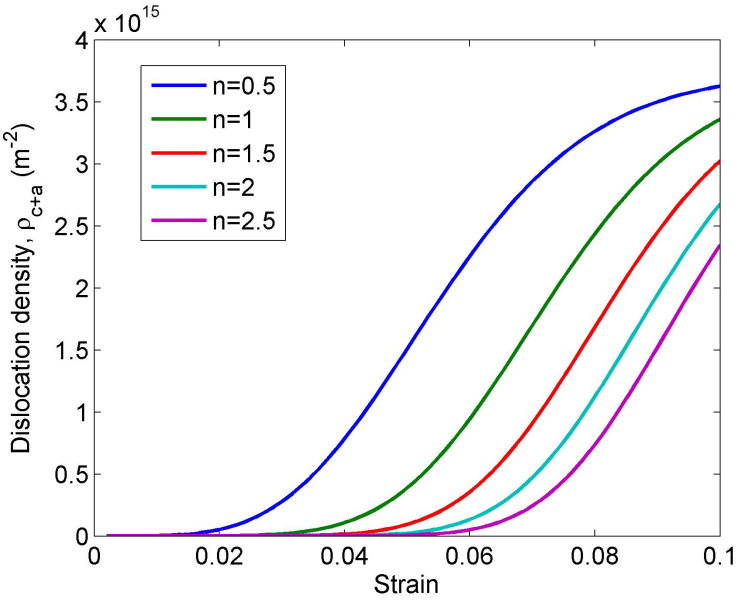

Figure 4.6: Effect of the value of parameter n on the evolution of the $\langle c+a \rangle$ dislocation density

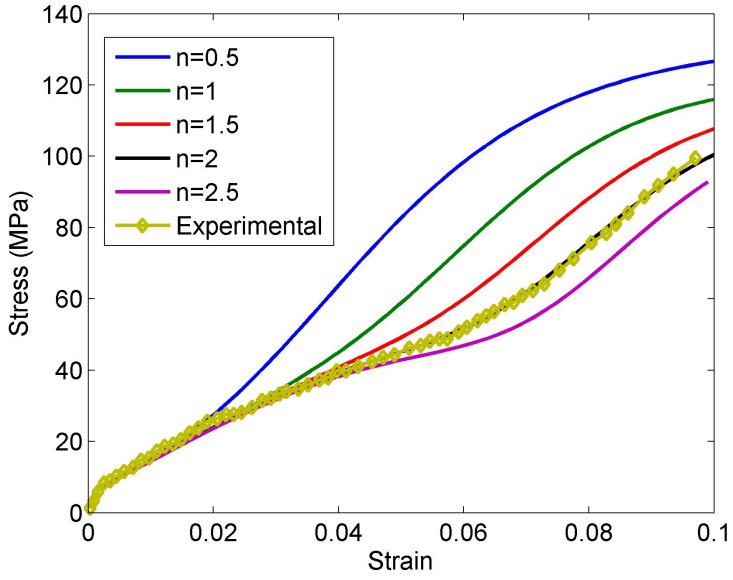

Figure 4.7: Effect of the value of parameter n on the stress-strain relationship

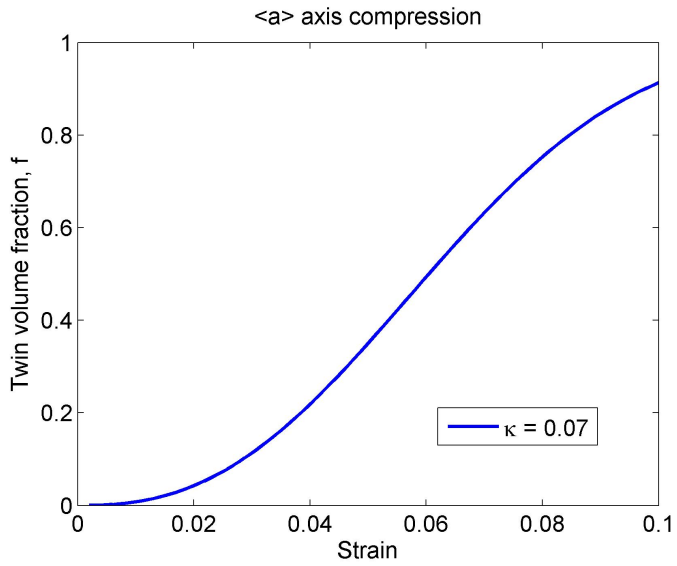

Figure 4.8: Evolution of the twin volume fraction under $\langle a \rangle$ axis compression

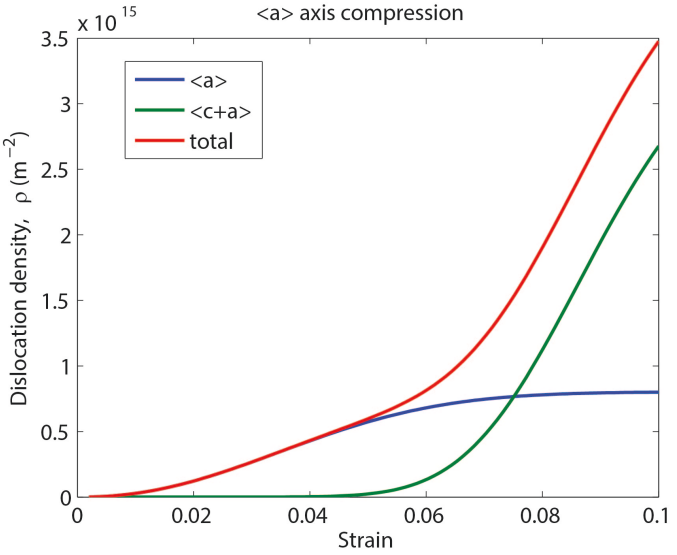

Figure 4.9: Evolution of the dislocation density under $\langle a \rangle$ compression

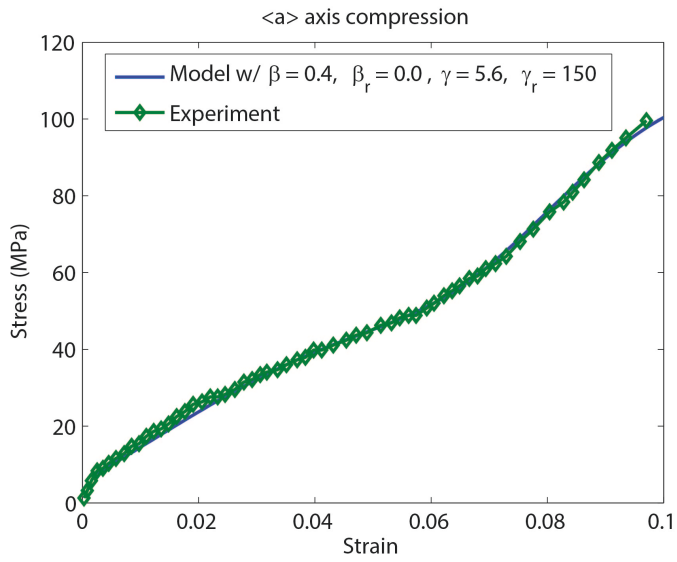

Figure 4.10: Stress-strain response under $\langle a \rangle$ axis compression. The experimental data is shown by the green line with markers and the output of the model is shown by the solid blue line

The evolution of twin volume fraction in single crystal Mg under $\langle a \rangle$ axis compression is shown in Fig 4.8. The value of κ is chosen to be 0.07 in order to match the rough estimate (from Xie et al., in preparation) of twin volume fraction ($f \approx 0.9$) at $\sim$10% strain.

The total dislocation density is composed of the density of $\langle a \rangle$ dislocations and $\langle c + a \rangle$ dislocations. TEM observations (Xie et al., in preparation) suggest that the initial dislocation density is dominated by $\langle a \rangle$ dislocations and $\langle c + a \rangle$ dislocations are very few in number. Therefore, the initial density of $\langle c + a \rangle$ dislocations was assumed to be an order of magnitude smaller than that of $\langle a \rangle$ dislocations. The

evolution of dislocation densities with strain is shown in Fig 4.9. In the early stages of deformation, the density of $\langle a \rangle$ dislocations is dominant but as the twin volume fraction increases, the contribution from the $\langle c + a \rangle$ dislocations starts to rise. The density of $\langle a \rangle$ dislocations is observed to almost saturate beyond $\sim$8% strain. The rate of increase of the $\langle c + a \rangle$ dislocation density is very high at strains greater than $\sim$7% which results in the strain hardening effect.

4.3.3 Summary of results for single crystal magnesium

The mechanism based model was successfully applied to describe behavior of single crystal magnesium. In the case of c-axis compression of single crystal Mg, pyramidal $\langle c+a \rangle$ dislocation slip was considered to be the dominant mechanism and an analytical description for the evolution of the dislocation density was developed. In the case of a-axis compression, $\langle a \rangle$ and $\langle c + a \rangle$ slip and extension twinning are the active mechanisms. Hence, the evolution of the three internal variables - (i) density of $\langle a \rangle$ dislcoations, (ii) density of $\langle c + a \rangle$ dislocations and (iii) twin volume fraction - was considered in describing the observed behavior. The model can also be applied to the deformation of single crystal Mg along different orientations where the relative activities of slip and twinning are different than that observed here.

4.4 Response of extruded Mg under compression along the ED

We have performed compression experiments on extruded magnesium in the extrusion direction (ED) at quasi-static and dynamic strain rates (Chapter 3) [107]. Experimental observations indicate that under this type of loading, the dominant deformation mechanisms are similar to those in the $\langle a \rangle$ axis compression of single crystal magnesium. There will most likely be differences in the evolution of these mechanisms due to the presence of grain boundaries. We use the same modeling framework from Section 4.2 to capture the response of this material.

The extrusion processing of polycrystalline magnesium induces a strong texture. The texture of the material is such that most basal planes are aligned parallel to the extrusion direction. To account for the effect of texture, a Taylor factor M is included in the Taylor hardening equation. The value of M is taken to be 2.5 from the literature owing to the extruded texture of the material and the nature of loading [108].

The grain size dependent strength of the polycrystalline material is accounted for by the Hall-Petch term. The average grain size of the material is 20 μm. The value of the Hall-Petch constant is taken from the literature as $k = 0.18$ MPa m$^{-1/2}$ [102]. The Peierl's stress is assumed to be 10 MPa from the average of the values reported in the literature [2, 101, 109].

The experimentally measured flow stress at yield is 60 MPa for both the quasi-

static and dynamic cases. In the twinning dominated deformation, the flow stress at yield is not sensitive to the strain rate but the strain hardening behavior is strain rate dependent. The value of the initial dislocation density is calculated to be $0.59 \times 10^{13} m^{-2}$ which is in the range estimated experimentally [103].

Table 4.3 shows the values of the parameters used in the model for both the quasi-static and dynamic loading cases. The values of the dislocation accumulation and recovery parameters are slightly different from the single crystal case due to the presence of grain boundaries and higher initial dislocation density in the extruded magnesium.

The modeling framework developed in Section 4.2 is applied to describe the behavior of extruded Mg compressed in the ED at quasi-static and dynamic rates. The twin volume fraction evolution for the quasi-static and high strain rate compression is shown in Figs 4.11(a,b). It can be observed that the twin volume faction increases from zero to >90% at a strain of 0.12 for both the quasi-static and dynamic cases. A higher value of the twin volume fraction for the same strain is obtained under high strain rate loading as compared with the quasi-static loading. The observations from Dudamell et al.'s work on AZ31 indicate that the propensity of twinning increases with increasing strain rates [60]. Therefore, we can expect that the twin volume fraction at a particular value of strain will be higher in the case of high strain rate compression. In our formulation for twin volume fraction evolution, smaller values

Parameter	Values
Flow stress at yield, $\sigma(1)$	60 MPa
α	0.2
M	2.5
β	0.15
γ (Quasi-static)	2.5
γ (Dynamic)	3.1
γ_{rec}	80
Initial dislocation density, $\rho_{(i)}$	$0.59 \times 10^{13} m^{-2}$
κ (Quasi-static)	0.085
κ (Dynamic)	0.07

Table 4.3: List of parameters used for the quasi-static and dynamic compression of extruded Mg in the ED

of the parameter κ give higher values of twin volume fraction (Fig 4.1) for the same strain. The values of κ for the quasi-static and dynamic cases used here 0.085 and 0.07 respectively.

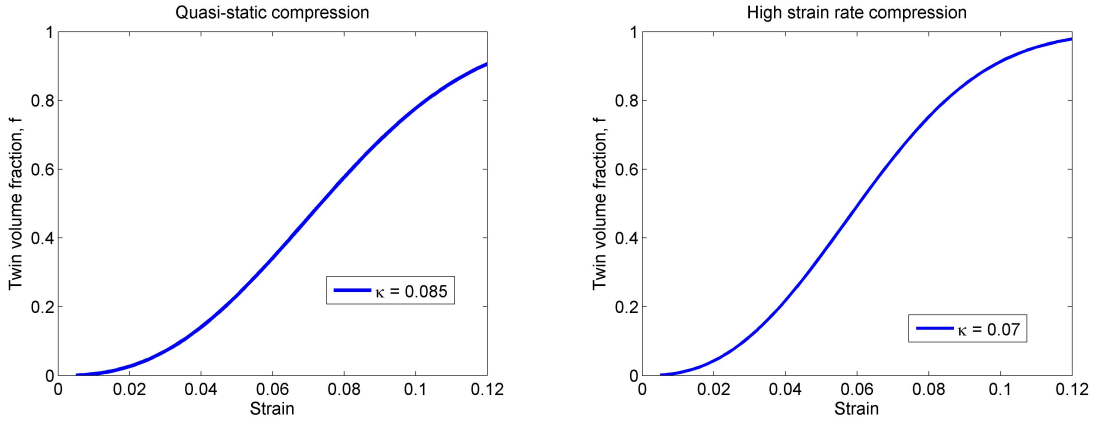

(a) (b)

Figure 4.11: Evolution of the twin volume fraction under (a) quasi-static compression and (b) high strain rate compression of extruded Mg in the ED

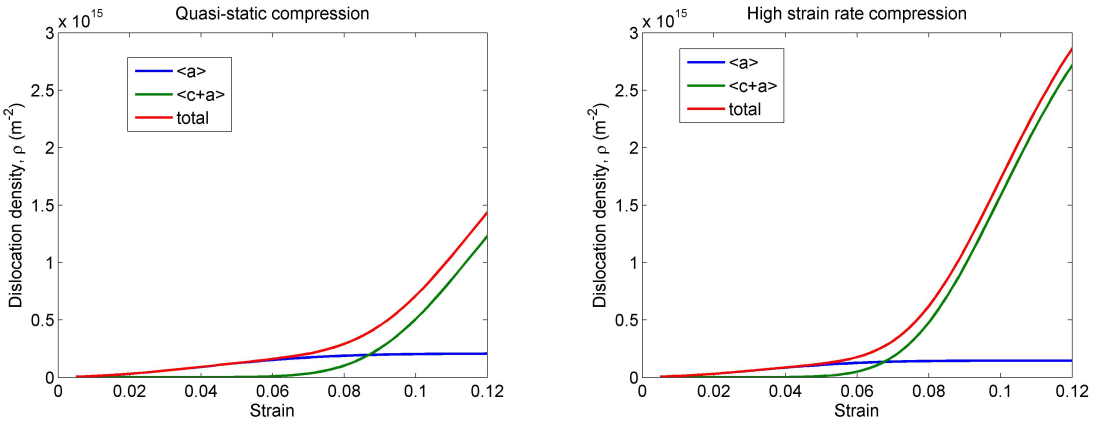

(a) (b)

Figure 4.12: Evolution of the dislocation density under (a) quasi-static compression and (b) high strain rate compression of extruded Mg in the ED

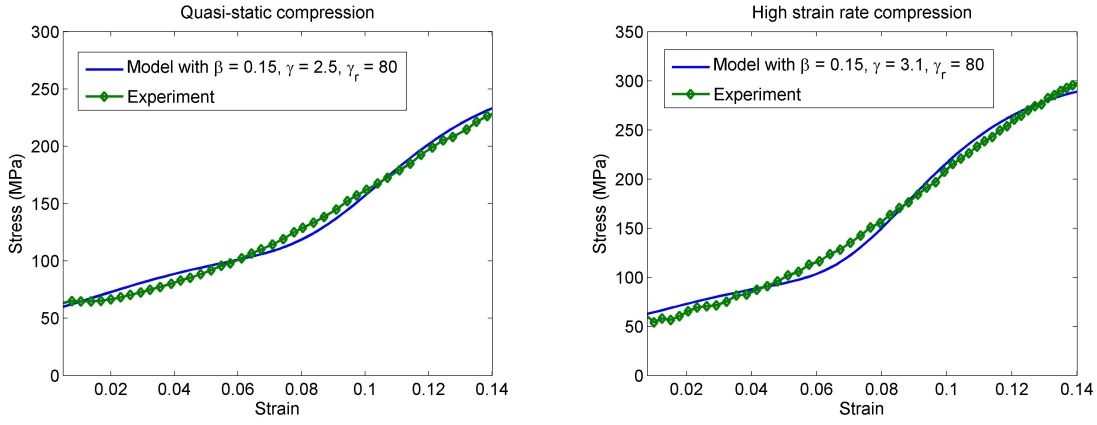

(a) (b)

Figure 4.13: Stress-strain response under (a) quasi-static compression and (b) high strain rate compression of extruded Mg in the ED. The experimental data is shown by the green line with markers and the output of the model is shown by the solid blue line

The evolution of the dislocation densities under quasi-static and high strain rate loading are shown in Fig 4.12(a,b). It can be observed that the accumulated dislocation density is higher in the case of the high strain rate compression as compared to the quasi-static compression. The coefficients β and γ account for the dislocation accumulation with deformation for the $\langle a \rangle$ and $\langle c + a \rangle$ dislocations respectively. A slightly higher density of $\langle a \rangle$ dislocations is observed in the quasi-static loading even with the same coefficient (β) of dislocation accumulation (Fig 4.12a). The reason for this is the lower twin volume fraction at a given strain in the quasi-static loading. The twin volume fraction is comparatively higher in the case of the high strain rate

loading at the same strain level. Due to the higher amount of twinning to accommodate the plastic strain, lesser activity of $\langle a \rangle$ slip is expected to be necessary in the high strain rate case for a particular strain. The density of $\langle c+a \rangle$ dislocations (and the total dislocation density) is higher for the high strain rate loading (Fig 4.12). The rate of dislocation accumulation is tied to the mean free path of dislocations. Greater dislocation densities have been observed in materials when deformed at high strain rates as compared to low strain rates. Some studies have shown that there is an increase in the active dislocation sources at higher strain rates. Dislocation generation at the shock front and effects of phonon drag at high strain rates have also been studied for different metals [110–112]. Therefore, the coefficient of the dislocation accumulation/generation term γ (for $\langle c+a \rangle$ dislocations) is assumed to be strain rate dependent in order to account for these effects. The coefficient β for ($\langle a \rangle$ dislocations) is assumed to be independent of strain rate in this case due to the ease of basal slip due to its very low CRSS as compared with the other deformation modes. A linear relationship for the coefficient of dislocation accumulation with strain rate of the form shown in Eq 4.21 was used in the case of FCC Aluminum in the work of Huskins [113].

$$\gamma(\dot{\epsilon_p}) = p + q(\frac{\dot{\epsilon_p}}{\dot{\epsilon_0}}) \tag{4.21}$$

where $\dot{\epsilon_0}$ is the reference strain rate. Due to the lack of experimental data at various strain rates, this relationship has not been calibrated for magnesium in this work

but can be added in the future. In this work, it is assumed that the value of the coefficient γ will be higher at higher strain rates and its value was chosen to fit the experimentally observed behavior.

Fig 4.13(a,b) shows the stress-strain response generated by the model (solid blue line) in comparison with the experimentally measured behavior (green line with markers) for the quasi-static and dynamic loading cases respectively. The model is able to capture the overall material behavior reasonably well. It can be observed that the flow stress at yield is similar in the two cases but the strain hardening behavior and the peak stress reached is higher in the case of high strain rate loading. The twin volume fraction evolution rate is faster in the case of the high strain rate deformation as compared to the quasi-static case (Fig 4.11). The material completes the twinning process earlier under the high strain rate loading. The combination of these two effects produces higher strain hardening in for the high strain rate case and therefore higher peak stress magnitudes are observed (Fig 4.13).

4.5 Summary

In this chapter, we have presented a simple scalar constitutive model based on the internal state variable theory. The commonly observed deformation modes in magnesium are considered in the model and the evolution equations for each of these modes are developed. The flow stress is related to the internal variables such as the

density of $\langle a \rangle$ and $\langle c+a \rangle$ dislocations and twin volume fraction through a Taylor hardening equation. The evolution of $\langle a \rangle$ dislocation density is considered separately from the evolution of $\langle c+a \rangle$ dislocations due to the significant differences in the conditions under which they are activated. The formulation for the dislocation density evolution equation is physics based and the dislocation accumulation or source term is considered to be strain rate dependent. The evolution equation for the twin volume fraction is purely empirical in the current model. The key equations from the model are given here.

The flow stress is given by

$$\sigma = \sigma_0 + \sigma_{Taylor} \tag{4.22}$$

where σ_0 is the initial strength and the contribution to the strength from dislocation-dislocation interactions is given by Taylor hardening as

$$\sigma_{Taylor} = \alpha M \mu b \sqrt{\rho_{total}} \tag{4.23}$$

The total dislocation density is composed of the $\langle a \rangle$ and $\langle c+a \rangle$ dislocation densities as

$$\rho_{total} = \rho_a + \rho_{c+a} \tag{4.24}$$

where the evolution of the density of $\langle a \rangle$ dislocations is given by

$$\dot{\rho}_a = (\frac{\beta}{b_a}\sqrt{\rho_a} - \beta_r \rho_a)[1-f]^n \dot{\epsilon} \tag{4.25}$$

and the evolution of the density of $\langle c+a \rangle$ dislocations is given by

$$\dot{\rho}_{c+a} = (\frac{\gamma}{b_{c+a}}\sqrt{\rho_{c+a}} - \gamma_r \rho_{c+a})[f]^n \dot{\epsilon} \tag{4.26}$$

The evolution of the extension twin volume fraction is given by

$$f(\epsilon) = 1 - exp[-(\frac{\epsilon}{\kappa})^a] \tag{4.27}$$

The parameters used in the model are listed in Table 4.4.

Material & Loading	β	γ	γ_r	κ	n
Single crystal (a-axis)	0.4	5.6	150	0.07	2
Single crystal (c-axis)	-	3.3	150	-	-
Extruded Mg (Quasi-static)	0.15	2.5	80	0.085	2
Extruded Mg (Dynamic)	0.15	3.1	80	0.07	2

Table 4.4: List of parameters used in the model

4.6 Future work

The current model (implemented in MATLAB) is applied to simple uniaxial loading configurations under quasi-static and dynamic strain rates. The constitutive model as presented has the capability to capture the material response but is not predictive. The model parameters for the current model were obtained from limited

set of experiments on pure magnesium. Significant experimental work has been done on magnesium alloys such as AZ31 but relatively few studies have been performed on pure magnesium. More comprehensive experimental datasets are needed in order to construct and calibrate some of the mechanism based constitutive relationships. An example is the strain rate and temperature dependence of flow stress for different textures. Note that temperature effects were not considered in this model since all the experimental data available was at room temperature.

The dislocation density evolution as well as the twin volume fraction evolution are likely to be strain rate dependent based on the experimental observations in magnesium alloys and other metals. A physics based relationship for the strain rate dependence of these mechanisms will add predictive capability to the model. Under deformation dominated by extension twinning, the flow stress at yield is observed to be insensitive to the strain rate in magnesium and its alloys [72]. Under slip dominated deformation, strain rate sensitivity of the flow stress is observed. Therefore, this strain rate dependent behavior of some deformation modes needs to be accounted for by the constitutive model. A mechanism based approach can be developed that accounts for the nucleation and growth of twins. Recent works have considered the concept of twinning dislocations that are responsible for the nucleation and growth of twins [114]. Studies on twin boundary migration in other materials (eg. Nickel [115]) have established a relationship between twinning dislocations and twin boundary velocity. The evolution of the twin volume fraction $\dot{f}$ is directly tied to the twin boundary

velocity. Similar mechanism based relationships for the twin volume evolution need to be considered for magnesium and its alloys for the models to be predictive.

The current model can be extended to be applied to model the behavior of Mg alloys. In this case, the effects of precipitates and solutes on the deformation behavior needs to be considered. The flow stress at yield and the strain hardening (and strain rate hardening) behavior may be affected by the solutes and precipitates. The evolution equations for the internal variables will need to account for the interactions with the solutes and precipitates.

Another avenue for the use of the current model is in a user-defined material model (UMAT) to be implemented in finite element codes such as Abaqus. The standard material models available in Abaqus are not able to capture the complex behavior of magnesium induced by extension twinning. The UMAT will be extremely valuable in producing material behavior that represents the actual behavior more accurately.

We have analyzed the behavior of magnesium under uniaxial stress loading at quasi-static and high strain rates thus far. We are interested in understanding the behavior of this material under complex (triaxial) stress states and loading of different durations. The results from the plate impact experiments performed on magnesium (that impose a uniaxial strain loading) are presented in Chapter 5 and the deformation mechanisms activated under this loading are also analyzed.

Chapter 5

Twinning in Extruded Mg under Normal Impact Loading

The deformation of pure extruded magnesium under high strain rate loading was described in Chapter 3. The dominant deformation mechanisms that are activated under uniaxial compression in the extrusion direction (ED) were studied, and were found to be (under this loading configuration), extension twinning, $\langle a \rangle$ slip and $\langle c+a \rangle$ slip. The strain rates imposed under the Kolsky bar loading were of the order of $10^3 s^{-1}$ and the typical duration of loading for these experiments was about $\sim 200 \mu$s. However, the dynamic loading conditions that the material can experience while being used in armor or automotive applications generally involve loading at varying strain rates, time durations and complex stress states. Therefore, it is important to understand the effect of these conditions on the behavior of magnesium. To address this, we

have performed normal plate impact experiments on the extruded pure magnesium that was studied in Chapter 3. The typical loading in these experiments is of much shorter duration ($<5\mu$s). The stress state imposed by the plate impact configuration is three dimensional (due to the uniaxial strain condition) and is very different than the uniaxial stress condition imposed by the Kolsky bars. The effect of these conditions on the deformation mechanisms is explored here through comparison of the deformation characteristics under the plate impact loading with that under the Kolsky bars.

In the recent years, a few studies have investigated the behavior of magnesium alloys under impact loading [75–77]. In the studies by Millett [75] and Hazell [77] et al., the impact velocities were high enough to generate shock in the material. Millett et al. investigated the response of the magnesium alloy AZ61 to shock loading. They observed that the shear strength of the material increases with the applied shock stress and time behind the shock front. They hypothesize that this effect is due to a deformation process that consists of early twinning followed by dislocation activity. The shock response and the spall behavior of the magnesium alloy Elektron 675 was studied by Hazell et al. by impacting the material along the extrusion direction and perpendicular to the extrusion direction. Their observations indicate that the Hugoniot Elastic Limit (HEL) and the spall strength values are higher along the extrusion direction. They also observed evidence of twinning in the recovered shock loaded material. It is very difficult to recover the shock loaded specimens for microstructural analysis while ensuring that the observed deformation is due to the initial applied

loading. Therefore, very few observations of the deformed microstructures of shock loaded specimens are typically reported and the work of Hazell et al. is particularly valuable.

We are interested here in the range of impact velocities below the full shock regime where there is elastic-plastic wave propagation. The recovery of impacted specimens in this regime is easier and the interaction of the waves with the microstructure can be studied. The normal plate impact experiments that are reported in this work all fall in this regime.

In this chapter, the deformation of extruded pure magnesium under normal impact loading is discussed. General deformation under uniaxial strain loading is discussed in Section 5.1 and the results from the normal plate impact experiments are presented in Section 5.2. We have performed 2D elastic-plastic simulations in Abaqus/Explicit to analyze the stress and strain evolution in the plates during the loading. The results of these simulations are discussed in Section 7.2. Finally, a comparison of the deformation characteristics observed under plate impact loading is made with those observed under Kolsky bar loading in Section 5.4. First, we discuss the state of stress and strain under the normal plate impact (uniaxial strain) loading.

5.1 Uniaxial Strain Loading

In the normal plate impact experiment, a cylindrical plate of material (the flyer) carried on a projectile is launched at high velocities and impacts a stationary plate (the target). The two plates are parallel to each other and perpendicular to the direction of projectile motion and therefore, the impact causes longitudinal wave propagation in both plates. The experimental configuration is shown in Figures 2.3 and 2.4 in Chapter 2. The normal plate impact loading induces a state of uniaxial strain in the direction of impact (the center of the plate is under the condition of uniaxial strain before the arrival of unloading waves from the edges of the plate). Due to the lateral constraint, the stress state is three dimensional. The geometrical configuration of the experiment is such that particle velocity histories are typically obtained only at the center of the rear free surface of the target plate. The thickness of the specimen is limited by the need to avoid interference from the release waves from the edges in order to maintain a state of uniaxial strain during the time of interest. Due to the lateral constraint imposed by the uniaxial strain condition, a higher amplitude of stress is needed to cause large plastic deformation here compared to the uniaxial stress case.

The plate impact configuration is commonly used to study shock wave propagation in materials. Typically, very high impact velocities are necessary to generate a shock in the material. A shock wave is associated with a sharp discontinuity in the state variables across the wavefront. In this work, we will not consider shock wave

propagation in magnesium.

We first consider the case of purely elastic wave propagation. The continuum analysis for such a case is presented below [116].

Let $\underline{e}_1$ represent the direction of impact and σ_1, ϵ_1 and v_1 be the stress, strain and velocity in the direction of propagation respectively. Therefore, we have

$$\rho \frac{\partial v_1}{\partial t} = \frac{\partial \sigma_1}{\partial x_1} \tag{5.1}$$

where ρ is the initial density of the material which is considered to remain constant for small dilatation. The continuity equation gives us

$$\frac{\partial \epsilon_1}{\partial t} = \frac{\partial v_1}{\partial x_1} \tag{5.2}$$

We assume the material to be isotropic in order to simplify the analysis that follows. We recognize that this is not a good assumption for anisotropic materials such as magnesium, making a more complex treatment necessary for accurate analysis of the stresses and strains during the deformation. For the isotropic material considered here, the directions $\underline{e}_2$ and $\underline{e}_3$ normal to the direction of wave propagation are equivalent. The equations of elasticity are used to relate the elastic strains to the stresses.

$$\epsilon_1^e = \frac{1}{E}[\sigma_1 - 2\nu\sigma_2] \tag{5.3}$$

$$\epsilon_2^e = \frac{1}{E}[(1-\nu)\sigma_2 - \nu\sigma_1] \tag{5.4}$$

Considering only the elastic behavior, the above equations yield the relationship

between the longitudinal stress and strain in the uniaxial strain case

$$\sigma_1 = \frac{E(1-\nu)}{(1+\nu)(1-2\nu)}\epsilon_1 \tag{5.5}$$

The longitudinal stress is related to the lateral stress by

$$\sigma_2 = \frac{\nu}{(1-\nu)}\sigma_1 \tag{5.6}$$

If the amplitude of loading is high enough, plastic yielding will occur. Theories such as J2 flow can be used to determine the stresses and strains in the plastic regime.

To account for the elastic-plastic wave propagation, the total strain is broken into elastic and plastic parts (denoted by superscripts e and p respectively) as follows.

$$\epsilon_1 = \epsilon_1^e + \epsilon_1^p \tag{5.7}$$

$$\epsilon_2 = \epsilon_2^e + \epsilon_2^p \tag{5.8}$$

The decomposition of the strain into elastic and plastic parts is valid when the strains are small. If we assume that the plastic flow is incompressible, we have

$$\epsilon_1^p + \epsilon_2^p + \epsilon_3^p = \epsilon_1^p + 2\epsilon_2^p = 0 \tag{5.9}$$

The lateral strains are required to be zero due to the uniaxial strain condition. Therefore,

$$\epsilon_2^e + \epsilon_2^p = 0 \tag{5.10}$$

Therefore, from Equations 5.9 and 5.10,

$$\epsilon_1^p = -2\epsilon_2^p = 2\epsilon_2^e \tag{5.11}$$

Therefore, total strain in $\underline{e}_1$ can be written as

$$\epsilon_1 = \epsilon_1^e + 2\epsilon_2^e \tag{5.12}$$

Equipped with this simplified understanding of the state of stress and strain in the uniaxial strain loading, we discuss the results from the normal plate impact experiments in the next section.

5.2 Normal Plate Impact Experiments

The experimental results from the plate impact experiments are discussed here. Normal plate impact experiments were conducted on pure extruded magnesium using the procedure described in Chapter 2. The direction of impact was chosen to be the extrusion direction (ED). In Chapter 3, the high strain rate experiments using the compression Kolsky bars were also conducted in the ED. The same direction was chosen for the impact experiments so as to compare the deformation characteristics under the two loading conditions. The texture of the material is such that the c-axes of the grains are randomly oriented in a plane perpendicular to the longitudinal direction (i.e. in the lateral directions). Therefore, with impact loading in the longitudinal direction (ED), an indirect tensile loading is imposed along the c-axes. Extension twinning is expected to occur under such loading in uniaxial stress condition but due

to the uniaxial strain condition in the plate impact experiment, the material is not free to expand in the lateral directions. This places a constraint on the extension of the c-axes in the lateral direction. It is therefore important to recognize that due to the state of uniaxial strain and the associated constraint on the lateral displacements in the experimental configuration, the deformation characteristics may be significantly different from the observations under uniaxial stress loading.

We are interested in investigating the mechanisms of inelastic deformation of the material. Most of the normal plate impact experiments were performed with an impact velocity in the range of 60-70 m/s. If the material remained purely elastic, this velocity would correspond to a longitudinal stress amplitude of ∼300 MPa. Some of the recent works reported the experimentally measured values of the HEL of some magnesium alloys. For AZ61, the HEL was found to be 205 MPa by Millet et al. [75]. Hazell et al. measured the shock and spall response of a magnesium alloy Elektron 675. The HEL was measured to be ∼380 MPa [77]. It is expected that the HEL for the alloys will be higher than that for pure magnesium here. The velocities corresponding to the reported measured values are in the range of 30-70 m/s (estimated from $\sigma_{HEL} = \frac{1}{2}\rho c_{el} v$ [117]). Therefore, we should expect the pure magnesium material to undergo plastic deformation, and elastic-plastic wave propagation to occur in the material with the 60 m/s impact velocity.

The flyer and the target plates in our experiments were made out of the same extruded pure magnesium material. The dimensions of the plates were designed to be

similar so as to have a symmetric impact. The experimentally measured quantities were the projectile velocity prior to impact, the misalignment between the impact faces of the flyer and target plates and the particle displacement at the free surface of the target.

5.2.1 Experimental Results

The results from the normal plate impact experiments and the quantities measured are discussed in this section. First, non-recovery type normal plate impact experiments were carried out on magnesium to test the experimental setup and diagnostics. The plate impact recovery setup discussed in Chapter 2 (Section 2.4.1) was then used to perform normal plate impact experiments with recovery of the target after impact. The impact velocities for both the recovery and non-recovery experiments were $\sim$60-70 m/s. In order to gain insight into the effect of the plate thickness/pulse duration on the wave propagation and deformation, experiments were also performed on plates with different thicknesses. The thickness values chosen were 2 mm, 3.5 mm and 7 mm. The lapping and mechanical polishing done prior to loading typically only affects a region within $\leq$100μm of the surface in the case of pure magnesium (based on a systematic analysis of polishing followed by microstructural analysis at different depths from the surface). The smallest value of thickness was chosen as 2 mm so that the region that may be affected due to the specimen preparation method is limited to a small fraction of the thickness of the specimen. As the thickness of the specimen

increases, the time between the arrival of the longitudinal wave at the free surface and the unloading waves from the specimen boundary decreases. The thickness of 7 mm was chosen so that there is still enough separation ($\sim$0.9 μs) between the arrival of the longitudinal loading wave and the release waves from the specimen boundary. At least two experiments were performed for each of the plate thicknesses at approximately the same impact velocity. The thickness of the target and the flyer plates was kept the same in order to have a symmetric impact configuration.

Test ID	Plate thickness (mm)	Projectile Velocity (m/s)	Tilt (milliradians)
Mg2E1	2	65	0.708
Mg2E2	2	60	Not recorded
Mg3E1	3.5	70	0.94
Mg3E2	3.5	Not recorded (intended to be 70)	1.18
Mg7E1	7	63	1.023
Mg7E2	7	62	0.472

Table 5.1: List of normal plate impact recovery experiments

Table 5.1 lists the impact experiments performed along with the quantities measured. The third column in the table lists the measured projectile velocity just before impact. The impact velocity varies between 60 - 70 m/s. If the material had a purely

elastic response to the imposed loading, the kinetic energy of the flyer will be completely transferred to the target plate within a very short time and the final velocity reached by the target would be exactly equal to the impact velocity after the initial wave propagation has occurred. We expect the material to undergo inelastic deformation under this range of impact velocity. Therefore, we can expect that the initial kinetic energy of the flyer plate will be transferred to the target such that a part of it is dissipated in the plastic deformation of the material and the rest as kinetic energy. Therefore, the experimentally measured free surface velocity of the target plates is typically initially lower than the impact velocity during the time of the initial wave propagation.

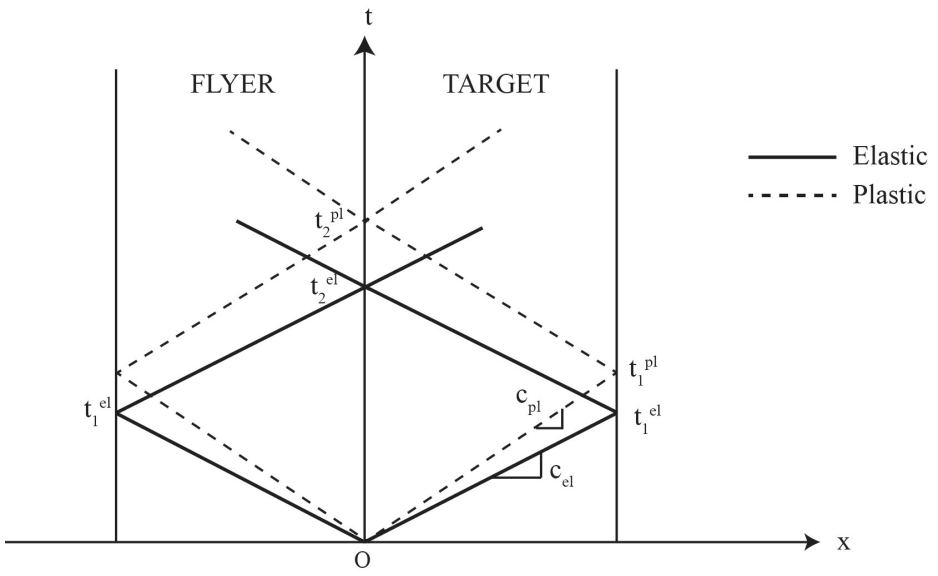

Figure 5.1: Elastic-Plastic wave porpagation in the normal plate impact configuration

When the impact velocity generates stress amplitudes above the HEL, elastic

and plastic wave propagation occurs inside the material. An idealized schematic of the wave propagation in the case of a single plastic wave is shown in Figure 5.1. Upon impact, longitudinal elastic and plastic waves are generated in both the flyer and target plates. The elastic wave (represented by a solid line) travels at a higher speed than the plastic wave (represented by the dashed line). Both these waves travel through the thickness of the plate to the rear free surface. The rear surface has a stress free boundary condition and therefore, the reflected waves from the free surface are of opposite sign. Therefore, various material points in the plates experience different states of stress that depend on the propagation and interaction of the elastic and plastic waves. For example, at the material points very close to the free surface of the target, the elastic release wave from the free surface will arrive before the plastic loading wave arrives introducing complexity in the analysis of the wave propagation.

The elastic properties of magnesium are known and can be used to estimate the longitudinal elastic wave speed in the material. The density of pure magnesium is 1740 kg/m^3 [12]. The elastic Young's modulus of the material is 44 GPa and the Poisson's ratio is 0.35. Using these values, the longitudinal elastic wave speed can be estimated to be 6370 m/s.

This calculated wave speed value from above equation is used in the further analyses in this work. The arrival times of the elastic waves at the free surface of the target can be estimated using this wave speed. The estimated arrival times (t_1^{el}) for the waves assuming a longitudinal elastic wave is propagating are given in the table

below for targets of different thicknesses.

Plate thickness (mm)	t_1^{el} (μs)
2	0.31
3.5	0.55
7	1.09

Table 5.2: Propagation times for elastic waves

The above arrival times for the waves are calculated based on the assumption of perfect impact. In reality, there is always some amount of misalignment (tilt) in the experiment. The effect of the tilt can observed in the free surface velocity history. The tilt causes a delay in the arrival of both the elastic and plastic waves and distorts the velocity history [118].

The particle displacement and velocity history at the rear surface of a 2 mm target as measured by NDI is shown in Fig 5.2 for shot Mg2E2. The NDI setup (presented in Chapter 2) consists of 2 photodiodes which are represented by Channels 1 and 2. The details of the procedure used to calculate the displacement and velocity history are given in Chapter 2 and the Appendix. The particle displacement becomes non-zero upon arrival of the elastic wave and rises thereafter. The particle velocity is calculated by numerical differentiation of the displacement-time history. It can be

observed from Fig 5.2 that the particle velocity jumps to ∼15-20 m/s upon arrival of the elastic wave at the rear surface. We do not have sufficiently high resolution data in this time to accurately capture the velocity history in this time range. There is a change in the slope around this value and the velocity continues to rise thereafter. This velocity range appears to correspond to the HEL of the material [75]. Exceeding the HEL (estimated below) causes elastic-plastic wave propagation to occur. The plastic wave travels slower as compared to the elastic wave. In the region close to the rear free surface, the elastic release wave from the free surface will arrive sooner than the plastic wave. The free surface velocity is affected by this interaction of the elastic and plastic waves and can be observed ∼50 m/s in the velocity profile in Fig 5.2b.

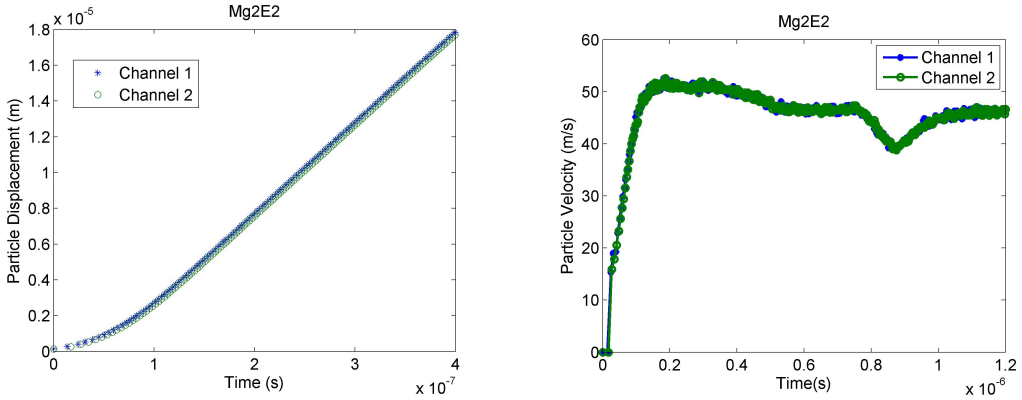

(a) (b)

Figure 5.2: Experimentally measured (a) particle displacement history and the calculated (b) partical velocity history at the free surface of 2 mm target plate (Mg2E2)

If the response was purely elastic, the rear surface velocity would jump to the

value equal to the impact velocity upon the arrival of the elastic wave and remain constant thereafter. The plastic wave travels at a slower speed and causes a slower rise in velocity as observed in Fig 5.2b. The waves reflected from the free surface travel back towards the impact surface of the target as well as the flyer. At the impact surface, these waves interact with the ones reflected from the rear surface of the flyer. In reality, there is some difference in the thickness of the flyer plate compared to the target. Therefore, the waves reflected from the back surface of the flyer and the target will arrive at the impact surface at slightly different times. The information about the reflection of the waves from the impact surface arrives at a later time in the experiment shown in Fig 5.2 and is seen in the free surface velocity history at $\sim$0.9 μs which is the time needed for the elastic wave to travel through the 2 mm thick target 3 times (3 x t_1^{el}). If the response of the material remained purely elastic, the free surface velocity would remain constant at 60 m/s and there will be no dip in the profile as is observed here.

The experimentally measured free surface velocity histories for the 2 mm, 3.5 mm and 7 mm targets are plotted in Figures 5.3, 5.4, 5.5. Two examples of the experimentally measured velocity profiles (from 2 different impact experiments) are plotted for each thickness. The velocity calculated from one of the diodes (channels) is shown for each of the experiments. Note that due to the difference in the target thicknesses, the waves arrive at the free surface at different times for each target.

The data is shifted so as to have the arrival time at the free surface as 0μs for ease of visualization and comparison.

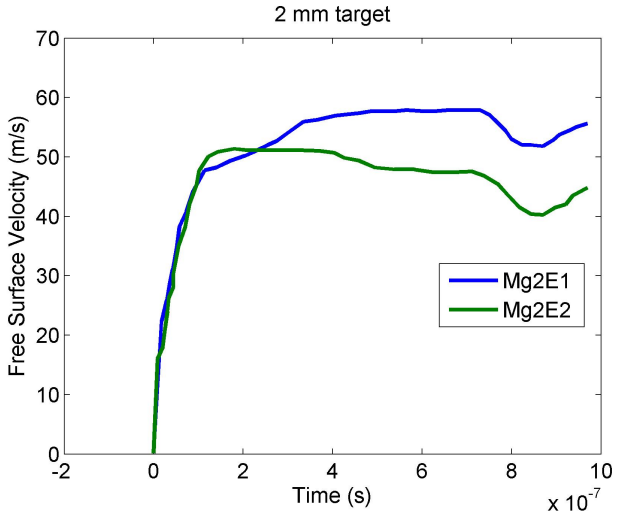

Figure 5.3: Experimentally measured particle velocity history at the free surface of 2 mm target plate

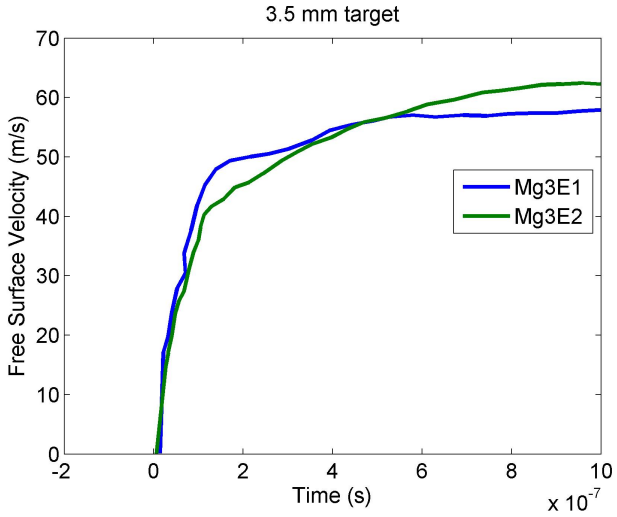

Figure 5.4: Experimentally measured particle velocity history at the free surface of 3.5 mm target plate

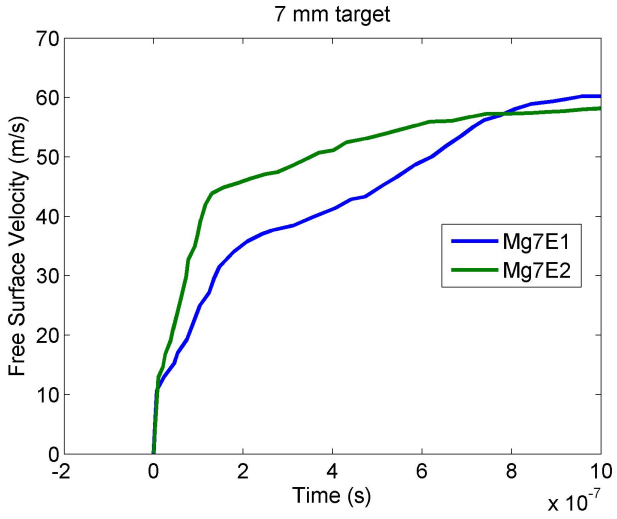

Figure 5.5: Experimentally measured particle velocity history at the free surface of 7 mm target plate

Upon arrival of the elastic wave, the particle velocity at the free surface rises rapidly. It appears that there is a change in the slope in the velocity history at $\sim$ 15 - 20 m/s for targets of all thicknesses (Figures 5.3, 5.4, 5.5). Assuming that this break in slope corresponds to the elastic limit [75], the HEL is estimated to be

$$\sigma_{HEL} = \frac{1}{2}\rho c_{el} v_{fs} \tag{5.13}$$

giving $\sigma_{HEL} \approx 97$ MPa from these measurements for the average free surface velocity of 17.5 m/s.

However, due to the complex strain hardening and strain rate dependent material behavior, a single plastic wave likely does not develop. Instead, the initial sharp rise in the velocity due to the elastic wave is followed by a gradual increase in the velocity

as the information about the plastic deformation arrives at the rear surface. Another break in the slope is observed in the velocity history around 40 - 50 m/s (Tests Mg2E1, Mg3E1, Mg3E2, Mg7E1 and Mg7E2). This break in slope appears at lower velocities for thicker targets (Fig 5.6). This is likely due to the interaction of the elastic and plastic waves in the regions close to the free surface. The free surface velocity rises to its peak value due to the arrival of the plastic wave at the rear surface.

It can be seen from figures 5.3, 5.4, 5.5 that there are differences in the velocity profiles from different experiments for each target. For the 2 mm target (Fig 5.3), the velocity for Test Mg2E2 is observed to rise to the peak value sooner than that for Test Mg2E1. This is mainly due to the different level of misalignment (tilt) in the two experiments. Test Mg2E2 has smaller tilt than Test Mg2E1 (based on the NDI data). The velocity for the experiment with smaller tilt (Mg2E2) appears to rise to the peak value faster that the experiment with higher tilt. There is also a difference in the peak values of velocity between different experiments for the same thickness. This difference primarily arises due to the slight differences in the impact velocities for different experiments. Similar observations are made for the velocity histories for the 3.5 mm target (Fig 5.4) and 7 mm target (Fig 5.5). The velocity rises to the peak value faster for Test Mg3E1 (smaller tilt) as compared to Test Mg3E2. Similar is the case for the 7 mm targets - Test Mg7E2 (smaller tilt) exhibits a faster velocity rise compared to Test Mg7E1. It is observed from the experimentally measured velocities that the target velocity does not appear to reach the impact velocity but remains

slightly lower. It is likely that there is some residual velocity in the flyer which causes the velocity of the target to be lower (due to the conservation of linear momentum). Also, due to the misalignment (tilt) involved, there is a lateral component of velocity and the normal velocity component is expected to be slightly lower than the measured projectile velocity.

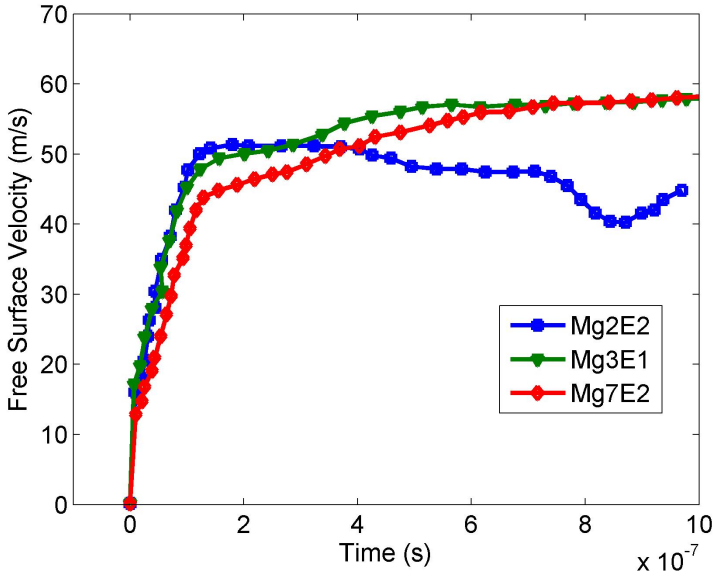

Figure 5.6: Experimentally measured particle velocity history at the free surface of targets of different thicknesses

A comparison of the experimentally measured free surface velocity histories for targets with the three different thicknesses is shown in Fig 5.6. The experiments with smaller tilt (Tests Mg2E2, Mg3E1 and Mg7E2) were chosen for comparison purposes. For all the thicknesses, an inflection point is observed at ∼15 m/s (could

not be resolved well due to lack of high resolution data during this time) followed by a change in the slope of the velocity time history in the range of 40-50 m/s. The free surface velocity is observed to reach it's peak value fastest in the case of the 2 mm target, followed by the 3.5 mm target and slowest for the 7 mm target. The plastic wave travels at a slower speed than the elastic. Therefore, as the propagation distance increases, the difference between the arrival times of the elastic and plastic waves increases therefore resulting in the observed delay in reaching the peak velocity for the thicker targets. Note that the impact velocity is not exactly the same for different experiments due to the inherent variability in the experimental conditions. This results in different values of the peak velocity reached by the target across different experiments.

The plastic response of magnesium under plate impact loading is not well characterized. Therefore, in order to understand the correlation between the observed velocity profiles and the deformation mechanisms, we need to analyze the microstructure of the deformed plates. This will enable us to link the observed deformation behavior and the resulting mechanical response.

5.2.2 Microstructural analysis

The target plates deformed under the normal plate impact loading were recovered using the recovery setup discussed in Chapter 2. The microstructure of these targets was analyzed using optical microscopy (Section 5.2.2.1) and electron back scattered

diffraction (EBSD) (Section 5.2.2.3).

5.2.2.1 Optical microscopy

In order to investigate the effect of the plate thickness on the wave propagation and the deformation mechanisms, the microstructure of the impacted plates of different thicknesses was analyzed. The pulse duration here is the time over which the deformation (elastic + inelastic) occurs. The thickness of the plate determines this duration through the time needed for the reflection of the waves from the free surface back into the target plate. Therefore, the shortest pulse duration is for the 2 mm target and the longest for the 7 mm target. The target plates of different thicknesses were recovered after the plate impact loading and were sectioned into smaller specimens for optical microscopy. Mechanical polishing down to 5μm with SiC paper was performed and the specimen was then chemically etched with a solution containing 10% nitric acid in distilled water. The micrographs shown are of the specimens prepared in such a way that the impact and the free surfaces are towards the left and the right side of the image respectively (Fig 5.7). This point of view was chosen so that any variation in the deformed microstucture through the thickness of the sample will be captured. In Fig 5.8, the terminology used in describing the morphology of the extension twins is shown.

The extension twins seen here are generally lenticular in shape. In many cases (but not all) they are observed to originate from the grain boundaries or triple junctions.

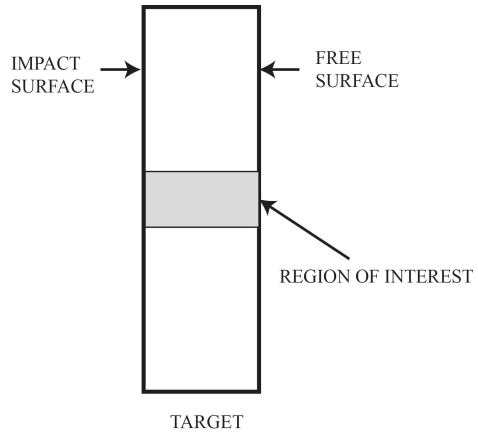

Figure 5.7: Schematic showing the central region of the target plate analyzed with optical microscopy

The length of the twins is generally greater than the width. Therefore, it may be argued that it is easier for the twin to grow in length rather than grow laterally to increase the twin width. Many twins seem to run across the entire grain and are stopped by the opposite grain boundary. For the twins that end inside a grain, we identify the leading tip as the twin tip. The boundaries that define the twin width are identified as twin boundaries. Several micrographs showing twins (Figures 5.9, 5.10 and 5.11) are shown for specimens of different thicknesses. The average twin length and twin width were measured by analyzing these micrographs with the commercial image analysis software ImageJ.

Target plates of the three different thicknesses (2 mm, 3.5 mm and 7 mm) were polished and etched in order to understand the differences in the deformation characteristics. The region at the center of the plate (as shown in Fig 5.7) was chosen

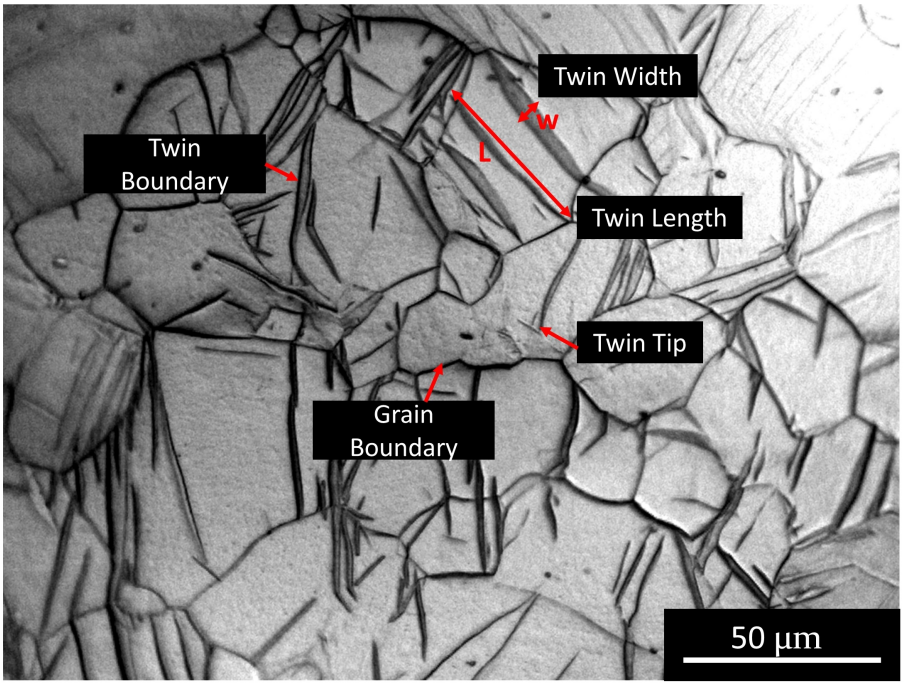

Figure 5.8: Optical micrograph showing twins in a deformed magnesium target (Test Mg2E2). The dark lenticular regions are twins. Various features in the twin morphology are identified in the figure

for the investigation as this region is least affected by the unloading waves from the boundary. In the case of the 3.4 mm and 7 mm targets, only the area within 2 mm from the impact surface was analyzed for comparison with the 2 mm target. Fig 5.9 shows the microstructure of the deformed 2 mm target after etching. The etchant attacks higher energy sites in the microstructure such as the grain boundaries and the twin boundaries. The images show the microstructure such that the impact face is towards the left side of the image and the free surface is towards the right side. There is a variation in the microstucture in terms of the amount of twinning through

the thickness of the 2 mm target as can be observed in Fig 5.9. Some regions are heavily twinned whereas some regions are almost free of twins.

The microstructure of the 3.5 mm target is shown in Fig 5.10. In this case also variation is observed in the microstructure in terms of the distribution of twins. The overall number of twins is observed to be smaller in the 3.5 mm target as compared to the 2 mm target.

Fig 5.11 shows the microstructure of the 7 mm target. A significant difference in this microstructure can be seen as compared to the thinner specimens. There are very few twins in the microstucture.

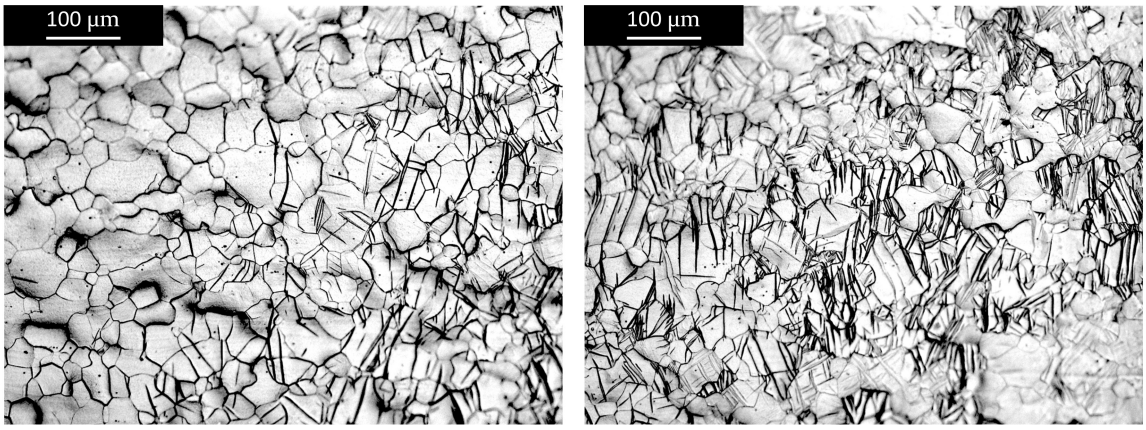

Figure 5.9: Optical micrograph of a 2 mm thick deformed target of 2 mm thickness (Test Mg2E2). Direction of impact is from the left towards the right

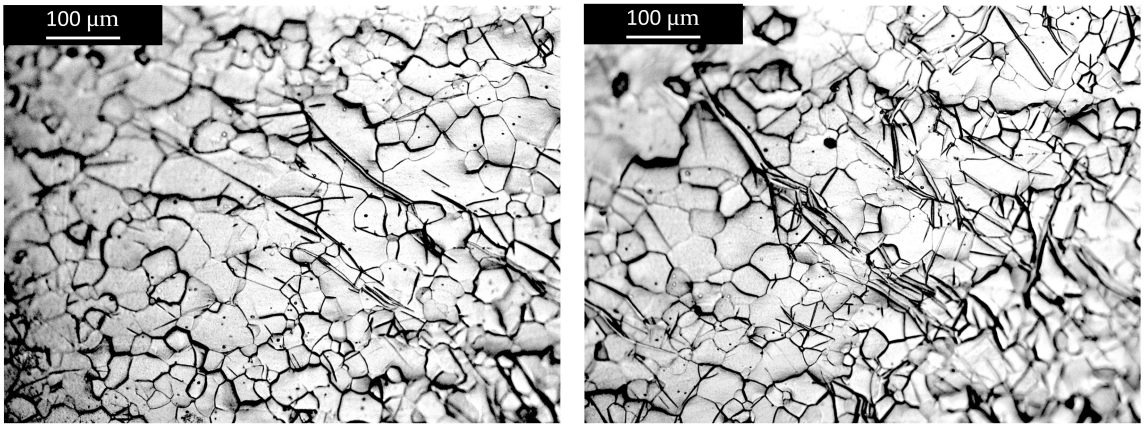

Figure 5.10: Optical micrograph of a 3.5 mm thick deformed target (Test Mg3E1)

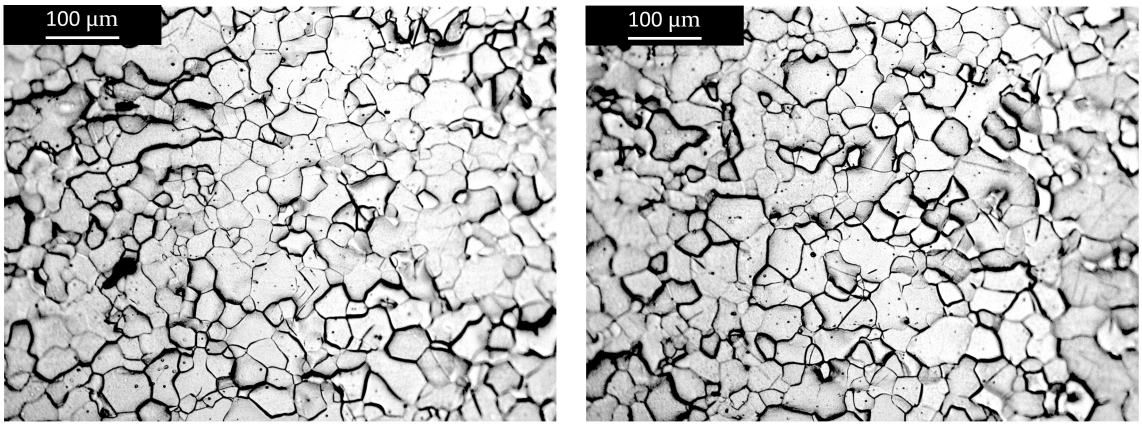

Figure 5.11: Optical micrograph of a 7 mm thick deformed target (Mg7E2)

The average length of the extension twins was found to be ∼21 μm (over a range of 10.2-37 μm) μm and the average width was found to be ∼4 μm (over a range of 1.6-5.4 μm) (based on the analysis of 6 micrographs, 2 for each sample thickness).

5.2.2.2 Estimation of twin velocity

The average twin sizes (twin length and width) calculated from the micrographs can be used to estimate the twin tip and twin boundary velocity. The approximate pulse duration in the normal plate impact experiments is ∼1-2 μs. The deformation twins that are observed in the deformed targets are formed within this time. The twin length is generally observed to be much larger (comparable to the grain size) than the twin width. We identify two velocities - twin tip velocity and twin boundary velocity.

The nominal twin tip velocity is estimated to be

$$v_{Tip} = \frac{L_{avg}}{\Delta t} = \frac{21\mu m}{1.1\mu s} = 19m/s \tag{5.14}$$

The nominal twin boundary velocity is estimated to be

$$v_{TB} = \frac{W_{avg}}{\Delta t} = \frac{4\mu m}{1.1\mu s} = 3.6m/s \tag{5.15}$$

The pulse duration for the 2 mm target (Δt = 1.1 μs is used here since the twin size statistics are dominated by the 2 mm sample since it contains the most number of twins). The twin tip velocity is greater than the twin boundary velocity based on the twin morphology.

Note that these estimates are lower bounds on the twin tip and boundary velocities. The maximum time duration available for the twins to grow to the measured sizes is the pulse duration. Twin growth may, however, happen during a fraction of this time which will result in much higher twin tip and twin boundary velocities. Due

to the nature of the experiment, only a post-mortem analysis is feasible which lets us calculate bounds on the velocities and not the accurate values.

The finite element analysis presented in Section 5.3 shows that the plastic strain rates are high only for a short duration ∼50 ns during the impact loading. Twin growth likely takes place within this time. Therefore, the estimated twin tip and twin boundary velocities based on this time duration are v_{Tip} = 420 m/s and v_{TB} = 80 m/s respectively.

5.2.2.3 EBSD analysis

Magnesium has two commonly observed modes of twinning - extension twinning and contraction twinning (as discussed earlier). Double twinning is also observed in some cases [25]. In order to characterize the twins induced by the normal plate impact loading, electron back scattered diffraction (EBSD) analysis was performed on the recovered specimens. The deformed target plates were recovered after the experiment and sectioned by EDM to obtain specimens for analysis. These specimens were then mechanically polished with SiC paper down to a 1200 grit (5μm) finish. Electrochemical polishing was then performed using a LectroPol-5 system with a 5% nitric acid in methanol electrolyte at 0^0C and a voltage of 20V. The specimens were immediately placed inside the SEM to avoid surface oxidation. The EBSD technique is very sensitive to the surface conditions due to the low penetration depth of the

electrons (∼100 nm). The region at the center of the target plate was analyzed (as shown in Fig 5.7).

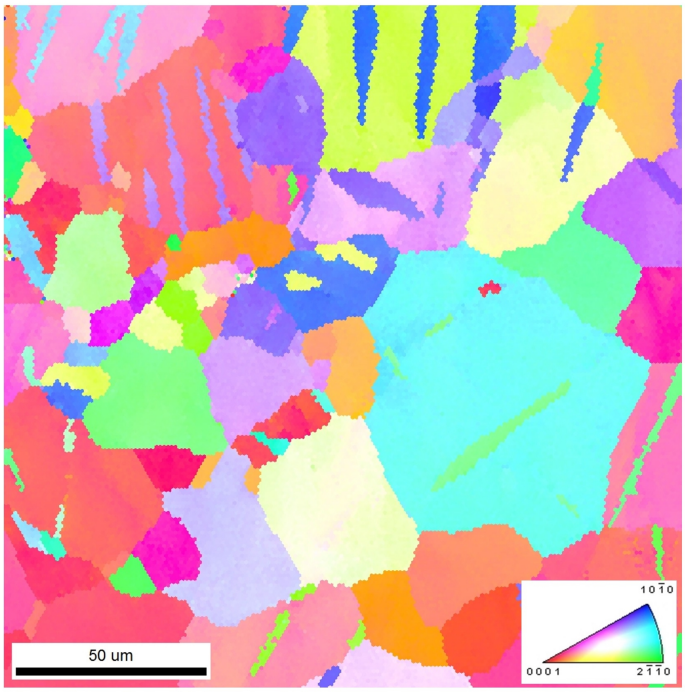

Figure 5.12: EBSD inverse pole figure in the through thickness direction of the specimen deformed under normal plate impact loading (Test Mg3E1)

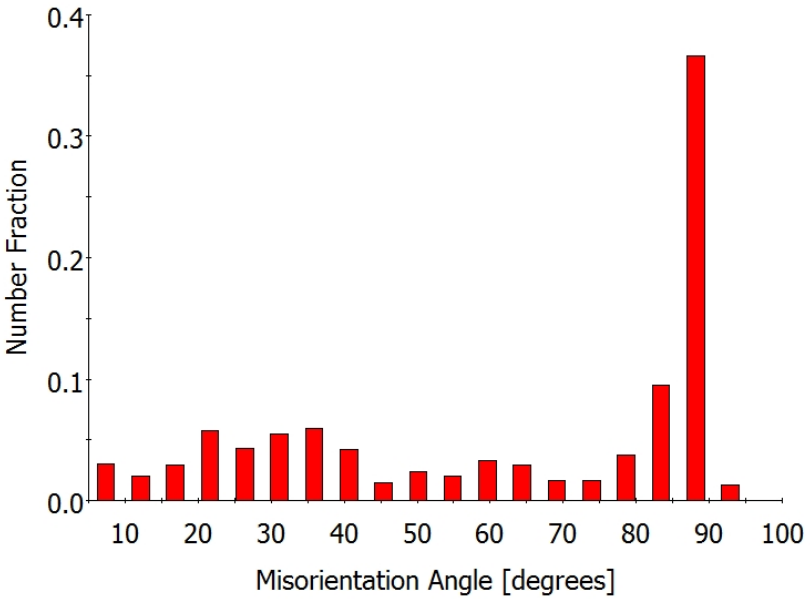

Figure 5.13: Misorientation angle distribution calculated from the EBSD data presented in Fig 5.12

The inverse pole figure as measured by EBSD is shown in Fig 5.12. Many lenticular shaped twins can be observed. Most of these twins are extension twins as can be observed from the misorientation angle distribution shown in Fig 5.13. The strong peak in the 85^0-90^0 range corresponds to the extension twin boundaries present in the microstructure. The morphology of these twins appears to be different than those formed under the high strain rate loading imposed by the Kolsky bars. The twins in this case are thin and coalescence of separate twins is generally not observed. We performed a few high resolution scans in regions where the topology of the grains looked interesting. One such example if shown in Fig 5.14. The inverse pole figure

map shows that the twin is actually composed of different regions that correspond to different orientations. The point-to-origin misorientation profile across the black line in Fig 5.14 is shown in Fig 5.15.

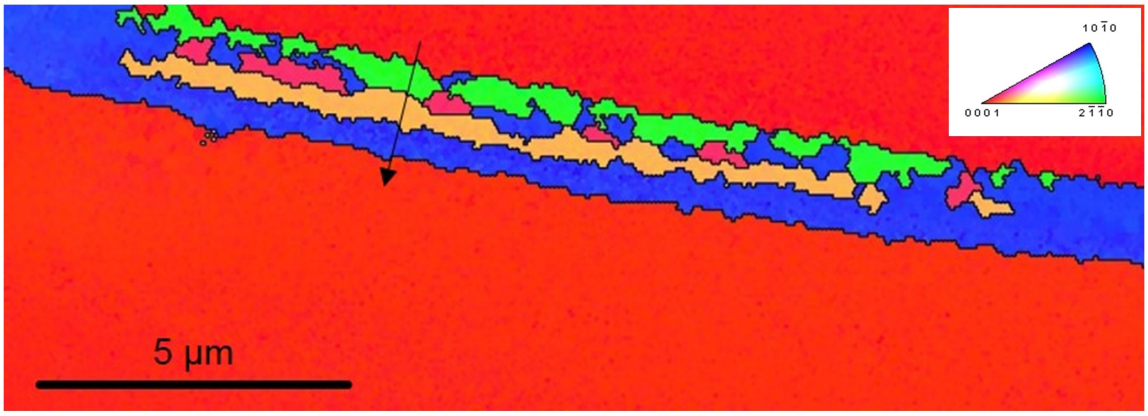

Figure 5.14: EBSD inverse pole figure map of a region in a grain within a deformed target (Test Mg3E1)

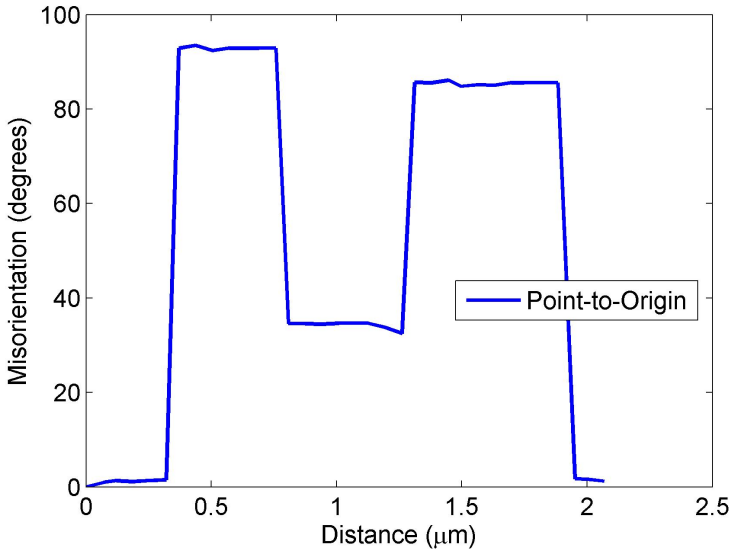

Figure 5.15: The point-to-origin misorientation profile across the black line in Fig 5.14

The different colors in Fig 5.14 represent different crystallographic orientations as represented by the map key in the inset of the figure. The orientation of the parent grain is represented by the red color and is close to the (0001) orientation. The point-to-origin profile (in Fig 5.15) represents the misorientation between each point on the black line with respect to the parent grain orientation. In the line profile, $\sim 86^0$ change in the misorientation is observed upon crossing the first extension twin boundary to enter the green twin. Upon crossing the boundary between the green and the yellow twins, a smaller misorientation of $\sim 38^0$ (with repect to the parent orientation) is observed. The yellow twin is actually a contraction twin most likely formed through a double twinning mechanism. The misorientation relationship for a double twin in magnesium has been discussed by Nave and Barnett [25]. The next

crossing is the boundary between the yellow and the blue extension twin to enter the blue twin which is $\sim 86^0$ away from the parent orientation. The blue and the green twins are both extension twins but have slightly different in-plane orientations; one being the first order prismatic and the other being the second order prismatic orientation respectively (as represented in the map key in the inset). These are known as variants of the extension twin. There are six possible variants of the $\{10-12\}$ extension twin in magnesium. The respective twinning planes and directions are given below (Table 5.3) [83].

Extension twin variants
(0 1 -1 2) [0 -1 1 1]
(-1 1 0 2) [1 -1 0 1]
(1 0 -1 2) [-1 0 1 1]
(0 -1 1 2) [0 1 -1 1]
(1 -1 0 2) [-1 1 0 1]
(-1 0 1 2) [1 0 -1 1]

Table 5.3: Extension twin variants [1]

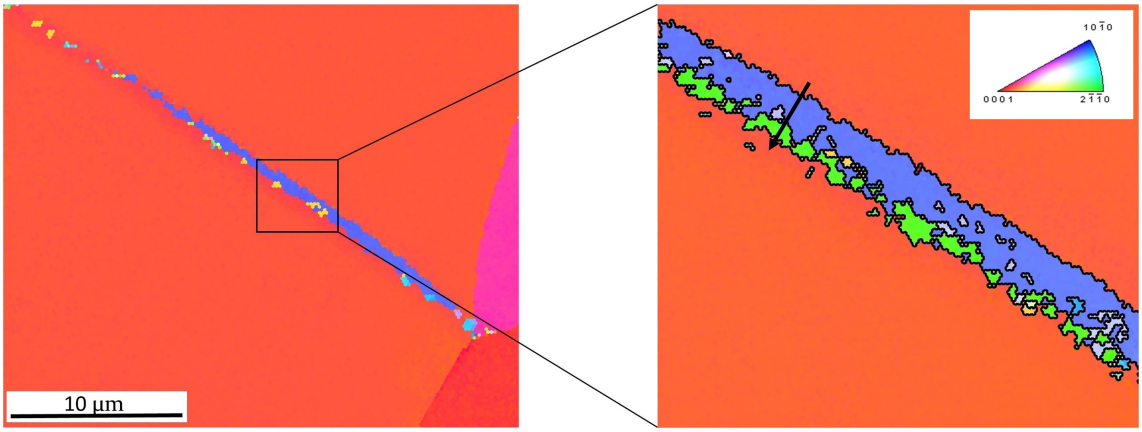

Figure 5.16: EBSD inverse pole figure map (a) An extension twin that nucleated from a triple junction (b) Closer view of the portion marked by the black square with a finer EBSD scan (Test Mg3E2)

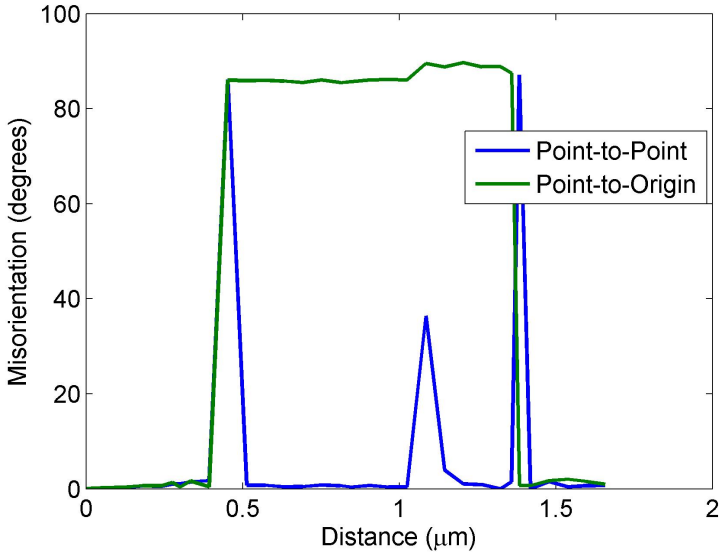

Figure 5.17: Point-to-point (blue line) and point-to-origin (green line) misorientation profile across the black line in Fig 5.16

In many cases, the extension twins are observed to nucleate from the grain boundaries or triple junctions due to the local stress concentrations. An example of this is shown in Fig 5.16. The higher resolution scan of the area marked by the black square is shown in the figure on the right side. The higher resolution scan shows the two different extension twin variants which were not well captured by the coarser scan. The misorientation profile across the black line marked in Fig 5.16 is shown in Fig 5.17. The point-to-origin (green line) misorientation profile shows that both the blue and the green twins are extension twins that $\sim 86^0$ away from the parent orientation. The point-to-point (blue line) shows the misorientation between the two extension twin variants. Many of the twins investigated in the analysis showed the multiple twin variant structure. The blue and the green twin orientations appear to correspond to the first and second order prismatic planes the misorientation betweeen which is $\sim 30^0$. In the case of the plate impact loaded specimens, nucleating multiple twin variants appears to be favorable instead of growth of the same twin variant. The dynamic nature of loading due to wave propagation most likely is the reason for the observed twin morphology under which much shorter time is available to the material to accommodate the deformation.

Plasticity in magnesium can be carried through two mechanisms - dislocation slip and twinning. Which of these mechanisms is dominant depends upon multiple factors - the nature of loading with respect to the orientation of the crystals, temperature, loading rates etc. Both the mechanisms may be active depending upon the loading

conditions. The optical micrographs shown above only bring out the twin boundaries that exist in the microstructure. Information about dislocations cannot be obtained from these images. Transmission electron microscopy analysis is needed to analyze the dislocations in the material. The deformation mode in the material will depend on the local stress state, loading rate and the local grain orientation. It is important to analyze the effect of these variables in order to understand the differences in the observed deformation. We have performed simulations mimicking the normal plate impact experiment in Abaqus/Explicit to obtain estimates of the stresses and strains, and this is discussed next.

5.3 Normal Plate Impact Simulations in Abaqus/Explicit

In this section, normal plate impact simulations performed using the commercial finite element package Abaqus are discussed. Due to the geometrical constraints imposed by the uniaxial strain configuration of the normal plate impact experiment, measurement of quantities is limited to the free surface. The particle velocity at the free surface is the only measurement of the material response we have during the experiment. If the material remained purely elastic during the deformation, the free surface particle velocity history can be used to estimate the entire stress and strain

history through the sample thickness. In our experiments, the material undergoes plastic deformation and the response of the material under this plastic deformation is not well characterized. The nature of the elastic-plastic wave propagation is such that the stresses, strains etc. vary though the plate thickness during deformation. Unless we know the precise elastic-plastic constitutive behavior of the plate material, it is not possible to calculate the complete deformations through the thickness from the measured quantities at the free surface.

In order to understand the reasons for the observed differences, it is instructive to study the evolution of the stress, strain and strain rate in the targets during deformation. In order to obtain an estimate of the stresses and strains experienced by the material during the deformation, we have performed finite element simulations in Abaqus/Explicit mimicking the normal plate impact experiments. The observations presented in Section 5.2.2.1 show significant differences between the deformed microstructures of the targets of different thicknesses. Therefore, simulations with plates of three different thicknesses have been performed.

A magnesium flyer plate impacting a magnesium target plate is simulated using a 2D plane strain configuration. The diameter of the flyer and target plates was taken to be 25.4 mm and three different thickness values of 2 mm, 3.5 mm and 7 mm were used to simulate the different experiments. The flyer plate is given an initial velocity of 60 m/s and the target plate is initially stationary. The top and bottom edges of the flyer and target plates are constrained to have zero displacement in the

lateral direction in order to simulate the uniaxial strain condition. The schematic of the setup is shown in Fig 5.18 below. The target and flyer plates were discretized into elements of 10μm thickness. This thickness proved to be sufficient to ensure convergence of the solution and no significant changes in results were observed for elements of smaller thickness. The details of the development of the simulations are given in Appendix. The strain rate dependent material model and the results are discussed here for conciseness.

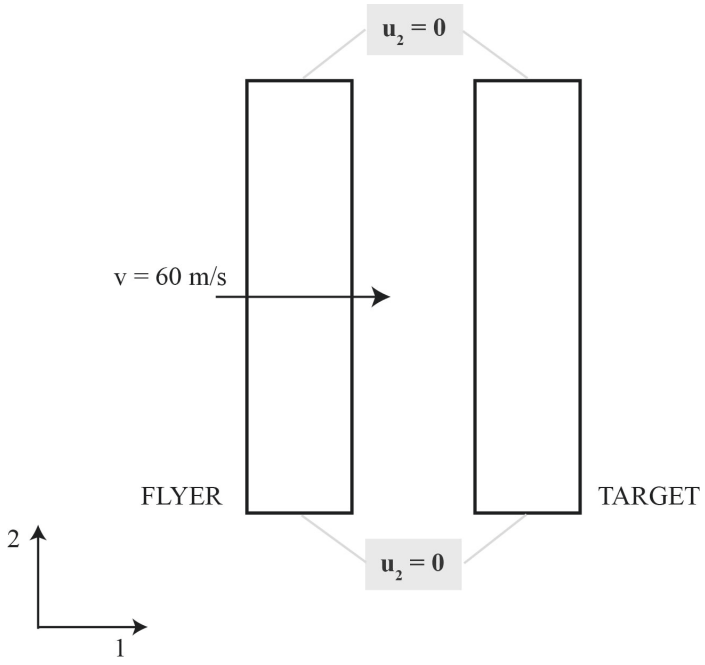

Figure 5.18: Simulation setup in Abaqus

5.3.1 Strain rate dependent model based on experimental material behavior

The behavior of magnesium when compressed in the ED was discussed in Chapter 3. The flow stress is observed to be insensitive to the strain rate whereas the strain hardening was observed to be strain rate dependent (the experimentally measured stress-strain response during uniaxial stress compression at quasi-static and dynamic strain rates is shown in Fig 5.19). The strain rate dependent response (as seen in Chapter 3) of this material is such that the flow stress at yield in the ED direction is not very rate sensitive. But the strain hardening behavior is sensitive to the strain rate.

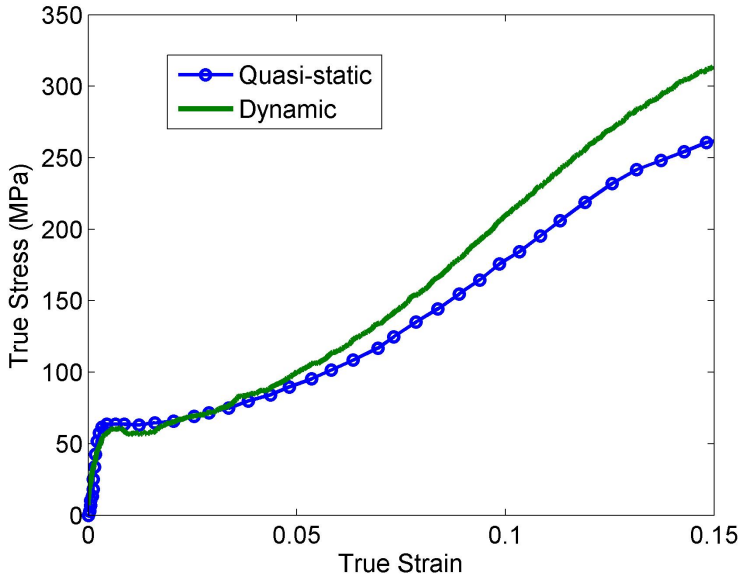

Figure 5.19: Stress-strain response of extruded magnesium under quasi-static and dynamic compression in the ED

In order to represent the actual material behavior more accurately, we use a strain rate dependent elastic-plastic material model in Abaqus/Explicit that is based on von-Mises plasticity. The rate dependence is implemented through a simple overstress Cowper-Symonds power law in Abaqus/Explicit. This form of rate dependence results in a yield stress that is strain rate dependent (which is not accurate for extruded magnesium compressed in the ED). Although, this formulation does not capture the actual material response accurately, this behavior was chosen for simplicity. The experimentally measured stress-strain response at quasi-static and dynamic strain rates was used to parametrize the rate dependent model. The overstress power law is given as

$$\dot{\bar{\epsilon}}^{pl} = D(R-1)^n \tag{5.16}$$

where $R = \frac{\bar{\sigma}}{\sigma^0}, \bar{\sigma} \geq \sigma^0$, with σ^0 the static yield stress and $\dot{\bar{\epsilon}}^{pl}$ the equivalent plastic strain rate. D and n are material parameters.

The data from the quasi-static and dynamic (Kolsky bar) experiments performed on this material is used to find the parameters D and n in the overstress power law. Due to the rate dependence of the strain hardening, the choice of the strain at which the flow stress values were picked will influence the values of the constants. We pick the flow stress values at a strain of 5% at strain rates of $2\times10^3 s^{-1}$ and $4\times10^3 s^{-1}$ since the confidence in the dynamic experimental data is low at smaller values of strain. The value of the constants obtained using the experimental data was found to be D = 26 x $10^3 \mathrm{s}^{-1}$ and $n = 1.35$.

The experimentally measured quasi-static stress-strain response is represented by the solid blue line in Fig 5.20 from which the value of σ_0 was taken. The above relationship gives stress-strain response at various rates as shown by the green and black dashed lines. It can be observed that the power law does not accurately capture the high strain rate behavior that is observed experimentally (represented by the red line). Therefore, the results of the simulation are not expected to reproduce the actual strain rate dependent material response accurately but provide us with a general understanding of the material behavior. The variation in the flow stress with strain rate calculated from the overstress power law (using the stress values at 5% strain) is shown in Fig 5.21 by the solid blue line. The black, red and green markers show the experimental values, each at a different strain rate. Note that if the stress value at a different value of strain are chosen to parametrize (D and n) the overstress power law, the nature of the blue line will change.

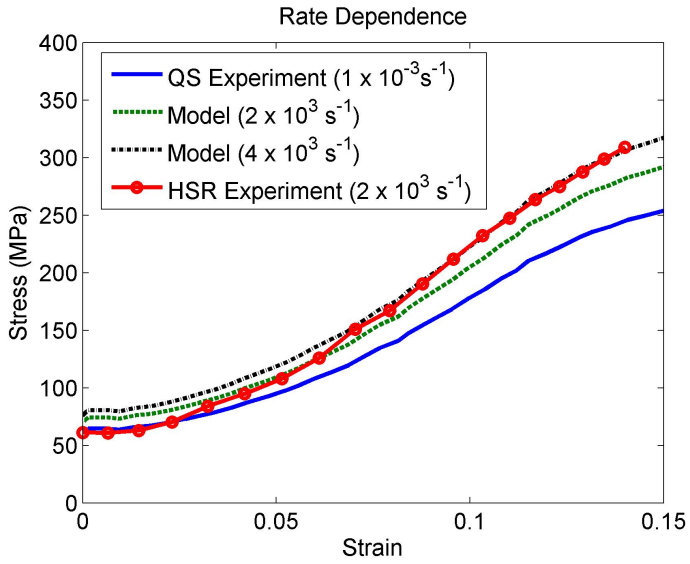

Figure 5.20: Strain rate dependent material behavior obtained using the overstress power law

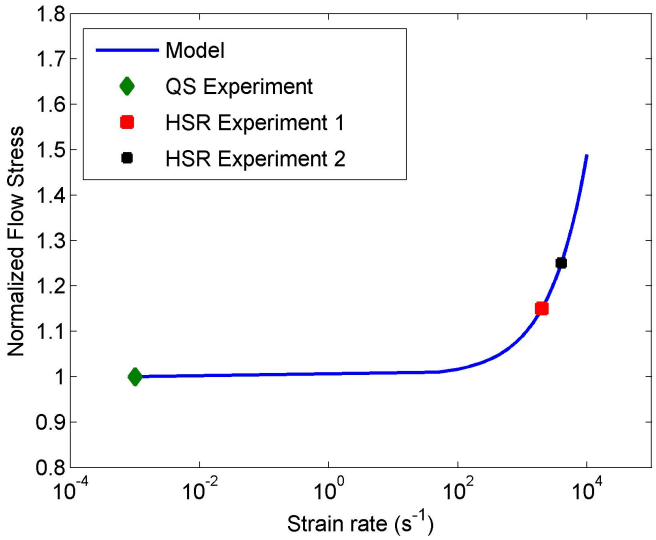

Figure 5.21: The flow stress at various strain rates generated from the overstress power law model (at 5% strain)

The overstress power law rate dependence was implemented in the Abaqus simulations. The results from these simulations are presented here. Fig 5.22a shows the free surface velocity profiles for targets of different thicknesses generated using this power law rate dependent model. The velocity is observed to rise rapidly upon arrival of the elastic wave. A change in slope around 25-30 m/s is calculated here for plates of all thicknesses which appears to correspond to the HEL. The yield strength under quasi-static loading is 60 MPa which is an input to the model. This gives us an expected $\sigma_{HEL} = 130$ MPa (based on $\sigma_{HEL} = \frac{1-\nu}{1-2\nu} Y_0$ [117]). Then the expected free surface velocity that corresponds to this HEL is calculated as $\sim$23 m/s (based on the equation $\sigma_{HEL} = \frac{1}{2}\rho c_{el} v$). Due to the rate dependent model used here, slightly higher free surface velocities resulting in higher HEL are expected for the dynamic loading. This range of velocity values obtained from the simulations is slightly higher than the range (15-20 m/s) observed experimentally. Due the strain rate dependent yield given by the material model used in the simulations, the yield limit is observed to be different for different target thicknesses (higher for smaller thickness). Beyond the first change in slope, the velocity is observed to increase at different rates for different target thicknesses (slower for thicker targets). Another change in slope is observed around 50-55 m/s for all the targets. This change corresponds to the interaction of elastic and plastic waves. In the region close to the rear face, the elastic release wave from the free surface arrives sooner than the loading plastic wave. Their interaction causes the change in slope observed and the velocity gradually rises to a peak value

due to the arrival of the plastic wave at the rear surface. This is also observed in the experimentally measured velocity histories especially for the 7 mm target in Fig 5.6. For the thinnest 2 mm target, the velocity is observed to reach the peak value faster as compared to the thickest 7 mm target. Although the velocity values corresponding to the change of slope and the rates of change of velocities are slightly different in the simulations, the overall nature of the velocity history is similar to the experimental observation (Fig 5.6). Since our intent here is to get an estimate of the stresses, strains and strain rates observed in the experiment and not to obtain the accurate values, this model suffices for the purpose. If we wish to obtain an accurate measure of these quantities, a user defined material model (UMAT) that accounts for the anisotropy, strain hardening and strain rate dependence of the material will be necessary.

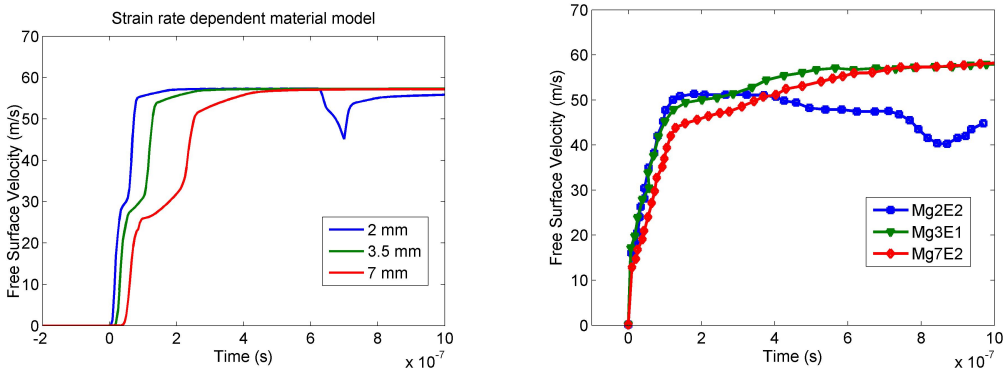

(a) (b)

Figure 5.22: Free surface velocity time history for different target thicknesses obtained from (a) simulations with the rate dependent material model and (b) experimental measurements

A comparison of the computed von-Mises stress history at 1 mm from the impact face is shown in Fig 5.23 a for different target thicknesses. The history of the normal stresses σ_{11} and σ_{22} at the same location is also shown. Note that the magnitude of the normal stresses is quite high ($\sim$300 MPa) compared to the yield strength in uniaxial compression (60 MPa) of the material. Due to the uniaxial strain constraint, plastic flow occurs when the equivalent stress (von-Mises) reaches the uniaxial stress yield limit. The stresses rise above the initial yield limit upon arrival of the elastic wave at this location and plastic flow occurs. The material remains under a high stress until the reflected elastic wave unloads the stress (at $\sim$0.5 μs for the 2mm target - blue curve). The stress rises again due to the reflected plastic wave from the rear free surface and causes increase in the plastic strain. Similar behavior is observed

for the 3.5 mm and 7 mm targets.

The corresponding equivalent plastic strain history is shown in Fig 5.24. The variable PEEQ represents the equivalent plastic strain and its magnitude is given as PEEQ $= \sqrt{\frac{2}{3}\epsilon^p : \epsilon^p}$. There is a sharp rise in the plastic strain at this time at which stress exceeds the yield limit (or the arrival of the plastic wave) for all the plate thicknesses (@ 1 mm from the impact face) (Fig 5.24). The plastic strain increases very slowly until the reflected plastic wave from the free surface causes the stress at this location to increase beyond the yield limit. Another sharp rise in the plastic strain is observed then. The peak values of the equivalent plastic strain reached for different thicknesses are slightly different. This difference most likely arises due to the dependence of the flow stress on the strain rate and the duration of the deformation.

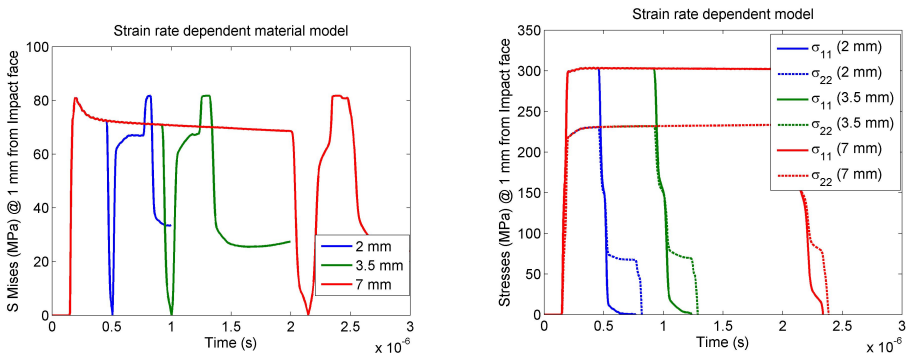

(a) (b)

Figure 5.23: (a) Von Mises stress time history and the (b) longitudinal and lateral stress time histories at 1 mm from the impact surface

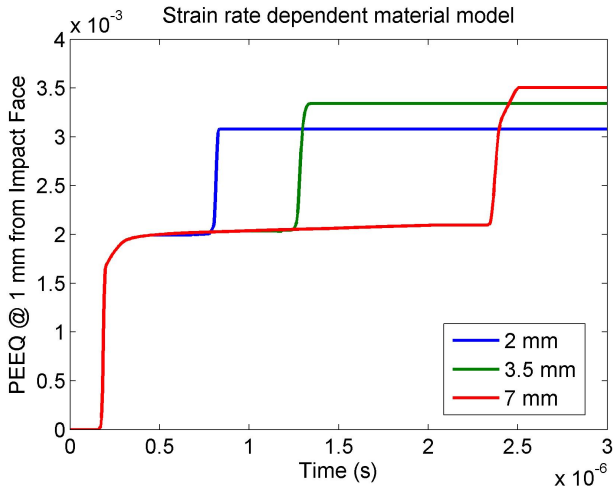

Figure 5.24: Equivalent plastic strain time history at 1 mm from the impact surface

The evolution of plastic strain through the thickness for different target plates is shown in Fig A13a. For all the target thicknesses, the accumulated equivalent plastic strain is the highest at a location close (within ∼0.5 - 1 mm) to the impact face. The accumulated plastic strain decreases towards the free surface reducing to zero at the free surface. Therefore, we can see that the plastic strain is accumulated in an inhomogeneous way through the target thickness.

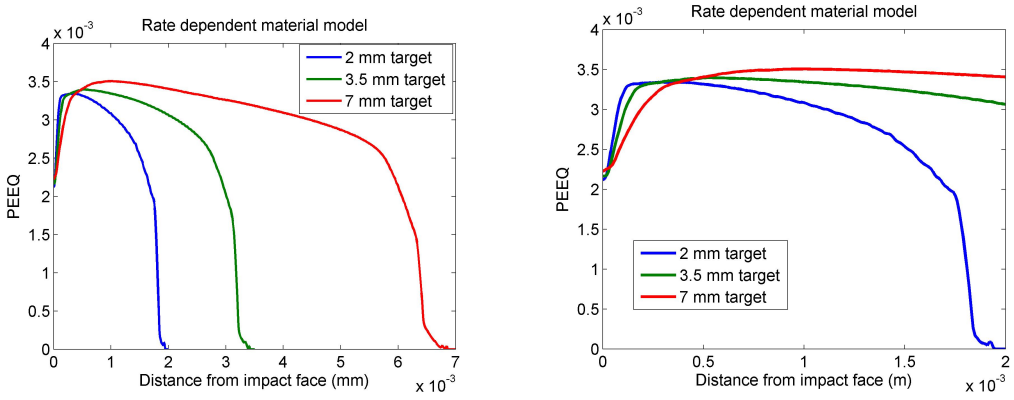

(a) (b)

Figure 5.25: Accumulated equivalent plastic strain distribution through targets of various thicknesses calculated with a rate dependent model plotted (a) over distance from the impact face (b) along the first 2 mm from the impact face

The accumulated equivalent plastic strain in the region 2 mm from the impact face for targets of all thicknesses is shown in Fig A13b for comparison. It can be observed that the distribution of the accumulated plastic strain varies for different targets. The value of the accumulated plastic strain rises to a peak value closer to the impact face for the 2 mm target (blue line) as compared to the thicker targets (green and red lines). The peak plastic strain is observed to be around 0.2 mm from the impact face for the 2 mm target. The plastic strain reduces with distance from the impact face beyond the peak value and is zero at the target rear surface. The strain rate history within the 2 mm target is shown in Fig 5.26 for different locations within the target. It can be observed from the figures that the strain rate jumps correspond to the times

at which the plastic wave arrives at the location - in each case, once from the initial plastic wave propagation and second from the reflected plastic wave from the target rear surface. The magnitude of the strain rate experienced at different locations is highest at the impact face and decreases as we get closer to the rear surface. The magnitude of the strain rate associated with the plastic wave decays with propagation distance. The strain rate imposed due to the reflected plastic wave at a location is lower than that imposed due to the initial plastic wave at the same location.

In Figure 5.27, the strain rate history at a fixed location (1 mm from the impact face) is shown for targets of different thicknesses. The figure shows that the magnitude of the plastic strain rate imposed by the first plastic wave is the same at this location for all targets. The magnitude of the strain rate imposed by the reflected plastic wave (from the target rear surface) is different for different target thicknesses. The magnitude is the highest for the thinnest target (2 mm) and the lowest for the thickest target (7 mm). Therefore, the computed average strain rate at this location due to the two plastic waves is highest for the 2 mm target and lowest for the 7 mm target.

To summarize, the plate impact simulations performed in Abaqus/Explicit show that the stress, strain and strain rates evolve non-uniformly through the target thickness. A comparison between targets of different thicknesses suggests that the average strain rate at a given location is highest for the 2 mm sample and lowest for the 7 mm sample. The overall nature of the free surface velocity histories calculated from the simulations agree with the experimental measurements. The exact values do not

match which is expected due to the assumed simplified dependence on strain rate in the simulations.

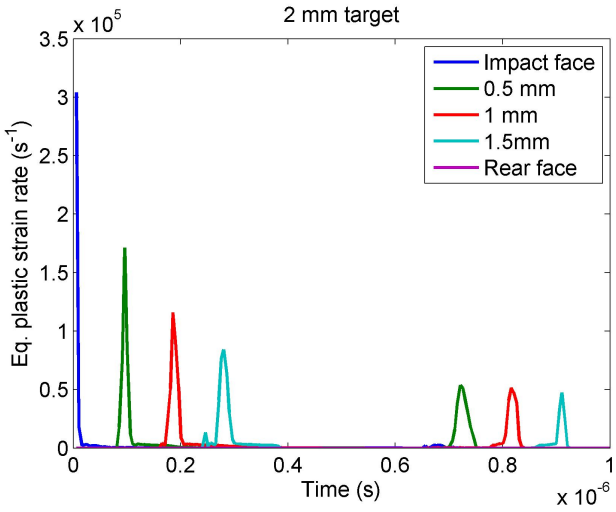

Figure 5.26: Strain rate history at various locations in the 2 mm target (from Abaqus/Explicit simulations)

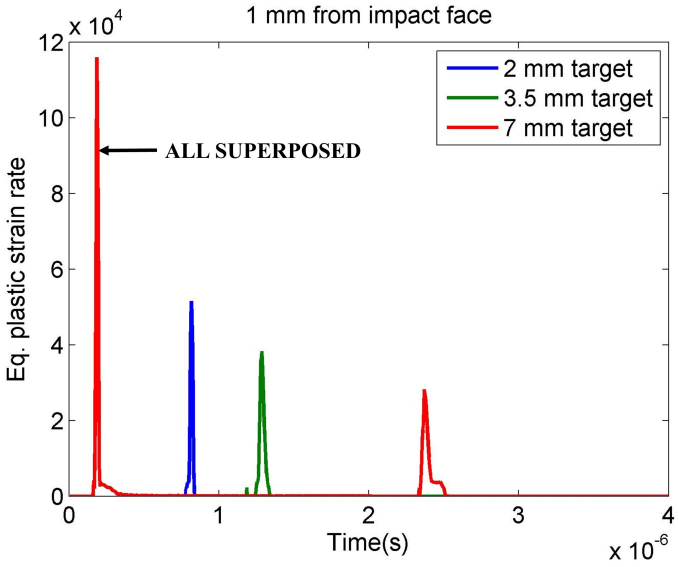

Figure 5.27: Equivalent plastic strain time history at 1 mm from the impact surface (from Abaqus/Explicit simulations)

5.4 Comparison with results from Kolsky bar experiments

In this section, we compare the characteristics of the deformation twins induced by the Kolsky bar loading with those induced by the normal plate impact loading. The morphology of the twins induced by the high strain rate deformation in the Kolsky bars (Chapter 3) appears to be significantly different from the morphology of the twins induced under the normal plate impact loading (Section 6.3). The possible reasons for these differences are explored here.

The loading conditions that are imposed on the material under the Kolsky bar and impact experiments are listed in Table 5.4. Note that in both the experiments, the material was loaded in the extrusion direction. Therefore, the texture of the material with respect to the loading is the same in both cases. The texture is such that the c-axes in most grains are oriented in a plane perpendicular to the ED/loading direction. Therefore, the compression or the impact load applied in the ED imposes an indirect tension along the c-axes of most grains.

Loading conditions	Kolsky bar	Plate Impact
State of stress	Uniaxial stress	Triaxial stress (due to uniaxial strain condition)
Accumulated plastic strain	3.5%	0.35%
Strain rate ($\dot{\epsilon}$)	$10^3 s^{-1}$	10^3-$10^5 s^{-1}$
Time duration	$\sim$200 μs	$\sim$1-2 μs
Time at high $\dot{\epsilon}$	$\sim$150 μs	$\sim$50 ns

Table 5.4: Comparison between the loading conditions under Kolsky bar and normal plate impact loading

However, the stress states in the two experiments are very different. In the uniaxial compression loading imposed by the Kolsky bars, the material is free to expand in the lateral direction to accommodate the plastic deformation. As a result, significant amount of plastic strain can be accommodated in the material. The deformation

typically takes place under a uniform strain rate (of the order of $\sim 10^3 s^{-1}$) across the specimen. After the stresses have been equilibrated, the deformation takes place typically over $\sim 200\mu$s depending on the specimen dimensions and the strain rates imposed.

In the case of the plate impact loading, the deformation is carried in the longitudinal direction. Due to the uniaxial strain condition, the material cannot expand freely in the lateral direction. The stresses in the lateral direction build up as a result. Due to the stresses in the three directions, a much higher stress amplitude is needed to cause severe plastic deformation. As a result, the total strain accumulated in the sample deformed under plate impact loading is small. The typical duration of the plate impact experiment is typically $< 2\mu$s. Therefore, as compared to the Kolsky bar experiments, much less time is available for the deformation (under plate impact loading). The strain rates typically vary through space and time and are typically in the range of $10^3 s^{-1} - 10^5 s^{-1}$, but the rates are large only for times of the order of $\sim$50 ns. Due to these differences in the loading conditions in the plate impact and Kolsky bar loading, the characteristics of the twins induced in these two cases are expected to have significant differences.

Here we compare the stresses and strains that result from the Kolsky bar loading with that from the plate impact loading and relate them to the observed microstructural features. The stress strain response from a high strain rate Kolsky bar experiment is shown in Fig 5.28. The arrow shows the stress and strain at which a

similar test was stopped ($\sim$ 70 MPa, 3.5% strain) to obtain a sample for microstructural analysis (shown in Fig 5.30a). Fig 5.29 shows the Mises equivalent stress (S Mises) and the longitudinal stress (S_{11}) generated in the plate impact experiment as calculated by the Abaqus/Explicit simulation. The longitudinal stress is much higher ($\sim$300 MPa) in the plate impact condition as compared to the stress in the Kolsky bar experiment ($\sim$70 MPa). The von-Mises equivalent stress (70-80 MPa) is comparable to the stress in the Kolsky experiment upto which the specimen shown in Fig 5.30a was loaded. Note that the accumulated plastic strain is significantly different in the two cases. The EBSD inverse pole figure of this specimen is shown in Fig 5.30a. The EBSD inverse pole figure for the material deformed under the normal plate impact loading is shown in Fig 5.30b. If we compare the strain rate in the two cases, the Kolsky bar specimen experiences an average strain rate of $10^3 s^{-1}$ whereas in the plate impact case the strain rate varies locally depending on thickness of the plate. The local strain rate in the case of the 2 mm specimen is $\sim 10^3 - 10^5 s^{-1}$.

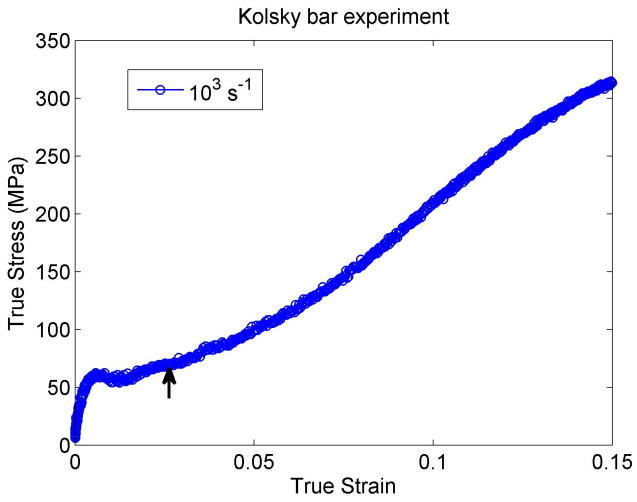

Figure 5.28: Stress vs. strain response from a high strain rate Kolsky bar experiment

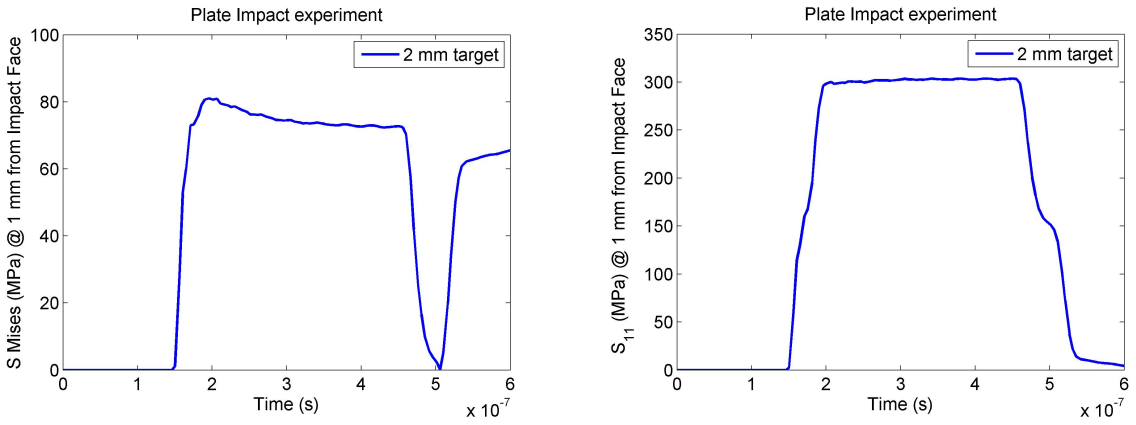

(a) (b)

Figure 5.29: Stresses obtained from the Abaqus simulations of the plate impact experiment (a) S Mises (MPa) (b) Longitudinal stress S_{11} (MPa)

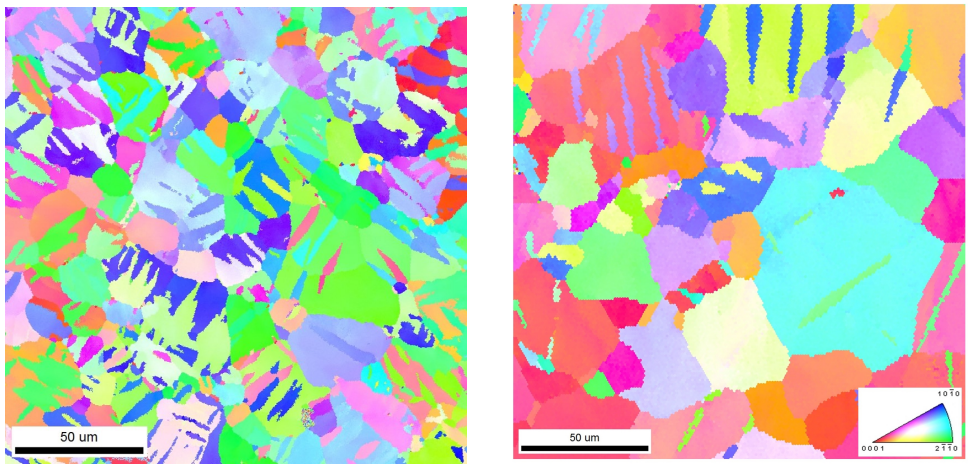

(a) (b)

Figure 5.30: EBSD inverse pole figures of magnesium deformed under (a) High strain rate compression in Kolsky bars (to a strain of ∼3.5% and (b) Normal Plate Impact loading (to a strain of ∼0.35%)

Plastic deformation in magnesium can be accommodated through dislocation slip and deformation twinning (as discussed earlier). Which of these mechanisms dominates depends on several factors such as the nature of loading with respect to the texture of the material, temperature, rate of loading etc.

Let us assume that both slip and twinning are active in the deformation of magnesium under plate impact loading. The increment in total plastic strain can be decomposed into the strain increment due to dislocation slip ($\delta\gamma_d$) and the strain increment due to twinning ($\delta\gamma_t$).

$$\delta\gamma = \delta\gamma_d + \delta\gamma_t \tag{5.17}$$

where the strain due to twinning can be written as

$$\delta\gamma_t = \delta f \hat{\gamma}_t \tag{5.18}$$

where $\hat{\gamma}_t$ is the theoretical twinning shear (0.129 for extension twins in magnesium) and δf is the increment in the twin volume fraction [2]. If w is the average twin width, L is the average twin length and D is the grain diameter, for N number of twins, we have the twin area fraction (considered to be equal to the volume fraction)

$$f = N\frac{wL}{D^2} \tag{5.19}$$

The value of the average twin length (measured in samples deformed under both Kolsky and plate impact) is close to the average grain diameter, and therefore, equation 5.19 can be simplified as

$$f = N\frac{w}{D} \tag{5.20}$$

We refer to N as the average twin number density (i.e. the number of twins per grain). Then the change in the twin volume fraction is

$$\delta f = \delta N\frac{w}{D} + N\frac{\delta w}{D} \tag{5.21}$$

If v_{TB} is the twin boundary velocity, the width of the twin can be written as

$$w = v_{TB}\delta t \tag{5.22}$$

We assume for simplicity that the twin boundary velocity is constant for each twin

variant. Therefore, equation 5.21 can be written as

$$\delta f = \delta N \frac{w}{D} + N \frac{v_{TB} \delta t}{D} \tag{5.23}$$

The first term accounts for a rise in the twin number density due to twin nucleation whereas the second term accounts for the growth of the existing twins.

Equation 5.17 is therefore given as

$$\delta \gamma = \delta \gamma_d + \hat{\gamma_t} [\delta N \frac{w}{D} + N \frac{v_{TB} \delta t}{D}] \tag{5.24}$$

In order to address the differences observed in the twinning characteristics in the plate impact samples as compared to the Kolsky bar samples, we consider four main aspects of twinning: twin volume fraction, twin density, twin morphology and type/nature of twins. The micrographs of the deformed Kolsky bar (3.5% strain) and plate impact targets (2 mm, 3.5 mm and 7 mm) were analyzed to measure the values of the twin volume fraction, average twin density and morphology, which are listed in Table 5.5.

Observation	Kolsky bar	Plate Impact
Twin volume fraction (f_{avg} = 1 - exp[-($\frac{\epsilon}{\kappa}$)^a])	f = 0.162 (measured) (@3.5% strain)	f = 5.6 x 10^{-4} (calculated) (@0.35% strain)
Twin width (w) (μm) Twin length (L) (μm)	w_{avg}=7 (4.7-11.9) L_{avg}=21 (10-34)	$w_{avg} = 4(1.6 - 5.4)$ L_{avg}=21 (10.2-37)
Twin number density (N_{avg})	4.6 (1 - 9)	5 (2 - 11) [2 mm target] 2.8 (1-6) [3.5 mm target] 1.1 (1-2) [7 mm target]
Twin variants	Growth of a single variant	Multiple variants

Table 5.5: Comparison of the twinning characteristics under Kolsky bar and normal plate impact loading

The twin number density is defined as the number of twins per grain. The average twin number density for the sample loaded in the Kolsky bar to 3.5% strain was measured to be 4.6 with a range of (1-9). Note that this value actually may be slightly higher since some of the twins had coalesced with other twins and led to a lower twin count. The twin densities developed in plate impact vary substantially. Table 5.5 shows that the average twin number density for the 2 mm target was estimated to be 5 with a range of (2 - 9) twins per grain. This value is similar to the Kolsky bar specimen with 3.5% strain. The twin number densities for the thicker targets are lower (2.8 and 1.1 for the 3.5 mm and 7 mm targets respectively).

Twin nucleation in magnesium has been observed to depend on the local stress

concentrations. The Schmid factors of the twin variants appear to have some influence on which variants are nucleated but is not a dominant factor [41]. Grain boundaries are assumed to be nucleation sites for extension twins in polycrystalline magnesium due to the high stress concentrations produced by the defect structure associated with them. The material in the case of the Kolsky bar and plate impact loading is the same and therefore expected to have a similar grain boundary structure. Therefore, in the loading configurations where twinning is the dominant mechanism, we expect to see similar twin density for the two cases.

In the constitutive model developed in Chapter 4, an empirical formulation for the evolution of the measured twin volume fraction with strain was developed. The twin volume fraction is given as

$$f(\epsilon) = 1 - exp[-(\frac{\epsilon}{\kappa})^a] \tag{5.25}$$

where κ and a are constants and ϵ is the plastic strain.

The twin volume fraction based on this formulation for the sample strained to 3.5% under Kolsky bar loading is $f = 0.162$ (consistent with the experiments from which the fit was derived). The nominal plastic strain in the plate impact loaded samples is very small. It is estimated to be $\sim$0.35% from the Abaqus/Explicit calculations. Assuming the same values for the twin evolution parameters (Eq 5.25) as that for the Kolsky bar loading, (a=2.5 and κ=0.07) , the twin volume fraction in the case of the plate impact loading is calculated to be $f = 5.6 \text{ x } 10^{-4}$. Therefore, we expect to see a very small volume fraction of twins in the samples deformed under plate impact

loading according to the strain based volume fraction evolution. Of course the values of the parameters κ and a may depend on the loading conditions.

Extension twins can accommodate large amount of plastic strain based on the theoretical twinning shear. Using the above values of twin volume fraction, the plastic strain accommodated by twinning is calculated. For the Kolsky bar specimen strained to 3.5%,

$$\gamma_t = f\hat{\gamma}_t = 0.02 \tag{5.26}$$

Therefore, it can be seen that a significant portion ($\sim$57%) of the plastic strain is accommodated through twinning.

For the plate impact sample,

$$\gamma_t = f\hat{\gamma}_t = 7 \times 10^{-5} \tag{5.27}$$

In the plate impact loading, the fraction of the strain ($\sim$2%) accommodated through twinning is very small. For the extremely small value of plastic strain carried by twinning, very infrequent observations of twins in the microstructure is expected. Therefore, significant dislocation activity may occur to accommodate the remainder of the plastic strain. This may be the case in the 7 mm targets where very few twins are observed.

Note that the twin volume fraction formulation given in Eq 5.25 is for deformation under uniaxial stress. Under uniaxial strain conditions, this relationship is expected to be different. The twin volume fraction predicted by this formulation under the

plate impact loading is very small and a higher twin volume fraction is observed in the 2 mm and 3.5 mm targets.

Significant twinning is observed in the center of the target in the 2 mm samples. The apparent volume fraction of twins in the region appears to be much higher ($\sim$10%). This number is based on the regions that are heavily twinned. Our observations suggest that the microstucture of these targets is inhomogeneous, and there are several regions devoid of twins. Therefore, the volume fraction of twins averaged over the entire collection of grains is expected to be much smaller. The reasons for the observed differences in the amount of twinning in the targets of different thicknesses is still unclear.

The twin volume fraction in the plate impact loading can be calculated using the average twin sizes and number density given in Table 5.5. The expression in Eq 5.23 assumes uniformity of deformation in the material. The microsturctural observations indicate that twinning is not uniform and the effect of this inhomogeneity needs to be accounted for. Therefore, the average twin volume fraction is corrected as

$$f = G_t N \frac{v \Delta t}{D} \tag{5.28}$$

where G_t is the number fraction of twinned grains ($G_t = \frac{\text{No. of twinned grains}}{\text{No. of grains}}$).

It is observed from the micrographs of the deformed samples that there are differences in the morphology of the twins in the Kolsky bar sample as compared to the plate impact sample. The average twin width and twin length in the Kolsky bar and plate impact samples were calculated using ImageJ and are listed in Table 5.5. The

average twin length in the two cases is similar but the average twin width is higher in the case of Kolsky bar specimens. Let us consider equation 5.23 and assume that contribution to the twin volume fraction from the nucleation of twins is similar for the two cases (first term). The contribution from the growth of existing twins (given by the second term) is different.

We assume that the twin boundary velocity is constant. The time duration available for the growth of twins is very different for the two cases as seen from Table 5.4. We hypothesize that since much longer times are available for the twins to grow in the case of the Kolsky bar loading, the twins can grow to much larger twin widths, therefore giving rise to a higher volume fraction. The very short durations available for the twins to grow in the case of plate impact experiment is the reason for the low twin volume fraction. The time duration in the Kolsky bar experiments ($\sim$100μs) is much higher than the plate impact experiments ($\sim$1μs). Therefore, for a constant twin boundary velocity, we expect to see twins of larger widths from equation 5.22. The twins observed in the Kolksy bar specimens are larger, but not 100 times larger as suggested by this assumption of constant twin boundary velocity. Therefore, the twin boundary velocity is likely not constant but is dependent on the loading conditions such as strain rate.

The types of twin variants observed in the Kolsky bar loading are also different from the plate impact loading. In the Kolsky bar loaded samples, one twin variant was observed to dominate the deformation process (discussed in detail in Chapter 3). In

the case of plate impact samples, multiple twin variants are observed in many cases (Figures 5.14, 5.16). The reason for this observation is not clear. One hypothesis is that in both cases, multiple twin variants are nucleated but the growth of one twin variant dominates and takes over the other variant. Due to the longer time duration available in the Kolsky bar loading, the growth of a single twin variant may dominate the deformation whereas due to the short time duration available in the plate impact loading, the twins may not grow as much and the different twin variants can be observed. Since the strain in the Kolsky bar sample that was analyzed is much higher that the plate impact sample, we may be unable to observed the different twin variants that may have existed at smaller strains.

5.5 Summary

The main findings from the experimental and computational investigation of the deformation of magnesium under normal plate impact loading are summarized here. Normal plate impact experiments were conducted on extruded magnesium at impact velocities in the range of 60-70 m/s. Deformation twinning was observed under normal plate impact loading of microsecond duration. The extension twins formed under this loading were observed to be thin and contained multiple twin variants in many cases. Double twinning was also observed. The stresses and strains under this loading are inhomogeneous through the thickness of the plates. This leads to inhomogeneity in

the deformation characteristics through the target thickness. There are some regions that are heavily twinned whereas others are devoid of twins.

The effect of plate thickness/pulse duration on deformation twinning was also studied. It was found that the propensity for twinning was highest in the thinnest plate (2 mm) and decreased with increasing plate thickness for similar impact velocities. The reasons for this observation are unclear and further analysis is necessary.

Finite element simulations of the plate impact experiments in Abaqus/explicit show that the stresses, strains and strain rates imposed in this loading are inhomogeneous through the thickness. The strain rates are of the order of $\sim 10^4 - 10^5 s^{-1}$ but the time durations are much shorter $\sim$100 ns.

The morphology of the extension twins formed under the high strain rates imposed over very short durations of time is different that that observed under the Kolsky bar loading of $\sim 10^3 s^{-1}$. The twin volume fraction is observed to be significantly higher in the samples deformed under Kolsky bar loading as compared to the samples deformed under plate impact. The longer time duration available for the growth of twins (in Kolsky) appears to the main reason for the significant differences in the twinning characteristics in the plate impact loading as compared to the Kolsky bars.

An estimate of the lower bound on the twin tip and twin boundary velocity was obtained and the values were found to be of the order of m/s. The twin tip velocity appears to be higher than the twin boundary velocity based on the twin morphology.

This analysis suggests that deformation twinning is activated in magnesium under

triaxial stress states (imposed by the uniaxial strain condition) at high strain rates (of microsecond duration). The volume fraction of twins under this loading are typically low and hence their effect on the overall texture of the material is not significant as compared with the Kolsky bar loading.

In this analysis, the dislocation activity in the material was not studied. It will be useful to study the dislocation structures inside the deformed targets with a TEM analysis. This will enable us to gain insight into the competition between the slip and twinning mechanisms under dynamic loading. The contribution of dislocation slip to the overall plastic strain will enable us to understand the reasons behind the observed microstructural differences in the targets of different thicknesses.

Chapter 6

Twinning in single crystal Mg under impact loading

6.1 Introduction

The recent interest in the increased use of magnesium in engineering applications has triggered the development of significant research into the deformation of this metal and its alloys [61, 119, 120]. The effects of texture, solutes, precipitates, and loading conditions such as temperature, strain rate etc. are being evaluated [55]. However, in order to build a complete understanding of the behavior of this material, it is important to understand the fundamental deformation mechanisms in single crystal pure magnesium and this is our intent here.

Magnesium has a hexagonal close packed (HCP) crystal structure, and the defor-

mation modes of this material consist of both slip and twinning systems. Slip can occur on the basal (0002) plane, prismatic $\{01\bar{1}0\}$ planes and the $\{11\bar{2}2\}$, $\{01\bar{1}1\}$ and $\{10\bar{1}2\}$ pyramidal planes in magnesium [121]. In addition to the slip modes, extension twinning on $\{10\bar{1}2\}$ planes and compression twinning on the $\{10\bar{1}1\}$ and $\{10\bar{1}3\}$ planes is also observed in magnesium [34, 122]. Several experimental studies have been conducted on single crystal magnesium over the last decade. These studies include experiments on bulk single crystals as well as recent experiments on micrometer sized crystals. Occurence of pyramidal $\langle c+a\rangle$ slip under c-axis compression of Mg single crystals was observed by Obara et al. and Kitahara et al. [35,38] and more recently by Syed et al., Xie et al.(in preparation) and Byer et al. [100,123]. Prismatic $\{01\bar{1}0\}$ and pyramidal $\{10\bar{1}1\}$ slip were observed by Reed-Hill and Robertson [124] when single crystal Mg was compressed parallel to the $\langle a\rangle$ axis. Xie et al. observed extension twinning together with $\langle a\rangle$ slip and $\langle c+a\rangle$ slip inside extension twins in single crystal Mg compressed parallel to the basal plane. Under tension parallel to the basal plane, multiple types of contraction twins - $\{30\bar{3}4\}$,$\{10\bar{1}3\}$,$\{10\bar{1}1\}$,$\{01\bar{1}0\}$ etc. were observed by Reed-Hill and Robertson [125] and Yoshinaga et al. [34]. The study by Chapuis and Driver [39] showed that some of these slip and twin systems (such as pyramidal slip, contraction twinning) are temperature dependent whereas the others are not (extension twinning). From these studies, it is apparent that basal slip and extension twinning are the most prevalent modes of deformation in single crystal magnesium under many loading conditions. There is less of an agreement

on the loading conditions under which prismatic and pyramidal slip and contraction twinning are activated.

All of the studies mentioned previously on single crystal magnesium are in the regime of quasi-static loading. It is important to build a fundamental understanding of the deformation of single crystal magnesium under a variety of loading conditions in order to build better physics-based predictive models.

We are interested in the deformation of single crystal magnesium under dynamic loading conditions. To the author's knowledge, only one study has been performed on the dynamic deformation of single crystal magnesium under uniaxial stress [126]. This study investigated the behavior of single crystal magnesium under $\langle c \rangle$ axis compression under Kolsky bar loading. Secondary pyramidal slip was found to be the dominant deformation mechanism under the uniaxial compression loading of $10^3 s^{-1}$. There have been no studies of the dynamic deformation of single crystal magnesium compressed along the $\langle a \rangle$ axis under uniaxial stress to the author's knowledge. This type of loading is observed to activate multiple deformation modes at quasi-static strain rates (Xie et al, in preparation). Recently, shock and spall experiments were also performed on single crystal Mg [127, 128] and some evidence of twinning was observed. Some impact/shock experiments have been conducted on magnesium and its alloys [75,77]. In these studies, the impact velocities were high enough to generate shock in the material. Millett et al. investigated the response of the magnesium alloy AZ61 to shock loading. The shock response and the spall behavior of the mag-

nesium alloy Elektron 675 were studied by Hazell et al. by impacting the material along the extrusion direction and perpendicular to the extrusion direction. In these magnesium alloys, deformation twinning was observed (in the case of Hazell et al.) and hypothesized (in the case of Millett et al.) to occur under shock loading. To the author's knowledge, no experiments on pure magnesium single crystals in the low velocity impact range have been reported.

The deformation of pure polycrystalline extruded magnesium under low velocity impact ($\sim$60 m/s) was studied in Chapter 5 (Section 5.2) and twinning was observed. Here, we are interested in understanding the dynamic deformation mechanisms in single crystal magnesium under normal impact loading along the $\langle a \rangle$ axis. This loading imposes very high strain rates locally (of the order of 10^4 - $10^5 s^{-1}$) under a condition of uniaxial strain. The effects of the triaxial stress state and the interaction of the impact induced waves with the material will enable us to gain insight into the dependence of the deformation mechanisms on the nature of loading. We perform analyses of the post-deformation microstructure using optical microscopy and electron back scattered diffraction (EBSD), and compare this with that seen in the specimens deformed quasi-statically along the same orientation.

6.2 Experiments

Normal plate impact experiments were performed on magnesium single crystals of 99.999% purity. In these experiments, a stationary target plate is impacted by a flyer plate launched by a gas gun at a certain velocity. The single crystal material was purchased from Metal Crystals and Oxides in the form of a cylindrical rod of 25.4 mm diameter. A cylindrical plate of 3.5 mm thickness was machined from it using electrical discharge machining (EDM). This served as the target plate in the experiment. The flyer plate was of the same dimensions as the target and was made out of extruded pure magnesium machined by EDM. The experimental configuration is shown in Fig 6.1. Both the front and rear surfaces of the target and the flyer plates were lapped with a 15μm boron carbide based lapping slurry to ensure flatness. This was followed by careful mechanical polishing of the rear surface of the target to a finish of 1μm or better. The rear surface of the target plate is required to have a mirror-like finish in order to perform interferometric measurement of the free surface velocity.

The single crystal target plate was oriented such that the crystallographic $\langle a \rangle$ direction was along the axis of the cylinder. This was also the direction of impact. The texture of the extruded magnesium flyer was such that most basal planes were aligned in the extrusion direction (ED) which is in the direction of impact. This texture of the flyer plate provides a better configuration to have a close to symmetric impact due to its close match with the single crystal orientation. Therefore, the nature of the

impact loading with respect to the orientation/texture of both the target and flyer plates is such that the $\langle c \rangle$ axis will experience indirect extension from the imposed compression parallel to the basal plane. Extension twinning is a favored deformation mechanism under this loading configuration under uniaxial stress conditions. It is important to note that the plate impact configuration imposes restriction on strain in the lateral direction (due to the uniaxial strain condition in the impact direction), and results in stresses in the lateral direction. Hence, the deformation modes observed here may be significantly different from those observed under uniaxial stress conditions. Since we have a basic understanding of the deformation modes in single crystal Mg compressed in this direction at quasi-static rates (Xie et al., in preparation), the same orientation was chosen to apply the dynamic impact loading. This enables us to understand the effect of the dynamic loading and the triaxial stress state on the dominant deformation mechanisms.

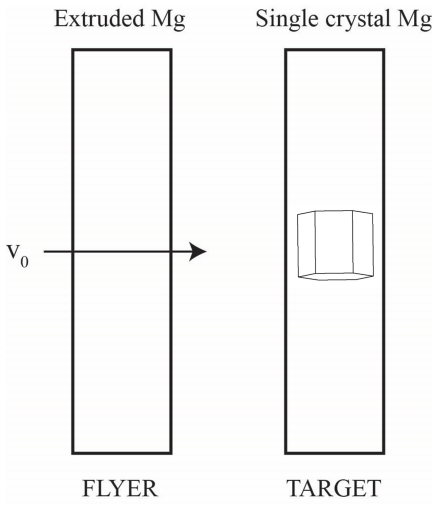

Figure 6.1: Experimental configuration for the normal plate impact experiments conducted on single crystal Mg

The experimental configuration for the normal plate impact experiment is shown in Fig 6.1. Upon impact, longitudinal compressive waves are generated in both the target and the flyer plates. If the impact velocity generates a stress higher that the yield limit of the material, the wavefront decomposes into elastic and plastic waves. The wave propagation in the idealized case of a single elastic and plastic wave is shown in Fig 6.2. Since we are interested in the inelastic deformation of the material, we chose the same impact velocity ($\sim$60 m/s) as used for the polycrystalline case in Chapter 5. The polycrystalline material underwent inelastic deformation under this impact velocity. The normal plate impact recovery setup designed by Jia and Ramesh [79] described in Chapter 2 was used in order to recover the single crystal target plate after impact for microstructural analysis. The recovery setup consists of

a stopper which absorbs the kinetic energy of the projectile after the initial impact.

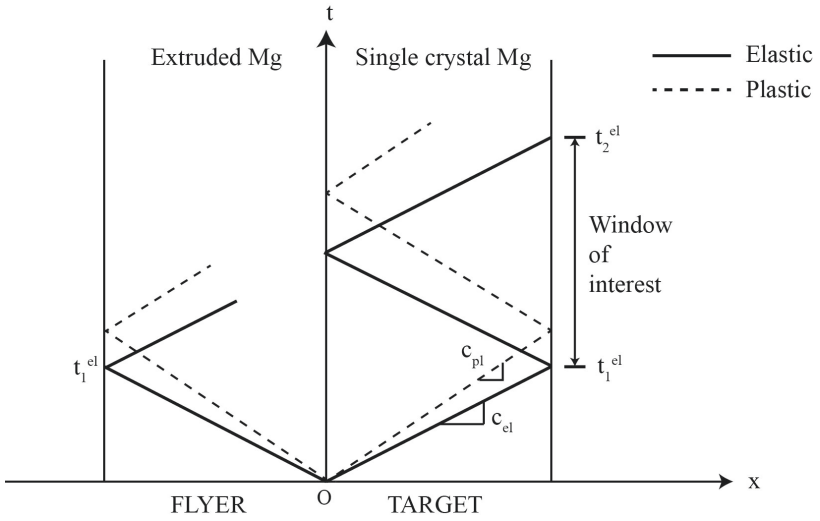

Figure 6.2: x-t diagram showing elastic-plastic wave propagation in the normal plate impact experiment on single crystal Mg

Test ID	Plate thickness (mm)	Projectile Velocity (m/s)	Tilt (milliradians)
Mga1	3.5	55	0.78
Mga2	3.5	58	0.22

Table 6.1: List of normal plate impact recovery experiments on single crystal Mg. Impact was along the $\langle a \rangle$ axis

The projectile velocity prior to impact was measured with a laser line velocity measurement system originally designed by Ramesh and Kelkar [80]. Two experi-

ments were conducted on single crystal Mg with similar impact velocities (Table 6.1). The misalignment between the impact faces of the target and flyer plates was also measured using a tilt circuit. The experimentally measured data for the test with smaller misalignment (Mga2) is presented here (Fig 6.3). A normal displacement interferometer (NDI) was used to measure the particle velocity at the rear surface of the single crystal Mg target. The experimentally measured displacement and velocity history at the target rear surface is shown in Figure 6.3.

Upon impact, longitudinal elastic and plastic waves are generated in the flyer and target plates. The elastic wave travels at a higher speed than the plastic wave ($c_{el} > c_{pl}$). These waves propagate through the thickness of the plates, reach the rear surface which is stress free and are reflected back into the plates. Each plane through the thickness of the plates experiences different stress and strain histories due to the nature of the elastic-plastic wave propagation. The regions closer to the impact face experience the elastic wave first followed by the plastic wave. In the regions close to the rear surface, the elastic wave reflected from the free surface may arrive at a given location earlier than the loading plastic wave depending on the relative wave speeds. Therefore, the stress state and deformation history experienced in different regions varies due to the complex wave interactions especially at longer times. In the regions close to the impact face, the stresses build up rapidly upon impact. These regions remain in this stressed condition until the reflected waves from the free surface arrive. These regions experience high amplitudes of stress for the longest time. In contrast,

the regions closest to the free surface of the target experience the high stresses for the shortest time.

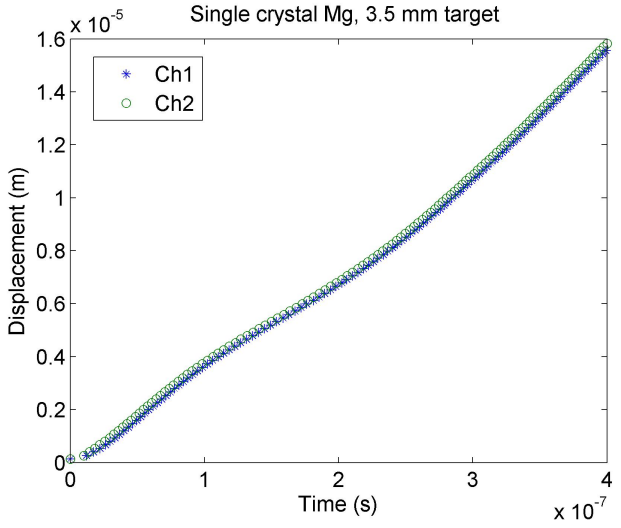

(a)

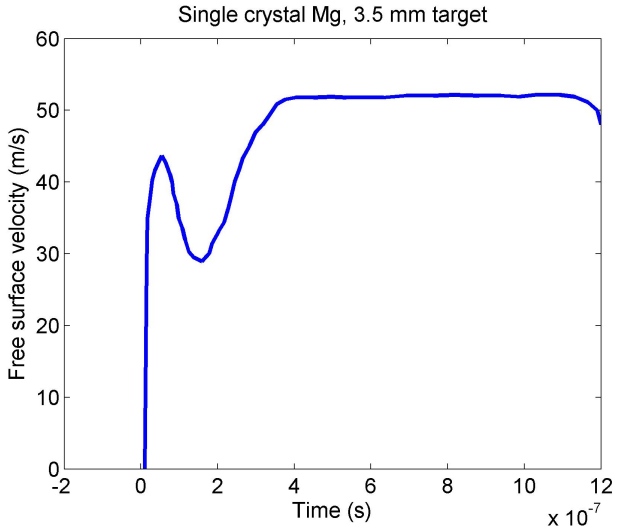

(b)

Figure 6.3: Experimentally measured (a) displacement history and (b) velocity history at the free surface of the single crystal Mg target plate (Mga2) under normal plate impact loading

The free surface displacement and velocity histories (shown in Fig 6.3) have been

shifted such that the elastic wave arrives at the free surface at zero time. The particle velocity at the target rises sharply to ∼43 m/s upon arrival of the elastic wave. Thereafter, a dip in the velocity profile is observed that reduces the velocity to about 30 m/s. The velocity rises again gradually to a value of ∼54 m/s likely due to the arrival of the plastic wave. Since the velocity history is derived from the displacement history, a similar trend is seen in the displacement profile as well. The rate of change of displacement is initially high, decreases slightly thereafter but then finally rises gradually (Fig 6.3a). The free surface velocity history in this case is observed to be significantly different from that in the case of extruded polycrystalline Mg impacted in the ED. In the polycrystalline material, no dip in the velocity was observed after the first sharp rise but a more gradual increase to the peak velocity was observed (Chapter 5).

The shock and spall respone of single crystal magnesium was recently measured by Kanel et al. and Winey et al. [127,128]. Winey et al. performed shock and release experiments along (0001) oriented single crystals. Kanel et al. investigated the shock and spall behavior of crystals impacted along (0001) axis, normal to the (0001) axis and at an angle of 45^0 to it. The HEL was measured to be different in different directions. The free surface velocity profiles measured in these experiements also show the sharp spike associated with the elastic precursor followed by a decay in the amplitude after which the rise in the velocity due to the shock wave is observed. This feature is observed for the (0001) oriented crystal and the $(10\bar{1}0)$ oriented crystal but

not for the crystal oriented 45^0 away from the c-axis [127]. The decay following the elastic precursor is associated with the stress relaxation caused by the multiplication of mobile dislocations or twins [127]. Evidence of profuse twinning was found in the recovered samples from the c-axis oriented crystals by Kanel et al. No microstructural analysis was presented for the crystals impacted normal to the (0001) axis.

The HEL can be calculated based on the measured free surface velocity profile. It is typically associated with the velocity at the first change of slope from the elastic precursor velocity. The longitudinal stress at the elastic precursor front, σ_{HEL}, is given by

$$\sigma_{HEL} = \frac{1}{2}\rho U_e v_{fs} \tag{6.1}$$

where U_e is the propagation velocity of the elastic precursor wave taken to be equal to the longitudinal wave speed c_{el} and v_{fs} is the free surface velocity associated with the elastic precursor. The density ($\rho = 1740$ kg/m^3) is taken from the literature. The longitudinal wave speed is be calculated as

$$c_{el} = \sqrt{\frac{c_{11}}{\rho}} = 5843 m/s \tag{6.2}$$

where $c_{11} = \lambda + 2\mu = 59.4$ GPa at 300^0K. The value of c_{11} is taken from Slutsky et al. [129]. Based on the measured velocity profile, and the above values, the calculated value of the HEL using the elastic constants for pure magnesium comes out to be $\sigma_{HEL} \approx 219$ MPa. This value of HEL is in the range of the HEL values reported for magnesium alloys [75, 77].

In our work, the loading direction is normal to the (0001) direction of the crystal. The free surface velocity profile is therefore expected to be similar to that of the $(10\bar{1}0)$ loaded crystal from Kanel's work. The measured free surface velocity shows similar features of the spiked elastic precursor followed by the precursor decay and then a separate plastic wave, although the amplitude of the plastic wave is much smaller because of the low impact velocities in this work. A decay in the elastic precursor with increasing distance of propagation is also observed [127]. σ_{HEL} of ∼390 MPa was reported for a 2 mm sample by Kanel et al. The HEL value calculated in this work is lower but is expected assuming the decay of the elastic precursor with propagation distance given that the thickness of the target in our work was 3.5 mm.

Some of the recent works reported the experimentally measured values of the Hugoniot elastic limit (HEL) (i.e. the yield stress under uniaxial strain condition) of some magnesium alloys. For AZ61, the HEL was found to be 205 MPa by Millet et al. [75]. Hazell et al. measured the shock and spall response of a magnesium alloy Elektron 675. The HEL was measured to be ∼380 MPa [77].

The velocity history profile here is also similar in nature to the velocity history profiles generated under shock loading of different materials in which elastic precursor decay is observed. Johnson and Rhode investigated dynamic deformation twinning in iron under shock loading [130]. Their observations indicate that the stress relaxation behind the elastic precursor is associated with twin formation. Impact experiments were performed by Kanel et al. on aluminum single crystals [117]. The free surface

velocity history in their experiments also showed decay behind the elastic precursor. The decay/relaxation observed in the velocity profiles is typically associated with generation or motion of defects such as dislocations and twins which is likely to be the case here.

6.3 Microstructural Analysis

6.3.1 Optical microscopy

The single crystal Mg target plates were recovered after impact and sectioned by EDM to obtain specimens for microstructural analysis. The specimens were then carefully mechanically polished down to a finish of 5μm (1200 grit) with SiC paper and water. Care was taken to ensure that $\sim$300 μm thick layer of material was removed in order to get rid of any damaged material from the EDM process. Mechanical polishing was followed by chemical etching of the surface with a solution containing 10% nitric acid in distilled water. The etchant attacks the high energy sites in the material therefore exposing twin boundaries and dislocation rich regions. The optical micrographs of the deformed material are shown in Fig 6.4(a,b). The optical micrographs are oriented such that the impact face is towards the left side of the image and the free surface is towards the right side. Three main geometries of twins are observed in the microstructure. First was the several long and thin twins that lie horizontally in the image (i.e. perpendicular to the impact and rear faces) are observed in the

microstructure. The second is the twins that have traces at an angle to the impact face and intersect the long horizontal twins. The third is the several small twins that are observed to form at intersections of larger twins or are observed to branch off larger twins. Several twin intersections are also observed. These twins are oriented along specific crystallographic planes. The orientation information about these twins is necessary to determine if the nature of these twins and the twin variants.

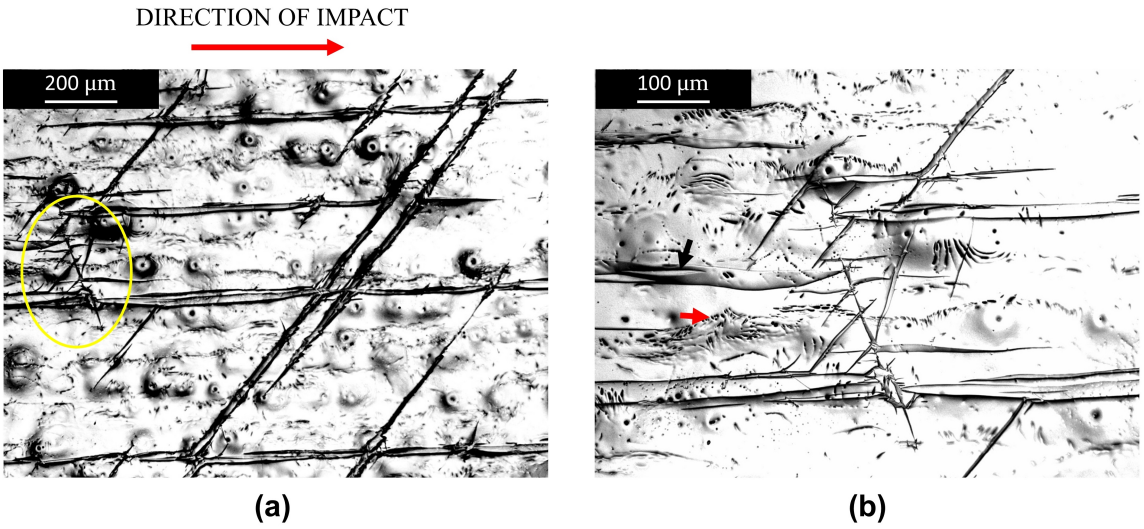

Figure 6.4: Optical micrographs of the deformed single crystal Mg target are shown in (a) and (b). Impact face is towards the left side of the image and the rear surface is towards the right side.

Complex twin structures are also observed in many places such as the one shown in the right image in Fig 6.4b. In some cases, twins formed inside another twin are observed and an example can be seen in the figure (shown by the black arrow). These

features are difficult to resolve with the optical microscope due to the limitation on the resolution and the surface topology. The other etch mark type features (shown by the red arrow) observed in the micrographs are most likely due to the underlying dislocation structure. These features were also observed in the quasi-static compression study of single crystal Mg performed by Xie et al. (in preparation).

The optical images were analyzed with a commercial software ImageJ in order to obtain an estimate of the twin sizes and twin spacing. The terminology used for some of the microstructural features observed here is shown in Fig 6.5. The average horizontal and vertical spacing between the larger twins (D and H respectively) was measured. The average width W (of the big twins) and the average twin lengths of the two larger groups of twins (L_{horz},L_{ang}) was also measured. The width and length of the smaller twins was not measured due to the limitation of the resolution of the images. The average measurements are reported in Table 6.2. These measurements are useful when constructing physics based constitutive relationships involving defect sizes and spacing and their effects on the deformation.

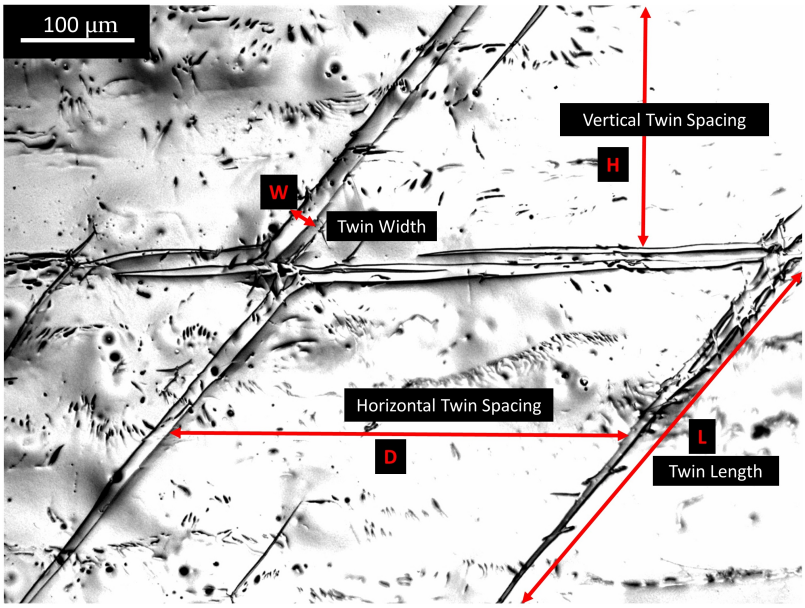

Figure 6.5: Optical micrograph of deformed single crystal Mg. The important features and the terminology are marked

The average twin sizes observed in the single crystal Mg deformed under impact loading are compared with those observed in the polycrystalline Mg in Chapter 5. In the single crystal material, the twins formed are much longer as compared to the ones formed in polycrystalline Mg under similar loading. In the polycrystalline Mg, the maximum twin length was limited by the grain size (~ 20 μm). In the polycrystalline material, grain boundaries are believed to be nucleation sites for twins due to the defects associated with them. The grain boundaries are high energy sites and therefore also act as barriers to the motion of defects such as twins. In the case of single crystal

Twin length (large horizontal twins) (L_{horz}) (μm)	2122 [1013-2653]
Twin length (angled twins) (L_{ang}) (μm)	866 [505-1307]
Twin width (W) (μm)	19 [12-22]
Vertical twin spacing (H) (μm)	267 [208-377]
Horizontal twin spacing (D) (μm)	345 [46-544]

Table 6.2: Nominal twin sizes and spacing (and the ranges) in deformed single crystal Mg

Mg, there are no grain boundaries to act as nucleation sites or barriers for the motion of defects. The free surfaces are most likely the nucleation sites in this case. The free surfaces typically have a defect population due to specimen preparation, handling etc. Therefore, it appears that grain boundaries play an important role in determining the morphology of deformation twins. Small twins are also observed in the middle of the target (Fig 6.4). It appears that they may have formed due to the interaction of the larger twins.

Under the plate impact loading, there is likely to be dislocation activity in the single crystal material along with deformation twinning. A comparative study of the dislocation structure observed in this case with that in the polycrystalline case will be helpful. TEM analysis of the deformed specimens is planned in order to study the dislocation structures in the material.

6.3.2 EBSD analysis

In order to understand the types of twins and the crystallographic orientation of the twins with respect to the parent, EBSD analysis was performed on the specimens. The specimens were mechanically polished first and then electrochemical polishing was performed in a LectroPol-5 electropolisher. The electropolishing was performed with a 5% nitric acid in methanol electrolyte at 0^0C and a voltage of 20V.

The inverse pole figure (IPF) map of the deformed single crystal Mg target is shown in Fig 6.6. Different crystallographic orientations are represented according to the IPF color map key shown in the inset. The sample is oriented similar to that in the optical micrographs with the impact direction horizontal in the plane of the figure. It can be observed from the figure that the parent region (red) is oriented such that the crystallographic $\langle c \rangle$ axis is almost normal to the plane of the image. Three types of twins, T1, T2 and T3 shown by the dark blue, light blue and light green colors respectively are identified. The orientation of each of these twins and the parent region are shown by the wire-frame drawings in the images on the right side. The misorientation profiles across the twins are measured along Line 1 and Line 2 that cross multiple twins as marked in Fig 6.6. These measured misorientation profiles shown in Fig 6.7 enable us to identify the types of twins.

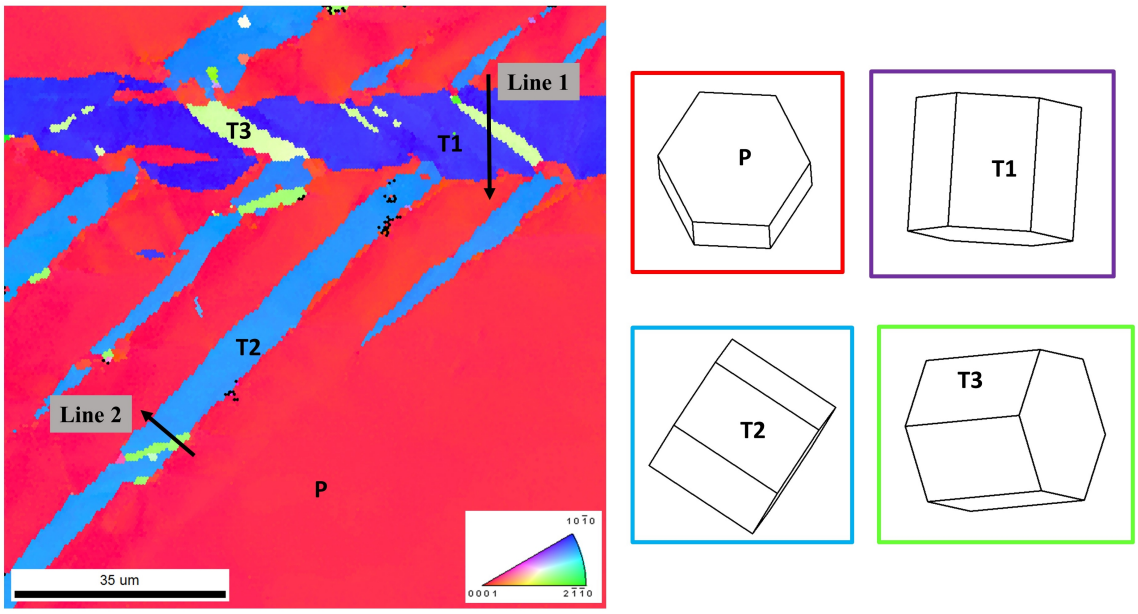

Figure 6.6: Inverse pole figure measured by EBSD of the single crystal Mg deformed under normal plate impact loading

The misorientation profile across Line 1 is shown in Fig 6.7a. The blue lines in the figure represent the point-to-point misorientation whereas the green lines represents the point-to-origin misorientation. Line 1 starts from the parent region, first crosses twin T1, then twin T3 and back into twin T1 to finally end in the parent region. It is observed from the profile that the dark blue twin (T1) is an extension twin and is 86^0 degree away from the orientation of the parent region. There is an 86^0 change in the point-to-point misorientation associated with the twin boundary between T1 and T3. Therefore, it appears that twin T3 is an extension twin with respect to the twin T1. The orientation of twin T3 is $\sim 60^0$ away from the parent (as seen from the point-to-origin profile) and therefore it is not an extension twin with respect to the

parent region.

Fig 6.7b shows the misorientation profile across Line 2. We can observe that the light green twin (T3) is oriented $\sim 60^0$ away from the orientation of the parent region which is similar to the observation along Line 1. The light blue twin (T2) is an extension twin which is oriented $\sim 86^0$ away from the parent.

In order to compare the relative orientations of the twins with respect to the parent, a pole figure type plot in the (0001) direction is shown in Fig 6.8. It can be observed that the orientation of the (0001) pole in the parent shown by the red dot (P) is very close to the out of plane direction at the center of the figure. Twins T1 (dark blue) and T2 (light blue) are oriented in such a way that the (0001) poles are 86^0 away from the (0001) pole of the parent region. The twin T3 (light green) has the (0001) pole oriented $\sim 60^0$ away from the parent (P).

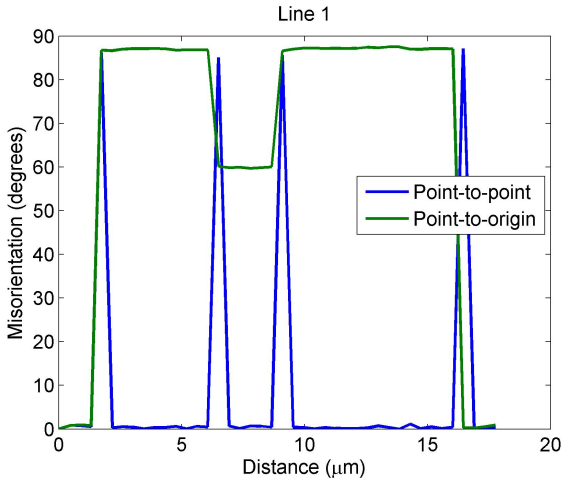

(a)

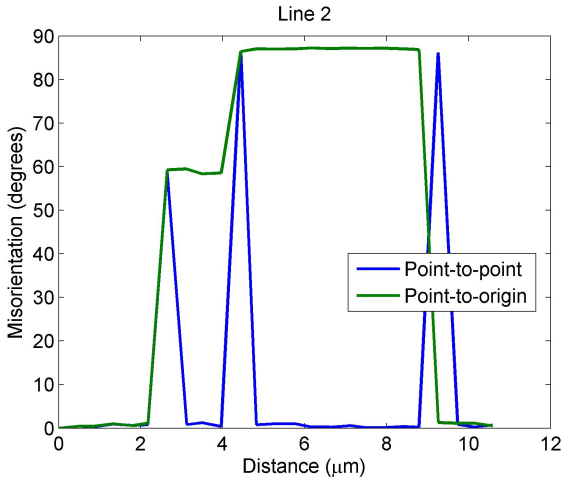

(b)

Figure 6.7: Point-to-point and point-to-origin misorientation profiles plotted accross (a) Line 1 and (b) Line 2 in figure 6.6

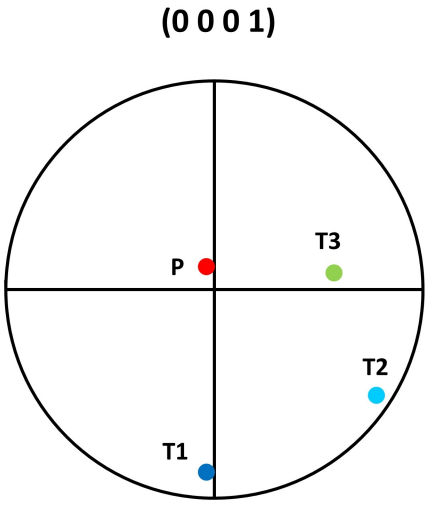

Figure 6.8: (0001) pole figure showing the parent and twin orientations for the IPF map shown in Fig 6.6

The twins T1 and T2 have a misorientation of 86^0 with respect to the orientation of the parent region and therefore are extension twins. The in-plane orientations of these twins are 60^0 apart which suggests that they are different extension twin variants. The twins T1 and T2 are two of the standard extension twin variants observed in several studies on Mg and its alloys [1, 25, 83].

The twin T3 appears to be a secondary extension twin. The exact mechanism for the formation of this twin is unclear. It is speculated that the twins T1 and T2 are formed under the initial propagation of the plastic wave from the impact. When this wave is reflected from the free surface of the target, it may cause secondary twinning inside the existing twins resulting in twins such as T3. To the author's knowledge, this type of secondary extension twinning has not been reported in magnesium thus

far. In the current experimental configuration, we are unable to differentiate between the deformation induced by the loading plastic wave and the reflected plastic wave. Experiments may be conducted in the future where a single wave travels through the target plate. This can be achieved by using a momentum trap plate backing the target plate. This will provide a cleaner loading of the sample.

Experiments on AZ31 were performed by Wu et al. [76] using the Kolsky bars. Observations of extension twins with different variants and double twinning were made in the deformed samples. It is important to note that the state of stress is different in the Kolsky bar loading as compared to the plate impact. From our previous studies (Chapter 3 and 5), we have observed that the uniaxial strain state in the plate impact loading and the higher strain rates as compared to deformation under Kolsky bar loading of uniaxial stress produces different twinning characteristics. The only other studies of the microstucture of a magnesium material after impact/shock loading to the author's knowledge were by Hazell et al. [77] and Kanel et al. [127]. Extensive twinning was observed by Hazell in the polycrystalline F grade Elektron 675 alloy shocked to 3.4 GPa. Since only optical microscopy was performed on the deformed samples, information about the type of twins, variants etc. is not known. Similar is the case for Kanel's experiments on (0001) oriented single crystal Mg in which profuse twinning was observed in the shocked samples with optical microscopy. A detailed crystallographic study of the deformation twins induced in magnesium under impact has not yet been performed to the author's knowledge.

6.4 Summary and future work

Deformation of single crystal magnesium impacted along the $\langle a \rangle$ at low velocities (55 - 60 m/s) axis was studied. A distinct elastic-plastic wave propagation was observed. The free surface velocity showed a decay of the elastic precursor typically associated with multiplication of mobile dislocations or twins. The HEL based on the measured free surface velocity was calculated to be $\sim$219 MPa which is in the range of the measured values for magnesium and its alloys under shock/impact loading.

Microstructural analysis was performed on the impacted samples and extension twinning was observed to be a dominant deformation mechanism. The average sizes of twins observed here were much larger as compared to the twin sizes measured in polycrystalline magnesium in Chapter 5. It is therefore suggested that grain boundaries act as strong obstacles to the growth of twins and thus play an important role in the growth of twins.

Three types of twins were observed in the microstructure. Two of the observed dominant twins (T1 and T2) correspond to the commonly observed extension twin variants in magnesium. A secondary extension twin (T3) was observed to form inside the primary extension twins (T1 and T2). The mechanism behind the formation of this twin is unclear and further analysis is necessary. The activity of dislocation mechanisms under this loading has not been studied. Therefore, TEM analysis to investigate the dislocation structures in the material is also planned.

Normal impact experiments at different stresses i.e. at varying impact velocities

can be conducted in the future. This will enable us to build an understanding of the dependence of twin nucleation on the stress amplitude. Experiments conducted with different pulse durations at the same impact velocity can help us understand the dependence of twin growth on the pulse duration versus stress amplitude.

The dynamic deformation of single crystal Mg under impact along $\langle c \rangle$ axis is also of interest. In loading configurations of this nature at quasi-static strain rates, pyramidal $\langle c + a \rangle$ slip and contraction twinning are the dominant modes of deformation. The deformation modes activated under dynamic impact in this orientation remain to be studied.

Chapter 7

Summary and future work

7.1 Summary of work and concluding remarks

Magnesium is gaining increasing importance in automotive, aerospace and defense applications. Most of the studies on magnesium till date have focused on the deformation of magnesium alloys in the low strain rate regime. However, a fundamental understanding of the dynamic behavior of this material is important given the potential automotive, aerospace and defense applications. The goal of this thesis was to improve our overall understanding of the dynamic behavior of magnesium with

a focus on understanding the relationships between deformation mechanisms (slip and twinning) and mechanical behavior. This was achieved through experimental characterization under dynamic loading, microstructural analysis and analytical and finite element modeling of poycrystalline and single crystal magnesium. The main contributions of this work are summarized here.

The majority of this work was focused on understanding the behavior of extruded polycrystalline pure magnesium. This material was chosen due to its strong texture in the extrusion direction (ED). Texture plays an important role in the deformation of magnesium and alloys as observed in previous studies [50, 59]. All the experiments presented here were conducted in compression along the ED as most of the grains have similar orientations with respect to the ED in this material and are expected to undergo similar deformation. This enables us to understand the overall response of the material based on a limited number of microstructural observations due to the low specimen to specimen variability.

7.1.1 Behavior of magnesium under high strain rate uniaxial stress loading

The behavior of magnesium under compression in the ED at quasi-static ($10^{-3}s^{-1}$) and dynamic ($10^{3}s^{-1}$) strain rates is presented in Chapter 3. The work shows that the mechanisms of extension twinning, $\langle a \rangle$ slip and $\langle c + a \rangle$ slip are necessary to

accommodate plastic strains under high strain rate loading along the ED in pure magnesium of micrometer size grains. The microstructural observations show that extension twinning reorients the material ($\sim 86^0$) to a harder orientation and causes a significant change in the texture. The previous works on the dynamic behavior of Mg alloys have only considered the evolution of twins in magnesium alloys and have not focused on the dislocation activity [50, 60]. To the authors knowledge, this work presents the first observations of the evolution of $\langle c+a \rangle$ dislocations inside extension twins in magnesium under dynamic loading. The extension twinning process is observed to be dominated by the growth of twins from the same variant pair. The interactions of the pyramidal $\langle c+a \rangle$ dislocations are observed to result in the formation of dislocation cells and subgrains which act as obstacles to the motion of other dislocations (Fig 3.13a,b). These observations suggest that the texture hardening due to the reorientation associated with extension twinning and the hardening caused by the interactions of the $\langle c+a \rangle$ dislocations both contribute to the high degree of strain hardening in the material. Although contraction twins are sometimes speculated to be the reason for the high strain hardening rates in Mg alloys [50], no evidence of contraction twinning was observed until the strains associated with the peak strain hardening rates.

This work suggests that although extension twinning is the dominant mechanism at low strains under compression in the ED, pyramidal $\langle c+a \rangle$ slip becomes increasingly important at higher strains under sustained high rate deformation. These ob-

servations enable us to develop a more complete understanding of the microstructural evolution of this material during the uniaxial stress dynamic deformation of the order of $\sim$200 μs.

7.1.2 Constitutive modeling

The insights gained from the analysis of the evolution of the dominant deformation mechanisms under compression in the ED were used to develop a simple mechanism based constitutive model presented in Chapter 4. This scalar model is based on an internal state variable formulation. The evolution equations for extension twinning, $\langle a \rangle$ slip in the parent and $\langle c + a \rangle$ slip inside the twinned region are formulated to capture the behavior of polycrystalline magnesium under compression in the ED. An empirical formulation for the evolution of twin volume fraction is considered whereas the evolution of dislocation density is physics based. This model is able to capture the experimentally observed behavior of extruded magnesium when compressed in the ED at quasi-static and dynamic strain rates.

A model for the behavior of single crystal Mg under $\langle c \rangle$ axis compression is also developed. $\langle c+a \rangle$ dislocation slip is the only dominant mechanism observed under this loading and therefore a simple analytical solution can be formulated. This formulation is able to capture the experimentally observed behavior well. This study shows that the complex response of magnesium can be captured by a simple mechanism based model.

7.1.3 Behavior of magnesium under dynamic loading of uniaxial strain

In Chapter 5, the analysis of the dynamic deformation of extruded magnesium under normal impact at 60 - 70 m/s is presented. The plastic strain accumulated under the normal impact loading is very low ($\leq$0.35%) due to the triaxial stress state imposed by the uniaxial strain condition. The observations from this work indicate that extension twinning occurs in magnesium even under the very short duration ($\sim$1 μs) of loading. The uniaxial strain condition (in the impact direction) in the plate impact configurations places a constraint on the strains in the lateral direction. Therefore, differences are expected in the twinning characteristics in this case as compared to the uniaxial stress Kolsky bar loading. Here, extension twinning does not occur uniformly in the microstructure with some regions showing extensive twinning and other regions devoid of twins. Variation in the amount of twinning is also observed between targets of different thickness but the reasons are still unclear. Elastic-plastic finite element simulations performed in Abaqus/Explicit show that the stress, strain and strain rate are non uniform though the thickness of the plate and evolve during the loading due to the wave propagation. This distribution along with the competition with dislocation slip is speculated to be the reason for the variation in twinning observed in the microstructure.

The average twin tip and twin boundary velocities were estimated from the mea-

sured twin sizes and found to be greater than a few m/s. The estimated values provide a lower bound on the velocities due to the post-mortem observation of the twins formed under the loading. Observations of twins in other materials have suggested that the velocities of twins formed under shock loading could approach the shear wave velocity [131].

7.1.4 Comparison of twinning under Kolsky bar and plate impact loading

The twins formed under the plate impact loading are generally observed to be thinner (and the overall volume fraction lower) compared to those observed under Kolsky bar loading. The twin number density appears to be similar in both cases. The main implications of these observations are presented here. Twin nucleation (and the twin number density) depends upon the local stress concentrations provided by the grain boundary defects (in polycrystalline materials) and does not appear to be affected by the duration of the loading. The twin volume fraction which directly depends on the twin density and the twin sizes appears to be dominated by the contribution from the twin size. The twin morphology (especially the twin width) depends upon the duration of loading. It is suggested that motion of the twin boundary causes an increase in the width of individual twins and therefore increases the overall twin volume fraction as given by the equation $w = v_{TB}\Delta t$. Therefore, for a constant twin

boundary velocity, twins of larger widths are expected for longer time duration of deformation as are observed in the case of Kolsky bar loading.

These observations imply that twinning occurs even under dynamic loading of very short time durations. It is important to note that although twinning may occur under such loading conditions, the volume fraction of twins is expected to be small. Therefore, the change in the overall texture of the material due to twinning is expected to be small as well. On the contrary, under sustained dynamic loading of longer durations (as in the case of Kolsky bars), the twins are expected to grow and cause a significant change in the overall texture of the material.

Multiple twin variants (and double twins) are observed in many cases under the microsecond impact loading. This is different from the observation of the same twin variant pair in the Kolsky bar loading. It is hypothesized that twinning involves nucleation of multiple variants but the growth of a single twin variant pair dominates the twinning process to accommodate large plastic strain.

7.1.5 Dynamic behavior of single crystal magnesium

In chapter 6, the analysis of the response of single crystal magnesium under normal impact of microsecond duration along the $\langle a \rangle$ axis is presented. Extension twinning is found to be an important deformation mechanism. The sizes of the extension

twins formed are much larger compared to the ones observed in the polycrystalline material deformed under similar loading conditions. This observation suggests that grain boundaries act as strong barriers to the growth of extension twins. In the single crystal, twins can grow much longer and wider due to the absence of grain boundaries. The crystallographic analysis of twins suggested that twins of three different variants are formed under this loading. The most dominant twin variant is not observed to correspond with the variant with the highest Schmid factor as has been observed in a few other quasi-static studies [41, 42].

7.2 Suggestions for future work

This work was aimed at furthering the understanding of the dynamic deformation of magnesium. Due to the richness of the deformation mechanisms of magnesium and the complexities induced by dynamic loading, several avenues for extension of this research are available. A few of the potential research directions for future work are discussed here.

- Microstructural evolution under quasi-static loading: In Chapter 3, the analysis of microstructural evolution of extruded magnesium under high strain rate loading was performed and the dominant deformation mechanisms were identified. Similar analysis performed on samples deformed at quasi-static rates of loading will enable us to understand the rate sensitivity of the deformation modes. The

analyses performed till date have focused on the qualitative comparison of twinning at different strain rates and ignored the dislocation activity [55, 60]. TEM analysis of the dislocation structures and dislocation density will be especially important as dislocation slip is generally sensitive to the rate of loading.

- Behavior at low temperature and high strain rates: In the work presented in this thesis, contraction twinning is generally not observed. The general understanding of contraction twinning is still lacking. Experiments that impose compression along the $\langle c \rangle$ axis can be performed at low temperatures and high strain rates. Under such conditions, dislocation mobility is expected to be low and contraction twinning may be favorable. This will enable us to improve our understanding of the contraction twinning mechanism.

- Improvements to the constitutive model: The current constitutive model presented in Chapter 4 uses an empirical formulation for the evolution of twin volume fraction. A physics based formulation for the growth of twins is necessary to add predictive capabilities to the model. The evolution of twin volume fraction based on the motion of twin boundary due to twinning dislocations (such as that in Ref [132]) can be implemented in the model.

  The current constitutive model does not account for the strain rate dependence of mechanisms explicitly. Dislocation slip is typically sensitive to the strain rate and although a complete understanding of the effect of strain rate on deforma-

tion twinning is lacking, studies suggest that extension twinning is somewhat sensitive to the loading rates [55, 60]. Incorporation of strain rate dependence in the model will enable us to capture the material behavior more accurately.

- Normal impact at different velocities: Normal impact experiments conducted at different impact velocities (generating different stress amplitudes) will enable us to understand the dependence of twinning on stress (and strain rate).

- Pressure shear plate impact: Pressure shear plate impact experiments will be valuable in analyzing the behavior of magnesium materials under constant high strain rate loading under combined pressure and shear loading. This will provide nominally homogeneous loading withing the thin magnesium specimen and simplify the analysis.

- Twin shapes: An analysis of the shapes of different twin variants in 2D and 3D will be extremely valuable. A detailed study of the structure of twin boundaries is also necessary for successfully modeling twin boundary motion.

- TEM analysis of dislocation activity under impact loading: The analysis in Chapter 5 indicates that the time duration of deformation has a significant effect on the extension twinning mechanism. The relative contribution of deformation twinning and dislocation slip to the plastic deformation under the microsecond loading is unknown. TEM analysis of the dislocations in the impacted samples will enable us to understand this. This may also enable us to

understand the reasons behind the observed differences in the target plates of different thicknesses.

It will be valuable to verify if pyramidal $\langle c+a \rangle$ slip (observed inside twins in extruded magnesium deformed in Kolsky bar) is observed inside the extension twins formed in single crystal Mg under $\langle a \rangle$ axis impact.

- Impact experiments on single crystals along the $\langle c \rangle$ axis: Impact experiments on single crystal Mg along the $\langle c \rangle$ axis will enable us to identify the dominant deformation mode under this microsecond loading. A comparison of these experiments with the ongoing shock experiments on Mg single crystals (Winey and Gupta) will be valuable in understanding the effect of the impact/shock stress amplitude on the deformation mechanisms.

- UMAT in Abaqus simulations: The elastic-plastic simulations in Abaqus/Explicit presented in Chapter 5 do not capture the experimental observations of the free surface velocity closely. The simulations were performed using a material model based on extrapolated experimental data. This model did not incorporate the dependence of strain hardening to the strain rate. In order to represent the material behavior more accurately, a user defined material (UMAT) can be developed and implemented in Abaqus. The mechanism based scalar constitutive model presented in Chapter 4 is able to capture the behavior of magnesium. Thsi constitutive model can be implemented in a subroutine for incorporation

into the Abaqus simulations. This will also enable us to predict the spatial and temporal evolution of the stress and strain histories in the experiment more accurately.

Appendix

Abaqus simulations

The development of the plate impact simulations in Abqus/Explicit is discussed here. First, purely elastic simulations were performed which were followed by the simulations using an elastic-plastic bilinear model. Finally, a model based on the experimentally measured stress-strain data was used to run simulations with and without strain rate dependence. The strain rate dependent model based on experimental data was finally used to perform the simulations presented in Chapter 5. The results of the prior models are presented here.

A magnesium flyer plate impacting a magnesium target plate is simulated using a 2D plane strain configuration. The diameter of the flyer and target plates was taken to be 25.4 mm and three different thickness values of 2 mm, 3.5 mm and 7 mm were used to simulate the different experiments. The flyer plate is given an initial velocity of 60 m/s and the target plate is initially stationary. The top and bottom edges of the flyer and target plates are constrained to have zero displacement in the

lateral direction in order to simulate the uniaxial strain condition. The schematic of the setup is shown in Fig A1 below. The 2D plane strain element CPE4R was used which is a 4-node bilinear quadrilateral element. The 2 mm, 3.5 mm and the 7 mm flyers and targets were discretized into 2000, 3500, and 7000 elements respectively. Therefore, there were 200, 350 and 700 elements across the thickness and 10 elements across the diameter with the thickness of each element being 10μm. This distribution of elements was chosen since it is important to resolve the stress, strain evolution in the through thickness direction as compared to the lateral direction.

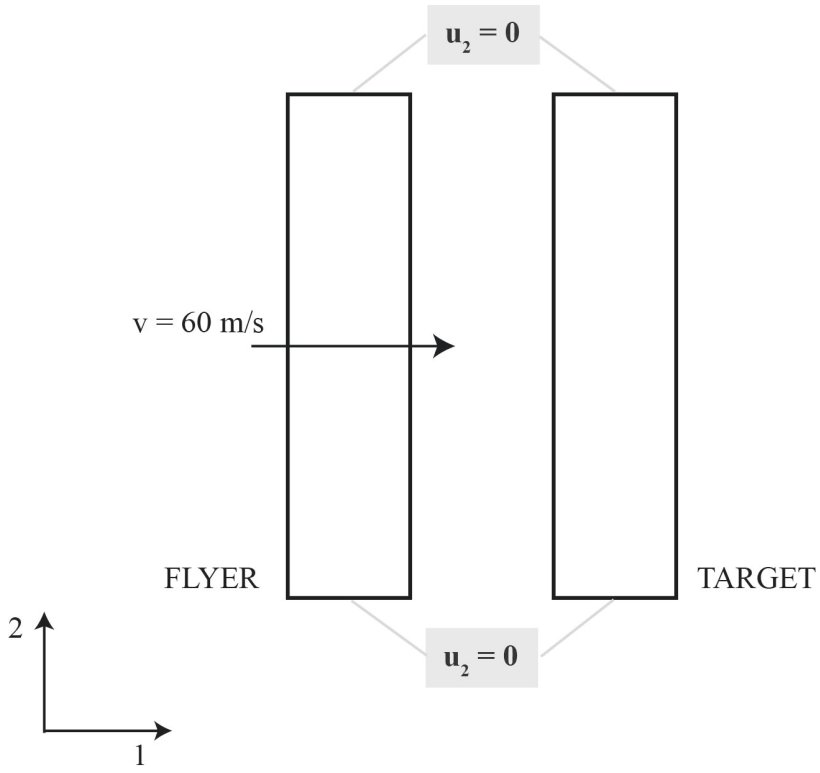

Figure A1: Simulation setup in Abaqus

First, purely elastic simulations were performed using material properties that are listed in the table below for both the target and flyer plates [12].

Density, ρ	1740 kg/m^3
Elastic modulus, E	44 GPa
Poisson's ratio, ν	0.35

Table A1: Elastic properties of pure Magnesium

Linear elastic response

The case in which the material remains purely elastic under the impact velocity of 60 m/s is shown in the figures below. Fig A2 shows the rear surface velocity of a 3.5 mm target. The free surface velocity rises rapidly to the value of the impact velocity of 60 m/s upon the arrival of the longitudinal elastic wave at the rear surface of the target and remains constant thereafter. The longitudinal elastic wave speed in the material is about 6370 m/s. The elastic wave arrives at the free surface at $\sim$0.55 μs (Table 5.2). The longitudinal stress history at a region 1 mm away from the impact face of the target is shown in Fig A3. The elastic wave arrives at this location at approximately 0.16 μs. The estimated value of the longitudinal stress due to the purely elastic wave propagation is $\sigma_{11} = \frac{1}{2}\rho cv \approx 332$ MPa. This stress is compressive in nature. The von Mises effective stress is also plotted in Fig A4 as a reference for comparison with the response of the elastic-plastic material models used later. The Mises stress at this location rises upon arrival of the elastic wave to $\sim$150 MPa and stays at a constant value until the unloading wave from the free surface reaches the location.

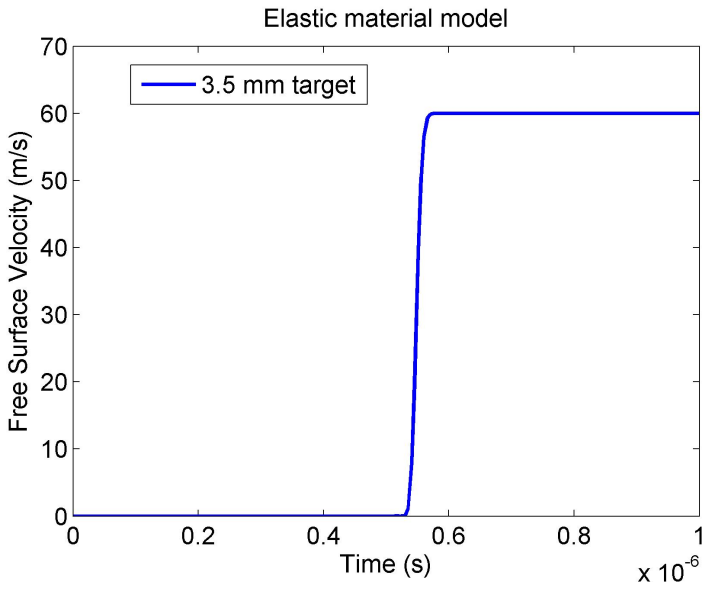

Figure A2: Free surface velocity time history for 3.5 mm target with a purely elastic response

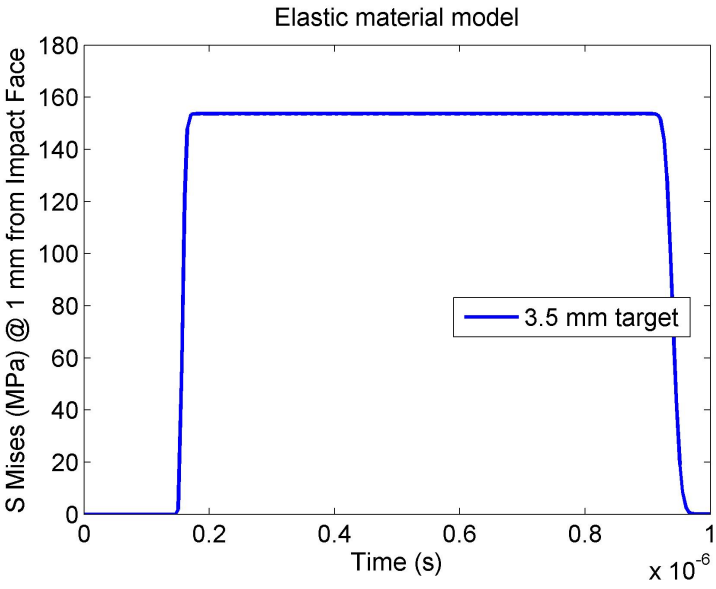

Figure A4: von Mises effective stress time history for purely elastic 3.5 mm target

In the plate impact experiments, the material undergoes inelastic deformation.

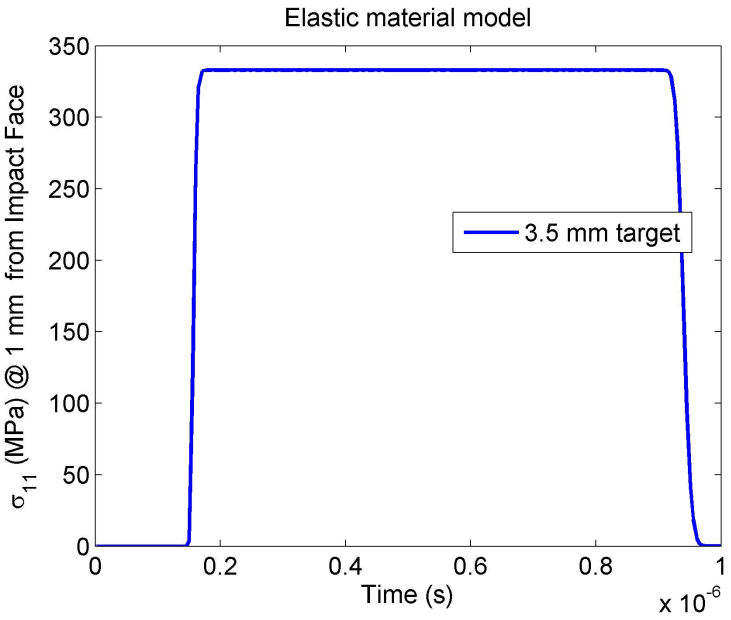

Figure A3: Longitudinal stress time history for 3.5 mm target with a purely elastic response

Therefore, it is useful to consider an elastic-plastic simulation in Abaqus. Von-Mises plasticity or the J2 flow theory is used in the Abaqus/Explicit simulations.

Bilinear elastic-plastic response

As a first step towards incorporating plastic material model in Abaqus/Explicit, we performed simulations with a bilinear elastic-plastic material model. The material behavior is assumed to be strain rate independent. Isotropic elastic-plastic material properties for magnesium were used for both the flyer and target plates. The material behavior in the plastic regime was represented by a simple bi-linear elastic-plastic behavior in order to simplify the analysis. The elastic properties of the material were

the same as before. The plastic behavior was described by the linear interpolation between the stress and plastic strain values in Table A2. These values are taken from the behavior measured under the high strain rate Kolsky bar loading.

Stress (MPa)	Plastic strain
$\sigma_y = 60$	0.0
$\sigma_{0.15} = 320$	0.15

Table A2: Material properties for the bilinear elastic-plastic model

The impact velocity of 60 m/s generates a stress amplitude above the yield limit of the material. Therefore, the wavefront decomposes into an elastic and a plastic wave with the plastic part traveling slower than the elastic part. Fig A5 shows the free surface velocity history for the elastic-plastic targets of different thicknesses. If the material response remained purely elastic, the free surface velocity would rise rapidly to 60 m/s upon arrival of the elastic wave. In this case, due to the plastic yielding, the velocity profile rises to the value corresponding to the yield limit upon arrival of the elastic wave. The plastic wave arrival later increases the velocity to its peak value.

The Abaqus simulations were used to study the evolution of stresses and strains in the target through the thickness and time. It is helpful to understand the effect of the

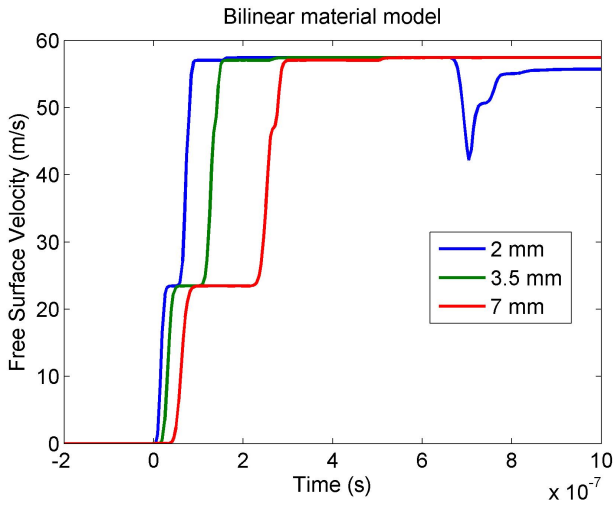

Figure A5: Free surface velocity history for different target thicknesses for the bilinear elastic-plastic material model

elastic and plastic waves on the stresses and strains at different locations in the plate. The von-Mises plasticity used in Abaqus considers yielding to occur when the mises equivalent stress (S Mises) exceeds the yield value specified. Considering a simple two wave analysis - an elastic wave and a plastic wave, we can use the estimated wave speeds to understand the effect on the stresses and strain in the material due to the wave propagation. As an example, the plane at the center of the 2 mm thick target (i.e. 1 mm away from the impact face) was chosen.The location was chosen such that the reflected waves from the free surface will reach this location at later times. This helps simplify the analysis due to the separation between loading and reflected waves. Fig A6 the x-t diagram for the elastic-plastic wave propagation with markers indicating the times at which these waves arrive at the point of interest. The von-Mises equivalent stress (S Mises) history at this point is also shown. The lowercase letters

a and b represent the arrival of the elastic wave and the uppercase letters A and B represent the plastic wave. The markers represent the times calculated assuming the wave speeds in Eq **??** and Eq **??**. From the figure, it an be observed that upon arrival of the elastic wave (a), the stress increases to the value of the yield limit (60 MPa) and then there is further increase due to the plastic wave (A). The stress remains at this constant value until the reflected elastic wave (b) unloads it. The reflected plastic wave (B) arrives increasing the stress again to a slightly higher value due to the isotropic linear hardening in the material model. At points such as P, the loading plastic wave and the reflected elastic wave arrive at the same time. Their interaction adds complexity to the analysis. The effect of this interaction is seen at the point P on the stress history plot. The analysis therafter becomes complicated. The important point to note is that the stresses do not exceed the yield limit after $\sim 1\mu$s and the equivalent plastic strain remains at a constant value for the 2 mm target thereafter.

The equivalent stress history at the point 1 mm away from the impact face is plotted for plates of different thicknesses in Fig A8. The differences in the stress history due to the different thicknesses can be observed. The equivalent plastic strain history for the same location is plotted in Fig A9. The plastic strain increases due to the initial yielding of the material at the same time for the three different thicknesses.

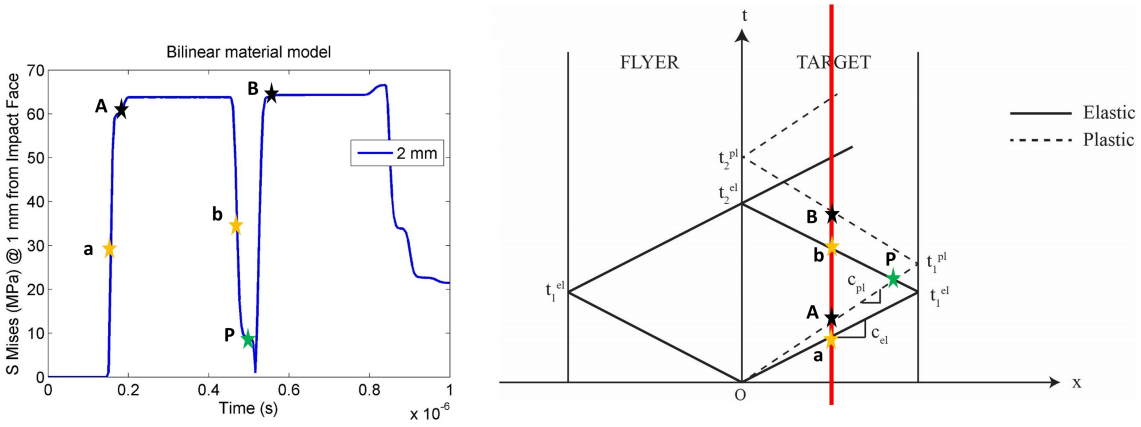

Figure A6: von-Mises equivalent stress history at a point 1 mm away from the impact face of a 2 mm target

The reflected plastic wave from the free surface causes yielding of the material again and increases the plastic strain. This reflected wave arrives at this location at different times due to the difference in the target thickness. It arrives sooner for the 2 mm thick target and therefore the plastic strain rises to its peak value in shorter time as compared to the thicker targets. The overall time available for the material point to reach the peak strain value is the shortest for the 2 mm target and longest for the 7 mm target. The accumulated equivalent plastic strain is similar for the different targets. A slightly higher strain is observed for the 7 mm target due to the slightly higher profile of the Mises stress (red line) from the reflected wave.

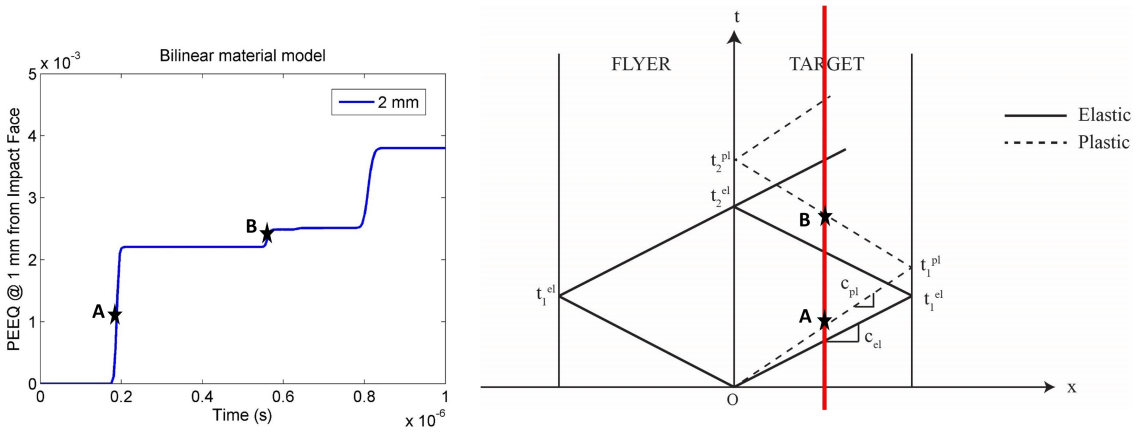

Figure A7: Equivalent plastic strain history at a point 1 mm away from the impact face of a 2 mm target

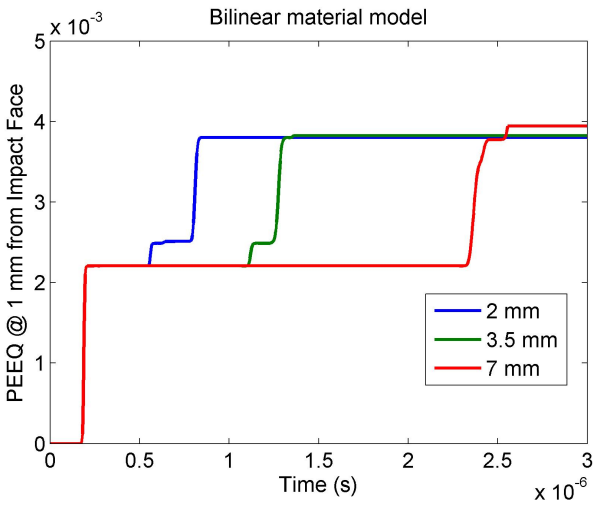

Figure A9: Equivalent plastic strain history for elastic-plastic material response of a 2 mm target

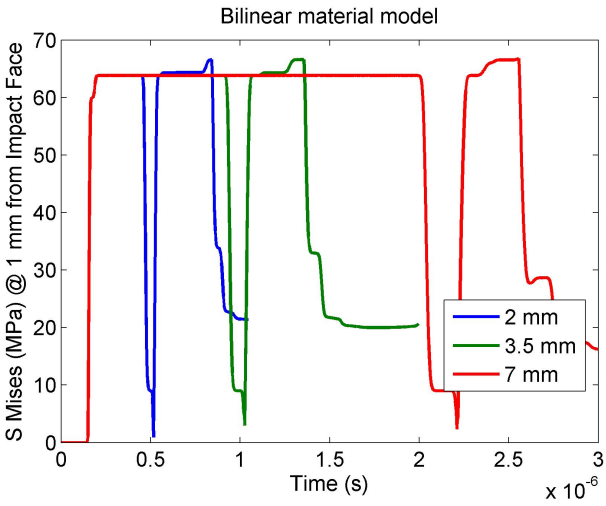

Figure A8: von Mises effective stress time history for elastic-plastic material response of a 2 mm target

Rate independent model based on experimentally measured material behavior

The bilinear material model used in the previous case is a simplifying assumption and not a realistic representation. Instead of assuming the bilinear material response, the experimentally measured dynamic stress-strain response from Chapter 3 is used to describe the material behavior. In this section, the results obtained from a strain rate independent material model based on the experimental data are presented. The elastic properties of the material were kept the same. The plastic behavior is described by the dynamic experimental data and a strain rate independent behavior is assumed. Simulations were performed for plates of the three different thicknesses. The free surface velocity profiles from the simulations are shown in Fig A10. The profiles

show the effect of the elastic and plastic waves on the velocity history. A sharp step in the velocity history from the elastic and plastic wave is observed. If we compare these free surface velocity profiles to the experimentally measured free surface profiles (Fig 5.6), we observe that the simulations do not capture the nature of the velocity history accurately. Therefore, we can conclude that the experimentally based strain rate independent material model used in the simulation does not capture the material response accurately.

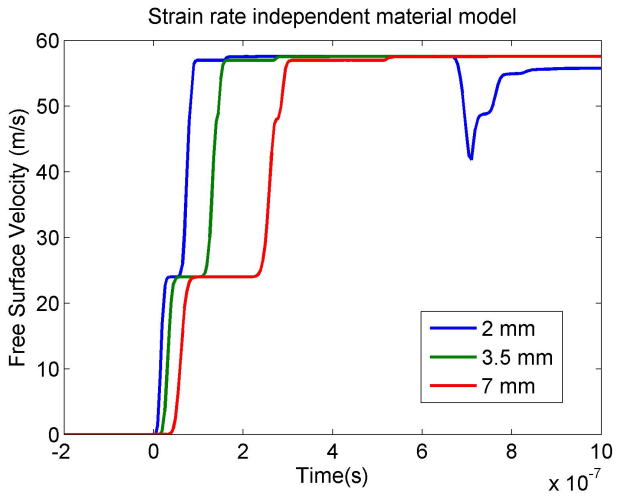

Figure A10: Free surface velocity time history for different target thicknesses with the rate independent model based on experimental data

We compare the effective von Mises stress and the equivalent plastic strain history at the same location (1 mm from impact face) in targets of different thickness with the rate independent material model with dynamic experimental data. The von-Mises equivalent stress history is similar to the one in case of the bilinear material model.

In this case, the peak stress value remains close to the yield value. This is because the experimentally measured stress-strain response of the material is such that the material behavior is almost perfectly plastic just after yield. As the strains induced from this loading are very small, they lie in this almost purely plastic regime. Hence, the corresponding peak mises equivalent stresses in the plate impact simulation are just above the yield limit. The equivalent plastic strain profiles are also similar. A slightly higher value of the peak plastic strain is observed for the 7 mm target here as well similar to the bilinear material model case.

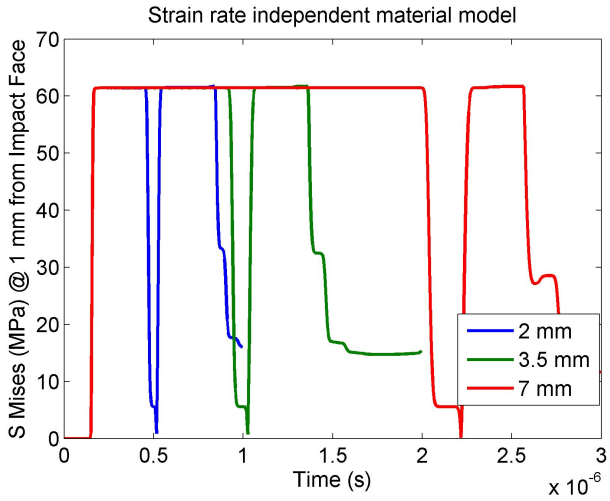

Figure A11: von Mises stress history at a location 1 mm away from the impact surface in targets of different thicknesses with the rate independent model based on experimental data

The accumulated plastic strain in the target during the deformation is shown for

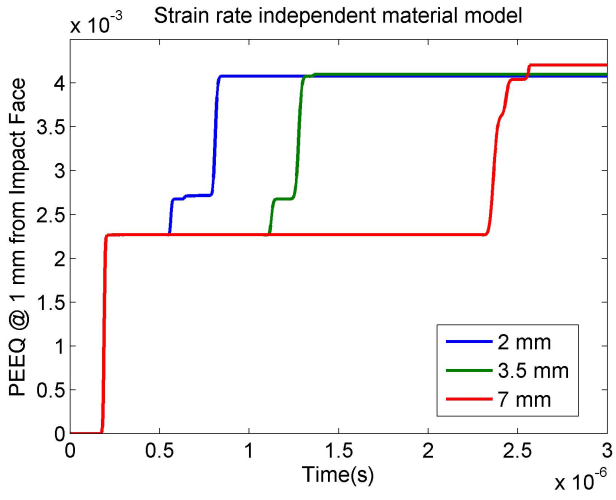

Figure A12: Equivalent plastic strain history at a location 1 mm away from the impact surface in targets of different thicknesses with the rate independent model based on experimental data

all cases in Fig A13. This distribution is shown on a normalized distance from the impact face in Fig A13b for easier comparison. It can be observed that a more or less uniform distribution of plastic strain through the target thickness is observed from this rate independent material model. The plastic strain accumulated at the impact face and the rear face is different due to the effect of the boundary conditions. In the next section, we implement rate dependence into the material model in order to obtain material behavior closer to that observed in the experiments.

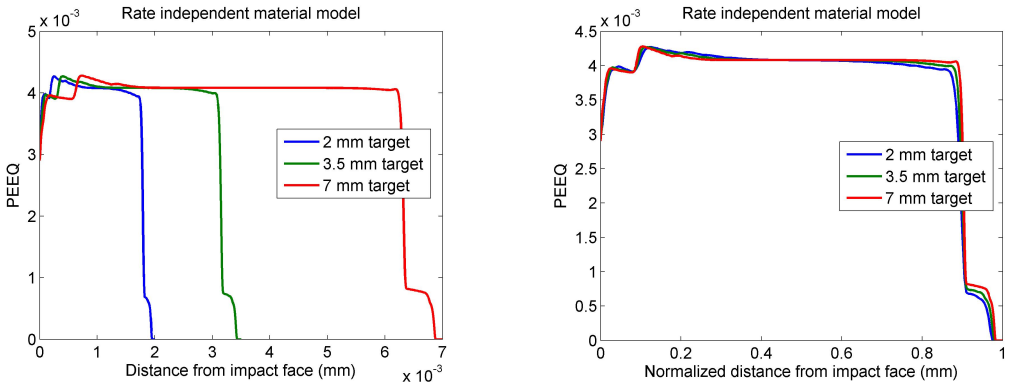

(a) (b)

Figure A13: Accumulated equivalent plastic strain distribution through targets of various thicknesses calculated with a rate independent model plotted along (a) real distance from the impact face (b) normalized distance from the impact face

Bibliography

[1] S.-G. Hong, S. H. Park, and C. S. Lee, "Role of 1012 twinning characteristics in the deformation behavior of a polycrystalline magnesium alloy," *Acta Materialia*, vol. 58, no. 18, pp. 5873 – 5885, 2010. [Online]. Available: http://www.sciencedirect.com/science/article/pii/S135964541000426X

[2] J. Zhang and S. P. Joshi, "Phenomenological crystal plasticity modeling and detailed micromechanical investigations of pure magnesium," *Journal of the Mechanics and Physics of Solids*, vol. 60, no. 5, pp. 945–972, 2012.

[3] K. T. Ramesh, "High rates and impact experiments," *Springer handbook of experimental solid mechanics*, pp. 929–960, 2008.

[4] S. Yadav, *An experimental and numerical investigation of dynamic deformations in metal-matrix and tungsten-based composites*, 1997.

[5] B. Mordike and T. Ebert, "Magnesium: Propertiesapplicationspotential," *Materials Science and Engineering: A*, vol. 302, no. 1, pp. 37–45, 2001.

BIBLIOGRAPHY

[6] G. Cole, "Magnesium vision 2020-a north american automotive strategic vision for magnesium," in *IMA-PROCEEDINGS-*. INTERNATIONAL MAGNESIUM ASSOCIATION, 2007, p. 13.

[7] M. Easton, A. Beer, M. Barnett, C. Davies, G. Dunlop, Y. Durandet, S. Blacket, T. Hilditch, and P. Beggs, "Magnesium alloy applications in automotive structures," *JOM*, vol. 60, no. 11, pp. 57–62, 2008.

[8] T. M. Pollock, "Weight loss with magnesium alloys," *Science*, vol. 328, no. 5981, pp. 986–987, 2010.

[9] F. Witte, "The history of biodegradable magnesium implants: a review," *Acta Biomaterialia*, vol. 6, no. 5, pp. 1680–1692, 2010.

[10] K. Cho, T. Sano, K. Doherty, C. Yen, G. Gazonas, J. Montgomery, P. Moy, B. Davis, and R. DeLorme, "Magnesium technology and manufacturing for ultra lightweight armored ground vehicles," DTIC Document, Tech. Rep., 2009.

[11] M. Pekguleryuz, "1 - current developments in wrought magnesium alloys," in *Advances in Wrought Magnesium Alloys*, ser. Woodhead Publishing Series in Metals and Surface Engineering, C. Bettles and M. Barnett, Eds. Woodhead Publishing, 2012, pp. 3 – 62. [Online]. Available: http://www.sciencedirect.com/science/article/pii/B9781845699680500016

BIBLIOGRAPHY

[12] M. M. Avedesian, H. Baker *et al.*, "Asm specialty handbook: magnesium and magnesium alloys," *ASM International, Materials Park, OH*, p. 15, 1999.

[13] E. Kelley and W. HOSFORD, "The deformation characteristics of textured magnesium," *TRANS MET SOC AIME*, vol. 242, no. 4, 1968.

[14] A. Couret and D. Caillard, "An in situ study of prismatic glide in magnesiumi. the rate controlling mechanism," *Acta Metallurgica*, vol. 33, no. 8, pp. 1447 – 1454, 1985. [Online]. Available: http://www.sciencedirect.com/science/article/pii/0001616085900458

[15] M. Yoo, "Slip, twinning, and fracture in hexagonal close-packed metals," *Metallurgical and Materials Transactions A*, vol. 12, pp. 409–418, 1981, 10.1007/BF02648537. [Online]. Available: http://dx.doi.org/10.1007/BF02648537

[16] S. Agnew, M. Yoo, and C. Tome, "Application of texture simulation to understanding mechanical behavior of mg and solid solution alloys containing li or y," *Acta Materialia*, vol. 49, no. 20, pp. 4277–4289, 2001.

[17] S. Agnew, J. Horton, and M. Yoo, "Transmission electron microscopy investigation of c+a dislocations in mg and solid solution mg-li alloys," *Metallurgical and Materials Transactions A*, vol. 33, no. 3, pp. 851–858, 2002. [Online]. Available: http://dx.doi.org/10.1007/s11661-002-0154-x

[18] S. R. Agnew and Ö. Duygulu, "Plastic anisotropy and the role of non-basal slip in magnesium alloy az31b," *International journal of plasticity*, vol. 21, no. 6, pp. 1161–1193, 2005.

[19] T. Al-Samman, X. Li, and S. G. Chowdhury, "Orientation dependent slip and twinning during compression and tension of strongly textured magnesium az31 alloy," *Materials Science and Engineering: A*, vol. 527, no. 15, pp. 3450 – 3463, 2010. [Online]. Available: http://www.sciencedirect.com/science/article/pii/S0921509310001577

[20] M. Barnett, Z. Keshavarz, A. Beer, and D. Atwell, "Influence of grain size on the compressive deformation of wrought mg-3al-1zn," *Acta Materialia*, vol. 52, no. 17, pp. 5093 – 5103, 2004. [Online]. Available: http://www.sciencedirect.com/science/article/pii/S1359645404004240

[21] M. Barnett, "Twinning and the ductility of magnesium alloys: Part i: twins," *Materials Science and Engineering: A*, vol. 464, no. 1-2, pp. 1 – 7, 2007. [Online]. Available: http://www.sciencedirect.com/science/article/pii/S0921509306026876

[22] ——, "Twinning and the ductility of magnesium alloys: Part ii. twins," *Materials Science and Engineering: A*, vol. 464, no. 1-2, pp. 8 – 16, 2007. [Online]. Available: http://www.sciencedirect.com/science/article/pii/S0921509307004297

[23] Y. Chino, K. Kimura, and M. Mabuchi, "Twinning behavior and deformation mechanisms of extruded az31 mg alloy," *Materials Science and Engineering: A*, vol. 486, no. 1-2, pp. 481 – 488, 2008. [Online]. Available: http://www.sciencedirect.com/science/article/pii/S0921509307016991

[24] J. Del Valle, F. Carreño, and O. A. Ruano, "Influence of texture and grain size on work hardening and ductility in magnesium-based alloys processed by ecap and rolling," *Acta Materialia*, vol. 54, no. 16, pp. 4247–4259, 2006.

[25] M. D. Nave and M. R. Barnett, "Microstructures and textures of pure magnesium deformed in plane-strain compression," *Scripta materialia*, vol. 51, no. 9, pp. 881–885, 2004.

[26] J. Koike, "Enhanced deformation mechanisms by anisotropic plasticity in polycrystalline mg alloys at room temperature," *Metallurgical and Materials Transactions A*, vol. 36, pp. 1689–1696, 2005, 10.1007/s11661-005-0032-4. [Online]. Available: http://dx.doi.org/10.1007/s11661-005-0032-4

[27] J. Koike, N. Fujiyama, D. Ando, and Y. Sutou, "Roles of deformation twinning and dislocation slip in the fatigue failure mechanism of az31 mg alloys," *Scripta Materialia*, vol. 63, no. 7, pp. 747 – 750, 2010, viewpoint set no. 47 Magnesium Alloy Science and Technology. [Online]. Available: http://www.sciencedirect.com/science/article/pii/S1359646210001594

[28] R. Gehrmann, M. Frommert, and G. Gottstein, "Texture effects on plastic

deformation of magnesium," *Materials Science and Engineering: A*, vol. 395, no. 1, pp. 338–349, 2005.

[29] L. Jiang, J. Jonas, R. Mishra, A. Luo, A. Sachdev, and S. Godet, "Twinning and texture development in two mg alloys subjected to loading along three different strain paths," *Acta Materialia*, vol. 55, no. 11, pp. 3899 – 3910, 2007. [Online]. Available: http://www.sciencedirect.com/science/article/pii/S1359645407001899

[30] L. Jiang, J. J. Jonas, A. A. Luo, A. K. Sachdev, and S. Godet, "Influence of 10-12 extension twinning on the flow behavior of az31 mg alloy," *Materials Science and Engineering: A*, vol. 445-446, pp. 302 – 309, 2007. [Online]. Available: http://www.sciencedirect.com/science/article/pii/S0921509306020363

[31] A. Akhtar and E. Teghtsoonian, "Solid solution strengthening of magnesium single crystalsii the effect of solute on the ease of prismatic slip," *Acta Metallurgica*, vol. 17, no. 11, pp. 1351–1356, 1969.

[32] S. Taylor, *Plastic strain in metals*, 1938.

[33] G. Groves and A. Kelly, "Independent slip systems in crystals," *Philosophical Magazine*, vol. 8, no. 89, pp. 877–887, 1963.

[34] H. Yoshinaga and R. Horiuchi, "Deformation mechanisms in magnesium single

crystals compressed in the direction parallel to hexagonal axis," *Trans. JIM*, vol. 4, p. 1, 1963.

[35] T. Kitahara, S. Ando, M. Tsushida, H. Kitahara, and H. Tonda, "Deformation behavior of magnesium single crystals in c-axis compression," *Key Engineering Materials*, vol. 345, pp. 129–132, 2007.

[36] J. Stohr and J. Poirier, "Electron-microscope study of pyramidal slip 1122 1123 in mg," *Phil. Mag.*, vol. 25, no. 6, pp. 1313–1329, 1972.

[37] E. Kelley and W. HOSFORD, "Plane-strain compression of magnesium and magnesium alloy crystals," *Trans Met Soc AIME*, vol. 242, no. 1, pp. 5–13, 1968.

[38] T. Obara, H. Yoshinga, and S. Morozumi, "1122¡1123¿ slip system in magnesium," *Acta Metallurgica*, vol. 21, no. 7, pp. 845 – 853, 1973. [Online]. Available: http://www.sciencedirect.com/science/article/pii/0001616073901417

[39] A. Chapuis and J. H. Driver, "Temperature dependency of slip and twinning in plane strain compressed magnesium single crystals," *Acta Materialia*, vol. 59, no. 5, pp. 1986–1994, 2011.

[40] B. C. Wonsiewicz, "Plasticity of magnesium crystals." Ph.D. dissertation, Massachusetts Institute of Technology, 1966.

[41] I. Beyerlein, "Statistical analyses of deformation twinning in magnesium," *Philosophical Magazine*, vol. Vol. 90, No. 16, p. 21612190, 2010.

[42] I. Beyerlein, R. McCabe, and C. Tom, "Effect of microstructure on the nucleation of deformation twins in polycrystalline high-purity magnesium: A multi-scale modeling study," *Journal of the Mechanics and Physics of Solids*, vol. 59, no. 5, pp. 988 – 1003, 2011. [Online]. Available: http://www.sciencedirect.com/science/article/pii/S0022509611000354

[43] Q. Yu, L. Qi, K. Chen, R. K. Mishra, J. Li, and A. M. Minor, "The nanostructured origin of deformation twinning," *Nano letters*, vol. 12, no. 2, pp. 887–892, 2012.

[44] H. Yoshinaga and R. Horiuchï, "On the nonbasal slip in magnesium crystals," *Transactions of the Japan Institute of Metals*, vol. 5, no. 1, pp. 14–21, 1963.

[45] S. Agnew, C. Tomé, D. Brown, T. Holden, and S. Vogel, "Study of slip mechanisms in a magnesium alloy by neutron diffraction and modeling," *Scripta Materialia*, vol. 48, no. 8, pp. 1003–1008, 2003.

[46] M. Yoo, S. Agnew, J. Morris, and K. Ho, "Non-basal slip systems in hcp metals and alloys: source mechanisms," *Materials Science and Engineering: A*, vol. 319321, no. 0, pp. 87 – 92, 2001. [Online]. Available: http://www.sciencedirect.com/science/article/pii/S0921509301010279

[47] O. Murnsky, D. Carr, M. Barnett, E. Oliver, and P. ittner, "Investigation of deformation mechanisms involved in the plasticity of az31 mg alloy: In situ neutron diffraction and epsc modelling," *Materials Science and Engineering: A*, vol. 496, no. 12, pp. 14 – 24, 2008. [Online]. Available: http://www.sciencedirect.com/science/article/pii/S092150930800823X

[48] D. Brown, S. Agnew, M. Bourke, T. Holden, S. Vogel, and C. Tom, "Internal strain and texture evolution during deformation twinning in magnesium," *Materials Science and Engineering: A*, vol. 399, no. 1-2, pp. 1 – 12, 2005, measurement and Interpretation of Internal/Residual Stresses. [Online]. Available: http://www.sciencedirect.com/science/article/pii/S0921509305001541

[49] S. Godet, L. Jiang, A. Luo, and J. Jonas, "Use of schmid factors to select extension twin variants in extruded magnesium alloy tubes," *Scripta Materialia*, vol. 55, no. 11, pp. 1055 – 1058, 2006. [Online]. Available: http://www.sciencedirect.com/science/article/pii/S1359646206005550

[50] M. Knezevic, A. Levinson, R. Harris, R. K. Mishra, R. D. Doherty, and S. R. Kalidindi, "Deformation twinning in az31: Influence on strain hardening and texture evolution," *Acta Materialia*, vol. 58, no. 19, pp. 6230 – 6242, 2010. [Online]. Available: http://www.sciencedirect.com/science/article/pii/S1359645410004854

[51] H. El Kadiri, J. Kapil, A. Oppedal, L. Hector, S. R. Agnew, M. Cherkaoui, and

S. Vogel, "The effect of twin–twin interactions on the nucleation and propagation of twinning in magnesium," *Acta Materialia*, vol. 61, no. 10, pp. 3549–3563, 2013.

[52] Z. Keshavarz and M. R. Barnett, "Ebsd analysis of deformation modes in mg–3al–1zn," *Scripta materialia*, vol. 55, no. 10, pp. 915–918, 2006.

[53] T. Al-Samman and G. Gottstein, "Room temperature formability of a magnesium az31 alloy: Examining the role of texture on the deformation mechanisms," *Materials Science and Engineering: A*, vol. 488, no. 1, pp. 406–414, 2008.

[54] P. Cizek and M. Barnett, "Characteristics of the contraction twins formed close to the fracture surface in mg–3al–1zn alloy deformed in tension," *Scripta Materialia*, vol. 59, no. 9, pp. 959–962, 2008.

[55] M. Tucker, M. Horstemeyer, P. Gullett, H. El Kadiri, and W. Whittington, "Anisotropic effects on the strain rate dependence of a wrought magnesium alloy," *Scripta Materialia*, vol. 60, no. 3, pp. 182–185, 2009.

[56] S. Agnew, J. Horton, T. Lillo, and D. Brown, "Enhanced ductility in strongly textured magnesium produced by equal channel angular processing," *Scripta Materialia*, vol. 50, no. 3, pp. 377–381, 2004.

[57] A. A. Luo, "Magnesium casting technology for structural applications," *Journal of Magnesium and Alloys*, vol. 1, no. 1, pp. 2–22, 2013.

[58] S. Biswas, S. Suwas, R. Sikand, and A. K. Gupta, "Analysis of texture evolution in pure magnesium and the magnesium alloy am30 during rod and tube extrusion," *Materials Science and Engineering: A*, vol. 528, no. 10, pp. 3722–3729, 2011.

[59] I. Ulacia, N. Dudamell, F. Glvez, S. Yi, M. Prez-Prado, and I. Hurtado, "Mechanical behavior and microstructural evolution of a mg az31 sheet at dynamic strain rates," *Acta Materialia*, vol. 58, no. 8, pp. 2988 – 2998, 2010. [Online]. Available: http://www.sciencedirect.com/science/article/pii/S1359645410000431

[60] N. Dudamell, I. Ulacia, F. Gálvez, S. Yi, J. Bohlen, D. Letzig, I. Hurtado, and M. Perez-Prado, "Twinning and grain subdivision during dynamic deformation of a mg az31 sheet alloy at room temperature," *Acta Materialia*, vol. 59, no. 18, pp. 6949–6962, 2011.

[61] T. Mukai, M. Yamanoi, H. Watanabe, and K. Higashi, "Ductility enhancement in az31 magnesium alloy by controlling its grain structure," *Scripta Materialia*, vol. 45, no. 1, pp. 89–94, 2001.

[62] B. Wu, Y. Zhao, X. Du, Y. Zhang, F. Wagner, and C. Esling, "Ductility enhancement of extruded magnesium via yttrium addition," *Materials Science and Engineering: A*, vol. 527, no. 16, pp. 4334–4340, 2010.

[63] R. K. Mishra, A. K. Gupta, P. R. Rao, A. K. Sachdev, A. M. Kumar, and

A. A. Luo, "Influence of cerium on the texture and ductility of magnesium extrusions," *Scripta Materialia*, vol. 59, no. 5, pp. 562–565, 2008.

[64] A. Jain, O. Duygulu, D. Brown, C. Tomé, and S. Agnew, "Grain size effects on the tensile properties and deformation mechanisms of a magnesium alloy, az31b, sheet," *Materials Science and Engineering: A*, vol. 486, no. 1, pp. 545–555, 2008.

[65] M. A. Meyers, *Dynamic behavior of materials*. John Wiley & Sons, 1994.

[66] M. Meyers, O. Vöhringer, and V. Lubarda, "The onset of twinning in metals: a constitutive description," *Acta materialia*, vol. 49, no. 19, pp. 4025–4039, 2001.

[67] K. Ishikawa, H. Watanabe, and T. Mukai, "High strain rate deformation behavior of an az91 magnesium alloy at elevated temperatures," *Materials Letters*, vol. 59, no. 12, pp. 1511 – 1515, 2005. [Online]. Available: http://www.sciencedirect.com/science/article/pii/S0167577X05000376

[68] T. Mukai, T. Mohri, M. Mabuchi, M. Nakamura, K. Ishikawa, and K. Higashi, "Experimental study of a structural magnesium alloy with high absorption energy under dynamic loading," *Scripta Materialia*, vol. 39, no. 9, pp. 1249 – 1253, 1998. [Online]. Available: http://www.sciencedirect.com/science/article/pii/S1359646298002966

[69] B. Li, S. Joshi, K. Azevedo, E. Ma, K. Ramesh, R. Figueiredo, and

T. Langdon, "Dynamic testing at high strain rates of an ultrafine-grained magnesium alloy processed by ecap," *Materials Science and Engineering: A*, vol. 517, no. 12, pp. 24 – 29, 2009. [Online]. Available: http://www.sciencedirect.com/science/article/pii/S092150930900358X

[70] B. Li, S. P. Joshi, O. Almagri, Q. Ma, K. Ramesh, and T. Mukai, "Rate-dependent hardening due to twinning in an ultrafine-grained magnesium alloy," *Acta Materialia*, vol. 60, no. 4, pp. 1818–1826, 2012.

[71] S. Agnew, W. Whittington, A. Oppedal, H. El Kadiri, M. Shaeffer, K. Ramesh, J. Bhattacharyya, R. Delorme, and B. Davis, "Dynamic behavior of a rare-earth-containing mg alloy, we43b-t5, plate with comparison to conventional alloy, am30-f," *JOM*, vol. 66, no. 2, pp. 277–290, 2014.

[72] K. E. Prasad, B. Li, N. Dixit, M. Shaffer, S. Mathaudhu, and K. Ramesh, "The dynamic flow and failure behavior of magnesium and magnesium alloys," *JOM*, vol. 66, no. 2, pp. 291–304, 2014.

[73] L. Jiang, J. J. Jonas, A. A. Luo, A. K. Sachdev, and S. Godet, "Twinning-induced softening in polycrystalline am30 mg alloy at moderate temperatures," *Scripta Materialia*, vol. 54, no. 5, pp. 771 – 775, 2006, viewpoint set no. 39: Statistical mechanics and coarse graining of dislocation behavior for continuum plasticity. [Online]. Available: http://www.sciencedirect.com/science/article/pii/S1359646205007566

[74] D. Chichili, K. Ramesh, and K. Hemker, "The high-strain-rate response of alpha-titanium: experiments, deformation mechanisms and modeling," *Acta materialia*, vol. 46, no. 3, pp. 1025–1043, 1998.

[75] J. Millett, S. Stirk, N. Bourne, and G. Gray, "On the behaviour of the magnesium alloy, az61 to one-dimensional shock loading," *Acta Materialia*, vol. 58, no. 17, pp. 5675–5682, 2010.

[76] B. Wu, G. Wan, Y. Zhang, and C. Esling, "Twinning characteristics in textured az31 alloy under impact loading along specified direction," *Materials Letters*, vol. 64, no. 5, pp. 636–639, 2010.

[77] P. Hazell, G. Appleby-Thomas, E. Wielewski, C. Stennett, and C. Siviour, "The influence of microstructure on the shock and spall behaviour of the magnesium alloy, elektron 675," *Acta Materialia*, vol. 60, no. 17, pp. 6042–6050, 2012.

[78] E. Huskins, B. Cao, and K. Ramesh, "Strengthening mechanisms in an almg alloy," *Materials Science and Engineering: A*, vol. 527, no. 6, pp. 1292 – 1298, 2010. [Online]. Available: http://www.sciencedirect.com/science/article/pii/S092150930901257X

[79] D. Jia, A. Lennon, and K. Ramesh, "High-strain-rate pressure-shear recovery: a new experimental technique," *International Journal of solids and structures*, vol. 37, no. 12, pp. 1679–1699, 2000.

[80] K. Ramesh and N. Kelkar, "Technique for the continuous measurement of projectile velocities in plate impact experiments," *Review of scientific instruments*, vol. 66, no. 4, pp. 3034–3036, 1995.

[81] P. Kumar and R. Clifton, "Optical alignment of impact faces for plate impact experiments," *Journal of Applied Physics*, vol. 48, no. 3, pp. 1366–1367, 1977.

[82] J. Bailey and P. Hirsch, "The dislocation distribution, flow stress, and stored energy in cold-worked polycrystalline silver," *Philosophical Magazine*, vol. 5, no. 53, pp. 485–497, 1960.

[83] S.-G. Hong, S. H. Park, and C. S. Lee, "Strain path dependence of 10-12 twinning activity in a polycrystalline magnesium alloy," *Scripta Materialia*, vol. 64, no. 2, pp. 145 – 148, 2011. [Online]. Available: http://www.sciencedirect.com/science/article/pii/S1359646210006482

[84] S. Morozumi, M. Kikuchi, and H. Yoshinaga, "Electron microscope observation in and around {1102} twins in magnesium," *Trans. JIM*, vol. 17, pp. 158–164, 1976.

[85] A. S. Khan, A. Pandey, T. Gnupel-Herold, and R. K. Mishra, "Mechanical response and texture evolution of az31 alloy at large strains for different strain rates and temperatures," *International Journal of Plasticity*, vol. 27, no. 5, pp. 688 – 706, 2011. [Online]. Available: http://www.sciencedirect.com/science/article/pii/S0749641910001142

[86] G. R. Johnson and W. H. Cook, "A constitutive model and data for metals subjected to large strains, high strain rates and high temperatures," in *Proceedings of the 7th International Symposium on Ballistics*, vol. 21. The Netherlands, 1983, pp. 541–547.

[87] I. Ulacia, C. Salisbury, I. Hurtado, and M. Worswick, "Tensile characterization and constitutive modeling of az31b magnesium alloy sheet over wide range of strain rates and temperatures," *Journal of materials processing technology*, vol. 211, no. 5, pp. 830–839, 2011.

[88] M. Barnett, Z. Keshavarz, and X. Ma, "A semianalytical sachs model for the flow stress of a magnesium alloy," *Metallurgical and materials transactions A*, vol. 37, no. 7, pp. 2283–2293, 2006.

[89] F. J. Zerilli and R. W. Armstrong, "Dislocation-mechanics-based constitutive relations for material dynamics calculations," *Journal of Applied Physics*, vol. 61, no. 5, pp. 1816–1825, 1987.

[90] P. Follansbee and U. Kocks, "A constitutive description of the deformation of copper based on the use of the mechanical threshold stress as an internal state variable," *Acta Metallurgica*, vol. 36, no. 1, pp. 81–93, 1988.

[91] Y. Estrin, L. Toth, A. Molinari, and Y. Bréchet, "A dislocation-based model for all hardening stages in large strain deformation," *Acta materialia*, vol. 46, no. 15, pp. 5509–5522, 1998.

[92] S. R. Kalidindi, "Incorporation of deformation twinning in crystal plasticity models," *Journal of the Mechanics and Physics of Solids*, vol. 46, no. 2, pp. 267–290, 1998.

[93] A. Staroselsky and L. Anand, "A constitutive model for hcp materials deforming by slip and twinning: application to magnesium alloy az31b," *International Journal of Plasticity*, vol. 19, no. 10, pp. 1843 – 1864, 2003. [Online]. Available: http://www.sciencedirect.com/science/article/pii/S0749641903000391

[94] A. Salem, S. Kalidindi, and S. Semiatin, "Strain hardening due to deformation twinning in α-titanium: constitutive relations and crystal-plasticity modeling," *Acta Materialia*, vol. 53, no. 12, pp. 3495–3502, 2005.

[95] G. Proust, C. N. Tomé, A. Jain, and S. R. Agnew, "Modeling the effect of twinning and detwinning during strain-path changes of magnesium alloy az31," *International Journal of Plasticity*, vol. 25, no. 5, pp. 861–880, 2009.

[96] L. Murr, "Work jardening and the pressure dependence of dislocation density and arrangements in shock loaded nickel and copper," *Scripta Metallurgica*, vol. 12, no. 2, pp. 201–206, 1978.

[97] U. Kocks and H. Mecking, "Physics and phenomenology of strain hardening: the fcc case," *Progress in materials science*, vol. 48, no. 3, pp. 171–273, 2003.

[98] C. M. Byer and K. Ramesh, "Effects of the initial dislocation density on size

effects in single-crystal magnesium," *Acta Materialia*, vol. 61, no. 10, pp. 3808–3818, 2013.

[99] G. S. Kim, S. Yi, Y. Huang, and E. Lilleodden, "Twining and slip activity in magnesium¡ 11-20¿ single crystal," in *MRS Proceedings*, vol. 1224. Cambridge Univ Press, 2009, pp. 1224–FF05.

[100] B. Syed, J. Geng, R. Mishra, and K. Kumar, "[0001] compression response at room temperature of single crystal magnesium," *Scripta Materialia*, 2012.

[101] J. Yasi, T. Nogaret, D. Trinkle, Y. Qi, L. Hector Jr, and W. Curtin, "Basal and prism dislocation cores in magnesium: comparison of first-principles and embedded-atom-potential methods predictions," *Modelling and Simulation in Materials Science and Engineering*, vol. 17, no. 5, p. 055012, 2009.

[102] C. Caceres, P. Lukáč, and A. Blake, "Strain hardening due to {10 1 2} twinning in pure magnesium," *Philosophical Magazine*, vol. 88, no. 7, pp. 991–1003, 2008.

[103] P. Klimanek and A. Ptzsch, "Microstructure evolution under compressive plastic deformation of magnesium at different temperatures and strain rates," *Materials Science and Engineering A*, vol. 324, no. 1-2, pp. 145 – 150, 2002. [Online]. Available: http://www.sciencedirect.com/science/article/pii/S0921509301012977

[104] H. El Kadiri and A. Oppedal, "A crystal plasticity theory for latent hardening

by glide twinning through dislocation transmutation and twin accommodation effects," *Journal of the Mechanics and Physics of Solids*, vol. 58, no. 4, pp. 613–624, 2010.

[105] R. Boettner, A. McEvily Jr, and Y. Liu, "On the formation of fatigue cracks at twin boundaries," *Philosophical magazine*, vol. 10, no. 103, pp. 95–106, 1964.

[106] B. Li and E. Ma, "Atomic shuffling dominated mechanism for deformation twinning in magnesium," *Phys. Rev. Lett.*, vol. 103, no. 3, p. 035503, Jul 2009.

[107] N. Dixit, K. Y. Xie, K. J. Hemker, and K. Ramesh, "Microstructural evolution of pure magnesium under high strain rate loading," *Acta Materialia*, vol. 87, pp. 56–67, 2015.

[108] C. Cáceres and P. Lukáč, "Strain hardening behaviour and the taylor factor of pure magnesium," *Philosophical Magazine*, vol. 88, no. 7, pp. 977–989, 2008.

[109] S. Groh, E. Marin, M. Horstemeyer, and D. Bammann, "Dislocation motion in magnesium: a study by molecular statics and molecular dynamics," *Modelling and Simulation in Materials Science and Engineering*, vol. 17, no. 7, p. 075009, 2009.

[110] M. Huang, P. E. Rivera-Díaz-del Castillo, O. Bouaziz, and S. van der Zwaag, "A constitutive model for high strain rate deformation in fcc metals based on

irreversible thermodynamics," *Mechanics of Materials*, vol. 41, no. 9, pp. 982–988, 2009.

[111] R. Armstrong, W. Arnold, and F. Zerilli, "Dislocation mechanics of shock-induced plasticity," *Metallurgical and Materials Transactions A*, vol. 38, no. 11, pp. 2605–2610, 2007.

[112] Z. Liu, X. You, and Z. Zhuang, "A mesoscale investigation of strain rate effect on dynamic deformation of single-crystal copper," *International Journal of Solids and Structures*, vol. 45, no. 13, pp. 3674–3687, 2008.

[113] E. L. Huskins, "The thermo-mechanical response of ufg aluminum at high strain rates," Ph.D. dissertation, Johns Hopkins University, 2012.

[114] J. Wang, J. Hirth, and C. Tomé, "Twinning nucleation mechanisms in hexagonal-close-packed crystals," *Acta Materialia*, vol. 57, no. 18, pp. 5521–5530, 2009.

[115] N. Daphalapurkar, J. Wilkerson, T. Wright, and K. Ramesh, "Kinetics of a fast moving twin boundary in nickel," *Acta Materialia*, vol. 68, pp. 82–92, 2014.

[116] J. Zukas, "Impact dynamics," *John Wiley & Sons, Inc, 605 Third Ave, New York, N. Y. 10158, U. S. A, 1982. 452*, 1982.

[117] G. Kanel, S. Razorenov, K. Baumung, and J. Singer, "Dynamic yield and tensile

strength of aluminum single crystals at temperatures up to the melting point," *Journal of Applied Physics*, vol. 90, no. 1, pp. 136–143, 2001.

[118] K. Kim and R. Clifton, "Dislocation motion in mgo crystals under plate impact," *Journal of materials science*, vol. 19, no. 5, pp. 1428–1438, 1984.

[119] T. Mukai, M. YAMANOI, H. WATANABE, K. ISHIKAWA, and K. Higashi, "Effect of grain refinement on tensile ductility in zk60 magnesium alloy under dynamic loading," *Materials transactions-JIM*, vol. 42, no. 7, pp. 1177–1181, 2001.

[120] J. Del Valle and O. A. Ruano, "Influence of texture on dynamic recrystallization and deformation mechanisms in rolled or ecaped az31 magnesium alloy," *Materials Science and Engineering: A*, vol. 487, no. 1, pp. 473–480, 2008.

[121] S. Graff, W. Brocks, and D. Steglich, "Yielding of magnesium: From single crystal to polycrystalline aggregates," *International Journal of Plasticity*, vol. 23, no. 12, pp. 1957–1978, 2007.

[122] R. Reed-Hill, "A study of the {1, 0,-1, 1} and {1, 0,-1, 3} twinning modes in magnesium," *Trans. Met. Soc. AIME*, vol. 218, pp. 554–558, 1960.

[123] C. M. Byer, B. Li, B. Cao, and K. Ramesh, "Microcompression of single-crystal magnesium," *Scripta Materialia*, vol. 62, no. 8, pp. 536–539, 2010.

[124] R. E. Reed-Hill and W. D. Robertson, "Deformation of magnesium single crystals by nonbasal slip," *Journal of Metals-Transactions AIME*, vol. 220, pp. 496–502, 1957.

[125] R. Reed-Hill and W. Robertson, "Additional modes of deformation twinning in magnesium," *Acta Metallurgica*, vol. 5, no. 12, pp. 717–727, 1957.

[126] Q. Li, "Dynamic mechanical response of magnesium single crystal under compression loading: Experiments, model, and simulations," *Journal of Applied Physics*, vol. 109, no. 10, p. 103514, 2011.

[127] G. Kanel, G. Garkushin, A. Savinykh, S. Razorenov, T. de Resseguier, W. Proud, and M. Tyutin, "Shock response of magnesium single crystals at normal and elevated temperatures," *Journal of Applied Physics*, vol. 116, no. 14, p. 143504, 2014.

[128] J. Winey, P. Renganathan, and Y. Gupta, "Shock wave compression and release of hexagonal-close-packed metal single crystals: Inelastic deformation of c-axis magnesium," *Journal of Applied Physics*, vol. 117, no. 10, p. 105903, 2015.

[129] L. J. Slutsky and C. Garland, "Elastic constants of magnesium from 4.2 k to 300 k," *Physical Review*, vol. 107, no. 4, p. 972, 1957.

[130] J. Johnson and R. Rohde, "Dynamic deformation twinning in shock-loaded iron," *Journal of Applied Physics*, vol. 42, no. 11, pp. 4171–4182, 1971.

[131] G. Gray, "Deformation twinning in al-4.8 wt% mg," *Acta Metallurgica*, vol. 36, no. 7, pp. 1745–1754, 1988.

[132] L. Capolungo, I. Beyerlein, and C. Tomé, "Slip-assisted twin growth in hexagonal close-packed metals," *Scripta Materialia*, vol. 60, no. 1, pp. 32–35, 2009.

Vita

Neha Dixit was born in Pune, India in 1986 to Deepti and Ravi Dixit. In 2007, she received the degree of Bachelor of Technology with distinction in Mechanical Engineering from the College of Engineering Pune, India. She then attended The Ohio State University where she received the Master of Science in Mechanical Engineering degree in 2009. In the Fall of 2010, she enrolled in the Mechanical Engineering Ph.D. program at the Johns Hopkins University. She received a M.S.E. in Mechanical Engineering degree in 2013. Her research focuses on the dynamic behavior of lightweight metals combining mechanics and material science.

Starting June 2015, Neha will begin work as a Consultant at the enginering consulting firm, Exponent, in Menlo Park, CA.